Charge Transport and Thermal Properties of A Semicrystalline Polymer Semiconductor

Li-Hong ZHAO

In partial fulfillment of the requirements for the

Degree of Doctor of Philosophy

Department of Physics

National University of Singapore

2010

To my mother

Acknowledgements

The work described in this thesis was carried out in the Organic Nano Device Lab (ONDL), National University of Singapore (NUS), and was supported by research scholarship from the Department of Physics in NUS.

I owe my deepest gratitude to the following people, without whom this thesis would not have been possible. First, I am heartily thankful to Dr. Peter Ho and Dr. Chua Lay-Lay, for leading me into this field, their continuous guidance, constant support and above all their patience throughout my PhD. I am really delighted to work with both of you.

I would like to show my gratitude to all the senior members in ONDL: Dr. Siva, Dr. Chia Perq Jon, Dr. Zhou Mi, Dr. Wang Shuai, Dr. Wong Loke Yuen, Dr. Roland Goh, Rui Qi, Jing-Mei, Dr. Tang Jie-Cong, Guo Han and Bibin for their assistant, fruitful discussions and encouragement. Without them, I could not have completed this project. I also thank all the junior members in ONDL for their encouragement and friendship. It is indeed a pleasure to spend my PhD time with all of you.

I would like to acknowledge Dr Tang Jie-Cong for the synthesis of PBTTT, NMR, GPC, DSC measurements and Figure 3.1; Rui Qi for the POM, solution UV-Vis measurements, Figure 2.5, Figure 3.2 and Figure 3.3; Jing-Mei for inducing lamellae in rrP3HT, AFM measurement of rrP3HT terraces, Figure 2.11 and Figure 2.12.

Abstract

Five-membered-ring heterocycle polymers such as regioregular poly(3-alkylthiophenes) (rrP3ATs) and poly(bithiophene-*alt*-thienothiophene) (PBTTT) are important prototype polymer organic semiconductors (OSCs) that show the high charge-carrier mobility important for both field-effect transistors (FETs) and photovoltaic (PV) applications. These typically orders into lamellae comprising π-stacked polymer chains with *anti*-coplanar rings spaced by the alkyl side-chains. This polymer morphology is suited to give high charge-carrier mobility owing to relatively fast transport in the π-stacking direction. The charge carriers are fundamentally polarons due to strong electron–phonon coupling, but they have been found to possess a significant inter-chain character, which is a subject of ongoing intense interest, because of the possibility to access highly mobile states.

PBTTT has recently been reported to give unprecedented molecular terraces on the surfaces of thin films, which suggests a more superior lamellar ordering than known in rrP3ATs. This lamellar order persists to both the air and substrate interfaces, which makes PBTTT a particularly useful model to investigate several aspects of polymer physics and charge-transport physics in ordered polymer OSCs. In this thesis, thermal excitation of the polymer and its effect on field-effect transport are studied. In particular, a novel ring-twist transition in π-conjugated polymers is established from detailed variable-temperature spectroscopy and quantum-mechanical calculations, together with a novel layered nematic transition. The effects of these ring-twist transition on the properties of the field-induced polarons and their transport density-of-states has been characterised.

In chapter 1, we give a brief introduction about the fundamentals of the organic semiconductor, properties of rrP3HT and PBTTT, followed by working mechanism of the organic field-effect transistors (OFETs), on which the charge transport property and modulation spectroscopy aspects in this thesis are based, and finally the short review of charge modulation spectroscopy (CMS).

In chapter 2, we propose a model based on the intrinsic viscosity measurement, solution ultraviolet-visible (UV-Vis) spectroscopy and atomic force microscopy to explain the origin of the molecular terrace morphology in PBTTT films. This model invokes the central role of a borderline poor solvent in promoting the early π-stacking of the polymer chains, and the subsequent deposition and growth of these π-stacks into continuous films on the substrate. The model appears to be general, as lamellae have now also been found in rrP3HT in this work. This explains the origin of the high degree of order present in PBTTT, which puts the correlation of morphology and transport physics on a firm basis.

In chapter 3, we investigated the dependence of paracrystal to liquid crystal transition and liquid crystal to isotropic phase transition in the temperature from 298 K to 500 K on molecular weight. A set of nematic phase transition (T_k‘ and T_k”) and isotropic melting (T_i) is observed in wide-angle X-ray scattering and variable temperature polarised optical microscopy measurements. The nematic phase transition and isotropic melting temperatures increase with increasing chain length and saturate for polymer chain length $n_o > 10$.

In chapter 4, we investigate the 320-K transition by variable temperature Fourier transform infrared (FTIR), Raman and UV-Vis spectroscopies. This transition is established to be a second-order cooperative ring-twist transition; denoted T_r. Quantum chemical calculations

quantitatively determined the ring-twist angles above T_r transition. Above T_r, the mean dihedral angles of the temperature-dependent vibrational and electronic spectra progressively increase from ≈ 0º to ≈ 25º just below the paracrystal to nematic phase transition (T_k), while keeping a long-range correlation that preserves a long polymer persistence length.

In chapter 5, we studied the effects of this mild T_r ring-twist transition on the interchain polaron and transport density-of-state. We demonstrate that the ring-twist transition existing in the bulk of PBTTT film has an impact on the polaron at the semiconductor/insulator interfaces. Although disorder tends to cause polaron localisation, mild ring twist in well-ordered π-stacked chains, in contrast, promotes interchain delocalisation by suppressing the electron-phonon coupling and thus favour the formation of the most delocalized interchain polarons. As a result of this thermally-induced ring twist, the transport density-of-states broaden near its centre but not in the tail where the polarons reside, and so the field-effect transistor characteristics become non-dispersive and well-behaved.

Table of Content

Table of Figures

Chapter 1. Introduction

1.1 Organic semiconductor

The scientific research and technological applications of organic electronics have witnessed phenomenal growth in the last two decades. Traditionally, plastics are known to be electrically insulating and are thus commonly used as insulator in industry. In year 2000, Alan J. Heeger, together with Alan G. MacDiarmid and Hideki.S won the Nobel Prize in Chemistry for their discovery and development of conducting polymers.[1] A group of organic semiconductor (OSC) materials, comprising of small molecules and π-conjugated polymers, is found to show the semiconducting electrical characteristics. Organic light-emitting diodes made of small molecules, by using double-layer structure consist of an aromatic diamine layer and 8-hydroxyquinoline aluminum (Alq_3) layer, and π-conjugated polymer, with poly(*p*-phenylene vinylene) (PPV) serving as active layer, have been developed in 1987 by Tang *et al.* [2] and the Cavendish laboratory [3] respectively. Initial demonstration of organic field-effect transistors (FETs) with α-conjugated oligothiophenes has been initially demonstrated by Horowitz *et al.*, [4] while FETs made of π-conjugated polymers, *e. g.* polythiophene or polyacetylene, have also been reported in 1980s by various groups. [5] [6]

The reason for the semiconducting electrical characteristics of this special group of molecules/polymers lies in their alternating single and double carbon-carbon bonds present along their backbone. The electronic structure of π-conjugated polymers results in a general delocalisation of the π-electrons across all of the adjacent parallel-aligned π-orbitals (Figure 1.1) of the atoms, and the delocalised π-electron bonding along the main chain.

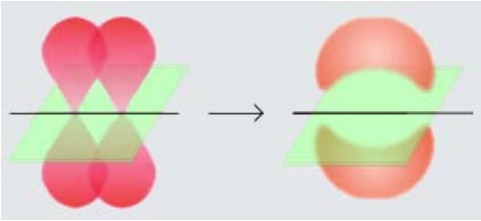

Figure 1.1 Parallel π-orbitals and π-bond

The energies of π-bonds and its anti-bonding π * are located between the σ and σ* bond. The energy difference between the π-π* bonds is defined as the energy gap of the polymers, which can be large for an insulator, but usually much smaller for a polymer that has π-conjugation. Therefore, it is possible to inject electrons and holes or excited photoexcited electron-hole pairs in these materials without causing a destruction of the polymer chain.

The introduction of charge carriers onto an isolated conjugated molecule is accompanied by a polaronic structural and electronic relaxation of the π-conjugated backbone. Figure 1.2 shows the bond alternation from benzenoid to quinoid form occuring when charges are located on the backbone. Singly charged carriers are referred to as polarons (or radical cations in the case of short oligomers) whereas doubly charged carriers are called bipolarons (dications), as shown in Figure 1.3. This relaxation results in the appearance of new optical transitions in the absorption spectrum at energies lower than the main π-π* transition. Note that transitions C3, C4, and DC2 are usually disallowed due to symmetry considerations in isolated chains.

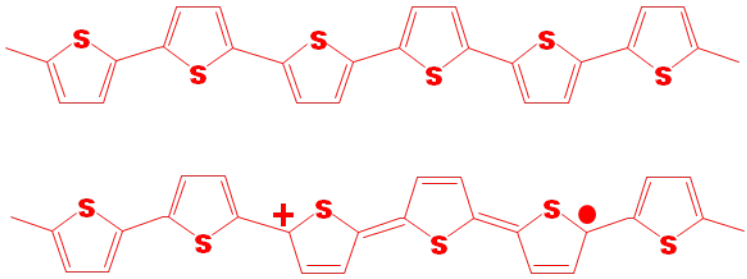

Figure 1.2 Schematics of neutral polymer π-conjugated backbone and polaron structure

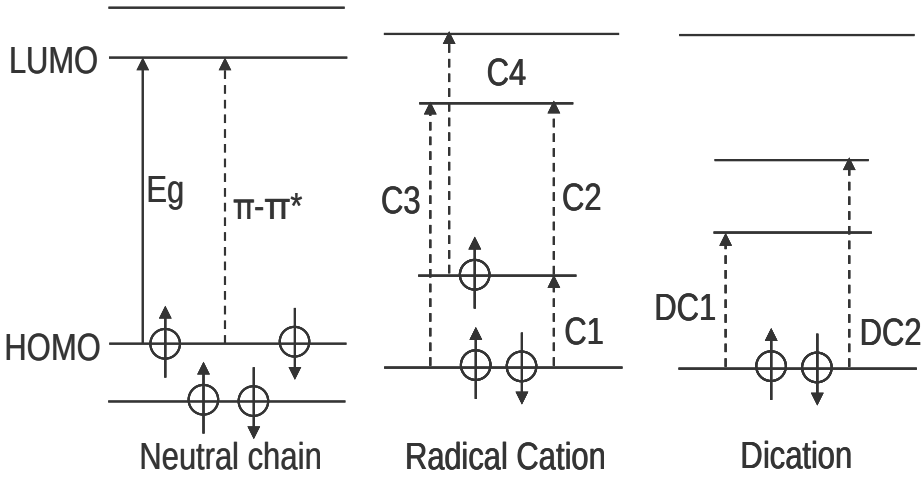

Figure 1.3 Structure and one-electron energy level diagram of radical cations and dications

1.2 Organic field-effect transistor (OFET) devices

Organic field-effect transistors (OFETs) are three-terminal devices comprising of a gate electrode, source electrode and drain electrode. The semiconductor is deposited to bridge the source and drain electrodes, and is itself spaced from the gate contact by an insulating gate dielectric layer. A source-drain voltage (V_{ds}) is applied across the drain-source electrodes while a gate voltage (V_{gs}) across the gate-source electrodes. This gate voltage provides an electrical field that leads to the accumulation of charge carriers at the semiconductor-dielectric interface. This in turn modulates the source-drain conductance for a given source-drain voltage (V_{ds}).

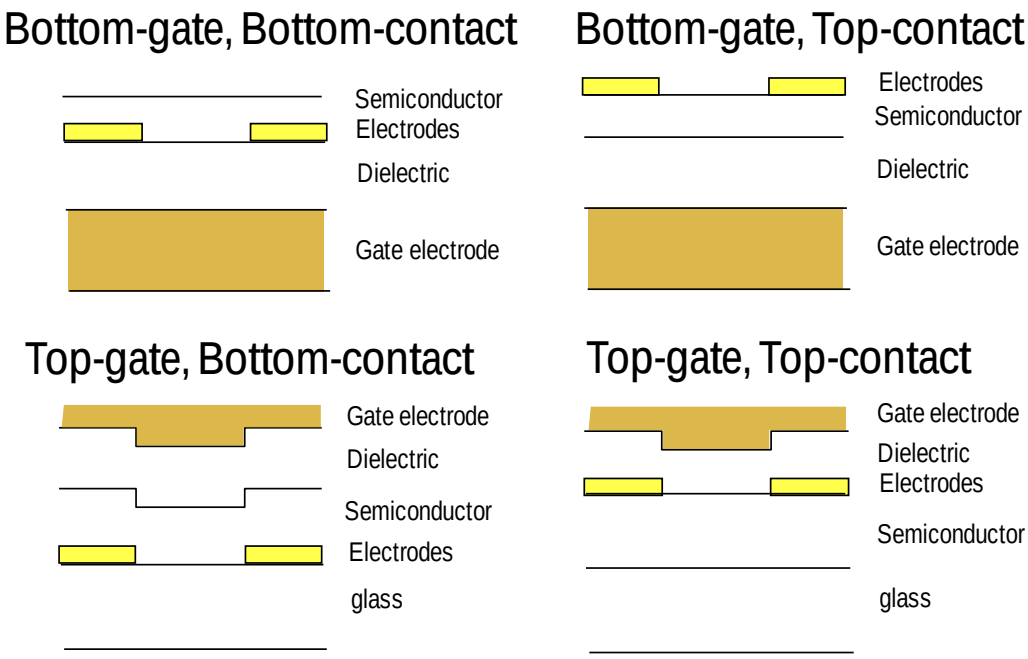

Figure 1.4 Four possible FET device configurations

There are four possible FET device configurations: bottom-gate, bottom-contact; bottom-gate, top-contact; top-gate, bottom-contact and top-gate, top-contact. (Figure 1.4) Two kinds of configurations have been used in this thesis, which are bottom-gate, bottom contact and top-gate, bottom-contact. In the bottom-gate bottom-contact configuration, Au source drain electrodes are photolithographically patterned on p^{++}-Si substrates with 200 nm of thermally grown SiO_2 as dielectric separating the Si gate and the active semiconductor layer. This configuration is commonly used to fabricate diagnostic OFETs to measure carrier mobility. In this configuration electrons/holes are injected directly into the semiconductor/dielectric interface by source-gate voltage V_{gs} and subsequently driven by the V_{sd}. In the top-gate bottom-contact configuration, the source/drain electrodes are also predefined by photolithography on glass or plastic substrate before the semiconductor is deposit. The top-gate electrode is fabricated by thermal evaporated metal. The typical field-effect characteristics, transfer characteristic (left) and output characteristic (right) are shown below (Figure 1.5).

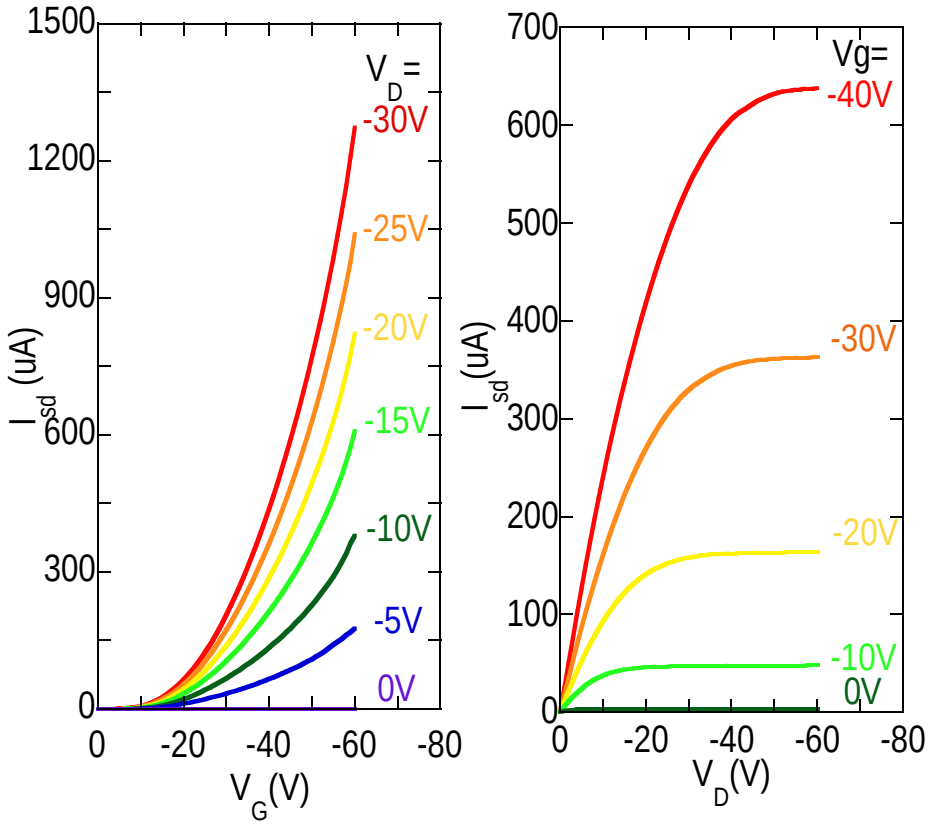

Figure 1.5 Field-effect transistor characteristics: bottom-gate, bottom-contact device using rrP3HT as semiconductor layer.

Field effect mobility can be extracted from OFET in the linear and saturation regime. In the linear regime when a small V_{ds} is applied across source-drain electrodes, the charges flowing from source to drain, the current flowing through the channel is directly proportional to V_{ds}. In this case the source-drain current I_{ds} can be described by :

$$I_{ds} = \frac{WC_i\mu_{lin}(V_{gs} - V_{gs,th})V_{ds}}{L}$$

Where L is the channel length, W is the channel width, C_i is the capacitance per unit area of the insulator, $V_{gs,th}$ is the threshold voltage, and μ_{lin} is the liner field-effect mobility, which can be calculated by plotting I_{ds} versus V_{gs} at a constant V_{ds}, when $|V_{ds}| < |V_{gs} - V_{gs,th}|$. The $V_{gs,th}$

depends on the charge carrier trapping at the interfaces and the nature of the semiconductor/dielectric interface.

When $|V_{ds}| > |V_{gs} - V_{gs,th}|$, source-drain current begins to saturate due to the pinch-off of the accumulation layer near the drain electrode and can be given by:

$$I_{ds} = \frac{WC_i \mu_{sat} (V_{gs} - V_{gs,th})^2}{2L}$$

where μ_{sat} can be calculated by plotting $\sqrt{I_{ds}}$ versus V_{gs}. The saturation mobility is usually higher than the liner mobility, which is speculated to be artifact due to contact resistance.

1.3 **High mobility π**-conjugated polymer: polythiophene family

π-conjugated polymers with highly extended π-conjugation in their conjugated backbone have attracted considerable attention from both fundamental and practical points of view. Thiophene-contaning polymers, among π-conjugated polymer family, have exhibited amongst the highest charge carrier mobility from OFETs. In these materials, thiophene rings are coupled together on their 2nd and 5th positions. Alkyl side-chains on the thiophene rings promote solubility in organic solvents. These polymers thus can form uniform films through solution processable methods, such as spin-casting, drop-casting and inject printing. The thiophene rings are conjugated together in a co-planar conformation to provide a delocalised electronic system, and a molecular configuration to achieve highly crystalline thin films. The first semicrystalline polythiophene polymer to give high charge-carrier mobility up to 0.1 $cm^2V^{-1}s^{-1}$ is regioregular poly(3-hexylthiophene) (rrP3HT),[7] fundamental properties of which have been extensively studied since 1980s.

1.3.1 Poly(3-hexylthiophene)

Regioregular poly(3-alkylthiophene)s (rrP3ATs) is an important family of π-conjugated polymer organic semiconductors that shows a relatively small bandgap, a strong propensity to π-stack resulting in a well-ordered morphology and hence high charge-carrier mobility. Therefore this family, in particular regioregular poly(3-hexylthiophene) (rrP3HT) (chemical structure shown in Figure 1.6), has emerged to be the most widely studied polymer OSC model for both fundamental structure–property characterizations[7-17] and also for field-effect transistors (FETs)[15,18] and photovoltaic (PV) device investigations.[19 20]

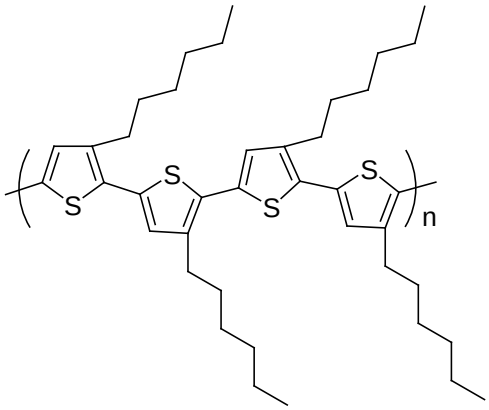

Figure 1.6 Chemical structure of rrP3HT

Thermochromism: rod-to-coil transition

Thermochromism of poly(3-alkylthiophene)s (P3ATs) were discovered by Yoshino group[21] and Ingänas group[22], who found that the colours of both the solutions and films of P3AT change remarkably as temperature increases over a broad temperature range, and this was a reversible transition. They attributed this observation to a transition of polymer conformation from a rigid rod geometry at low temperature to a random coil conformation at higher temperature, which is widely known as rod-to-coil transition.

This explanation has been further supported by various spectroscopy measurements done by a few other groups in the next decade. Tashiro *et al.* suggested that the transformation from *trans* to gauche configuration in alkyl side-chains triggers the torsional motion between thiophene-thiophene rings which further results in the structural disordering of the π-conjugated backbone,[23] indicated by differential scanning calorimetry (DSC) thermograms, temperature-dependent X-ray diffraction (XRD), Fourier transform infrared spectroscopy (FTIR) and Ultraviolet-visible (UV-vis) spectroscopy on material. Detailed study of variable temperature vibrational spectroscopies of alkyl side-chains of P3ATs and their model compounds have been performed by Zerbi *et al.*, and they found the existence of ring twisting structure in the chain backbone which is also supported by the effective conjugation coordinate theory; however the deviation from the planar state is very small.[24]

In these studies, a thermal blue shift of the π–π* transition has been found below this thermochromism transition, which indicates a different structure at higher temperature with decreased effective conjugation length.[24] This transition is also sensitive to the substitution pattern and related to the formation of delocalised conformation defects with increasing temperature, which is denoted as “twiston”.[25] Moreover, in regioregular polymers (more than 90% head-to-tail) with short alkyl side-chains, a continuous themochromic blue shift of the π–π* transition was observed, instead of isobestic behavior obtained in regiorandom P3ATs, which is speculatively assigned to the equilibrium among crystalline, quasi-ordered and disordered phases. [26,27]

Analogous to glass transition, the thermochromism transition discovered in P3ATs has been attributed to a variety of polymorphic and mesophase transitions reported by a few groups. Interlayer interdigitation of the side-chains has been reported which incorporate to the liquid

crystalline state upon modest annealing of rr-P3AT films, supported by temperature-dependent X-ray diffraction.[28] The influence of the molecular weight was reported to be more significant than alkyl side-chain effect on the crystallization of rr-P3AT films which form a 2D mesomorphic phase with the anti-coplanar polythiophene π-conjugated backbone lying roughly edge-on parallel to the film surfaces while alkyl side-chains are approximately orthogonal to the substrate.[29] In order to further investigate the nature of polymophism and phase stability of rr-P3AT, detailed measurements has been performed, such as DSC, nuclear magnetic resonance (NMR), XRD, photoluminescence and Raman scattering, by which a transition at *ca*. 80 °C resulting from the side-chain disordering and at *ca*. 130 °C subsequently due to the change in π-conjugated backbone was concluded.[29,30] The transition temperatures of rr-P3ATs, temperature at which the films undergo an ordered to nematic phase transition, were found to be decrease as the length of alkyl side-chains increase.[31] More detailed phase transition diagram of P3ATs has also been proposed, which indicate the existence of a glass transition in the liquid crystalline phase due to the thiophene ring twist.[32]

Morphology of rrP3HT: nanowhiskers

The morphology of organic semiconductor polymers is central to the charge transport in organic semiconductors, since all the charge transport in FET occurs within a few nanometers at the semiconductor-dielectric interface. Moreover, for π-conjugated polymers, the π-conjugated backbones are favorably laying parallel to the surface to provide good charge transport. Therefore, the in-plane charge transport might be expected to be better. When the π-conjugated backbones become partially disordered, the delocalisation of charge carriers over a few neighbouring molecules dominates. As a result, the π-packing becomes crucial since charges are traveling through the interface by hopping between two molecules along the π-packing direction.

Whiskers of rrP3HT have been reported in 1993 by Ihn *et al.*.[33] Tansmission electron microscopy (TEM) shows rrP3HT ribbon-like whiskers (Figure 1.7) formed from diluted solution in poor solvents, such as cyclohexanone and *n*-decane by heating up the solution up to certain temperature to completely dissolve rrP3HT before cooling down to room temperature. The width of the whiskers always shows 15 nm, while the lengths are often tens of micrometers. Therefore, the author concluded an arrangement of folded polymer chains along the lengthwise edges of the whiskers within a single whisker. The proposed packing of rrP3HT by the author is shown in Figure 1.8.

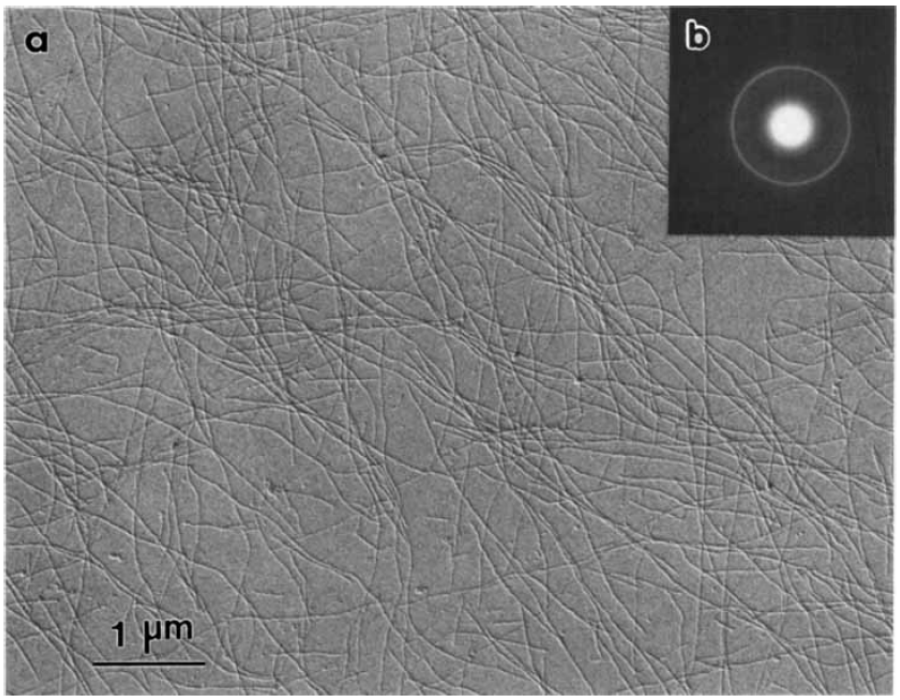

Figure 1.7 (a) TEM of rrP3HT whiskers grown from cyclohexanone solution; (b) corresponding electron diffraction pattern. [33]

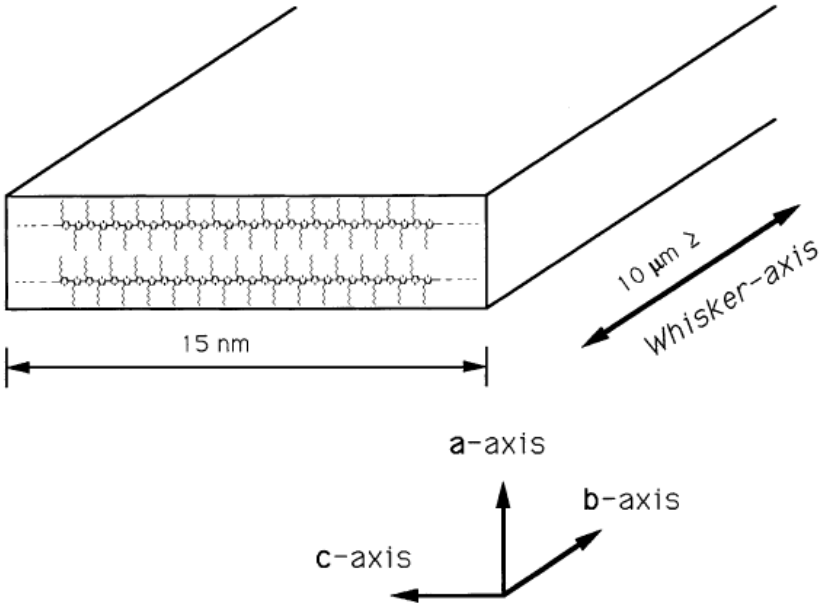

Figure 1.8 Schematic representation of the molecular arrangement within rrP3HT whiskers [33]

Numerous studies of morphological dependence of rrP3HT on solvent, molecular weight and casting method have been reported subsequently.[34,35] Kline group[10,13] showed that low-molecular-weight (MW) rrP3HT can give whiskers and fibrils from various solvent, such as chloroform, and xylene, by both drop-casting and spin-casting. High-MW rrP3HT however gave an isotropic nodular morphology. This observation is also supported by XRD and atomic force microscopy (AFM) phase images, and the models to explain the chain-packing suggests that low-MW polymer molecules behave like highly-ordered rigid rods along the nanorod short axis, while high-MW rrP3HT molecules form small ordered areas with a few bends within a polymer backbone (Figure 1.9).

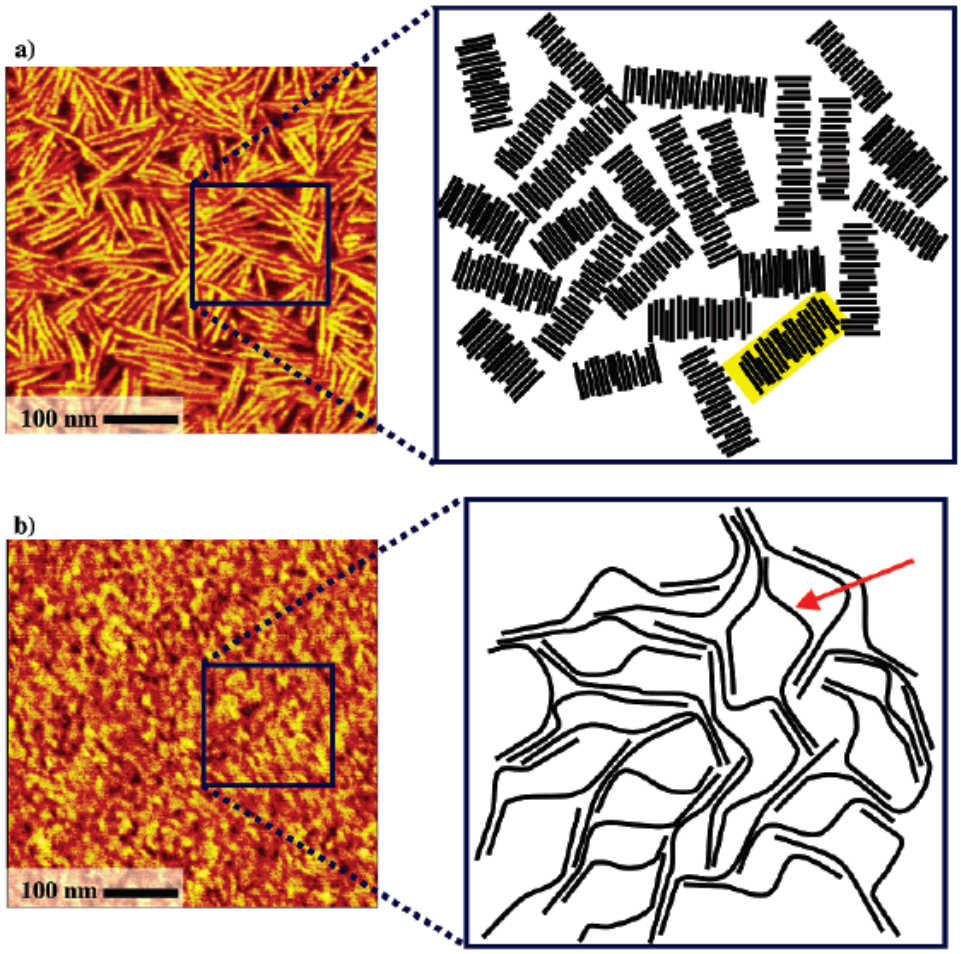

Figure 1.9 AFM images and models for chain-packing in rrP3HT films. (a) Low-MW rrP3HT and (b) high-MW rrP3HT. [10]

Recently, it was shown that even high-MW-rrP3HT can give the whisker or fibrillar morphology if the material is deposited by slow evaporation using a high boiling point solvent, e.g. trichlorobenzene. [18,36] The length of the nanofibers increases rapidly with increasing MW and reaches an apparent plateau in the median MW (about 29 kD to 52 kD), which is attributed to the strong π-stacking interaction between chains. Poor solvent was reported to be able to induce ribbon-like whiskers in high-MW rrP3HT. [37] The typical width of *ca*. 15 nm were observed in the studies listed above for high-MW rrP3HT, which is shorter than the contour length of the chains, suggesting the chains must fold to be accommodated within the whisker.

However, rrP3HT nanowire consists of more extended chains width more than 20 nm induced by controlling solvent vapor pressure [38] and mixed solvent (good solvent mixed with poor solvent, such as anisole) [39] was also suggested. In those reports, the height of the nanowire indicated that there are 2-3 layers of polymer backbone edge-on stacking parallel to the surface and perpendicular to the long axis of the nanowire. These folded-chain crystals or fringed-micelle crystals have also been well-established in high-MW material, by TEM, and also the expected crystal thickening effect in Hoffman–Weeks plot of melting temperature *vs* isothermal annealing.[40,41] The polymer chain folds involve several *cis* conformation of the thiophene rings, and have been visualized by scanning tunneling microscopy.[42]

1.3.2 Liquid-crystalline semiconducting polymer: Poly(bithiophene–alt-thienothiophene) (PBTTT)

Recently, it has been shown that by reducing the side-chain density on the polythiophene backbone, or by incorporating fused thienothiophene rings, this π-stacking can be further enhanced to improve charge-carrier transport properties.[43,44] Moreover, the presence of unsubstituted thiphene rings along the backbone was shown to increase the ionization potential (IP), [45] which further improved the air ability of the material as compared to rrP3HT.

Poly[2,5-bis(3-alkylthiophene-2-yl)thieno[3,2-b]thiophene-2,5-diyl] (PBTTT) was reported recently to exhibit higher mobility than other polymers in polythiophene family (chemical structure shown in Figure 1.10).[46] PBTTT shows a liquid-crystalline phase (LCP) from which far more highly-ordered lamellae can be obtained upon annealing from a worm-like morphology, as shown in Figure 1.12.[47] [44,46] The molecular height of PBTTT lamella indicates the edge-on

packing of the polymer with π-conjugated backbone parellel with the substrate surface (Figure 1.11). [47] However, TEM images showed that nanometer-scale ultrastructures can be found in large terraces which indicated a distribution of local chain environments.[48]

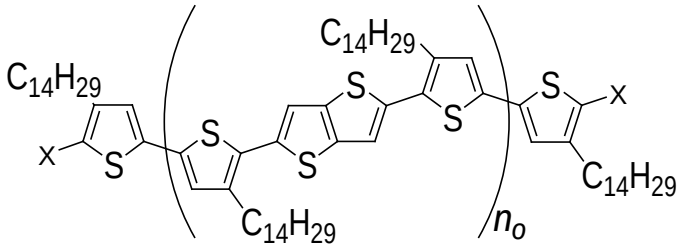

Figure 1.10 Chemical structure of PBTTT

In contrast to rrP3HT which gives folded-chain lamellae[18] with mixed orientation in the film bulk[7,9,14] and at the film surface [15,49] which complicates any attempt to correlate with field-effect charge-carrier mobility, PBTTT gives molecularly-thin lamellae comprising of π-stacks of entire chains parallel to the film plane, which persist to both substrate and air interfaces. This provides therefore large well-oriented lamellar paracrystals in which the correlation between FET mobility μ_{FET} and thermal excitation of the π-conjugated chains can be properly investigated. Atomic-force microscopy (AFM) and grazing-incidence X-ray diffraction have shown that these lamellae are oriented exclusively parallel to the film plane.[44,46] We have confirmed from AFM here that this is true even of the first (sub)monolayer at the substrate interface .

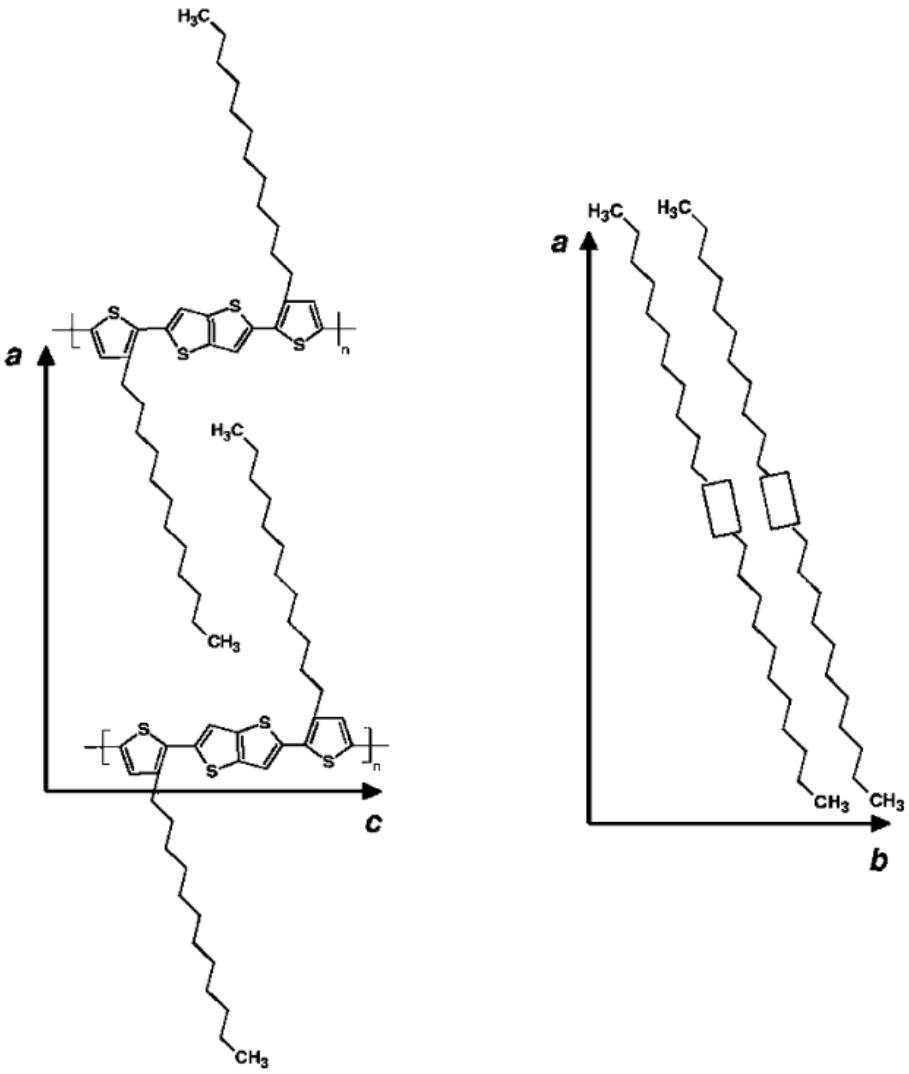

Figure 1.11 Schematic of molecular packing of PBTTT. Lamellar stacking due to the alkyl side chains occurs along the a-axis, and π-stacking occurs along the b-axis. The positions of the molecules in the cell are qualitative and are not meant to quantitatively describe the details of the molecular packing, e.g., the extent of interdigitation of thesidechains. [44] However, the work in this thesis will demonstrate that no side-chain interdigitation exist. In fact the side-chains are significantly disordered at room temperature.

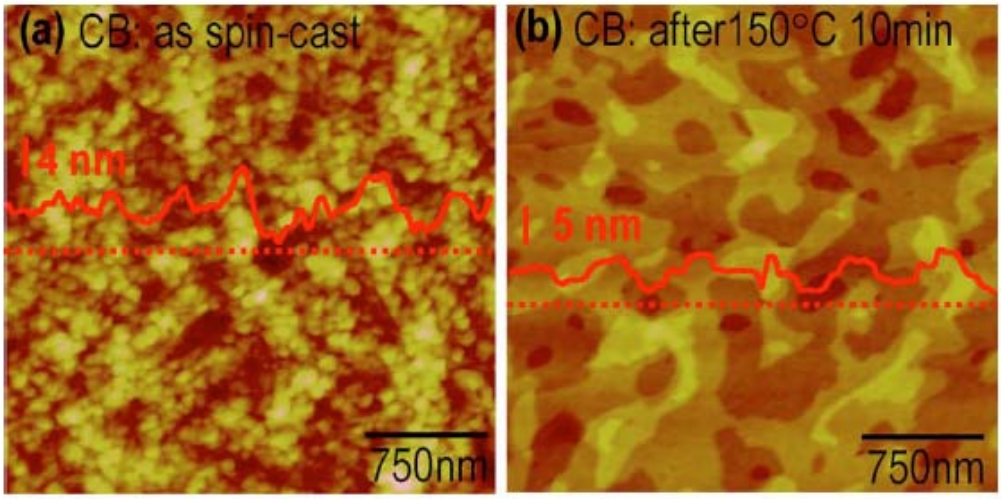

Figure 1.12 AFM images of 20-nm-thick PBTTT film on OTS treated SiO2 substrate. (a) As-spin-cast chlorobenzene film. (b) After anneling chlorobenzene film. [47]

A set of detailed studies has shown that before its isotropic melting, PBTTT film gives a well-defined cooperative ring-twist transition followed by a melting transition to the nematic liquid crystalline phase. Nematic liquid crystalline phase has nematic order within the lamellae (i.e., only orientation order of the mesogen director (chains) that are perpendicular to the lamellae, with no long-range periodicity in any direction in plane) but a crystalline order in the lamellar direction. PBTTT is also more air-stable than rrP3ATs on storage and during operation. [47,50] The better air-stability of PBTTT is due to the more tightly packing of the π-conjugated backbone of PBTTT than in rrP3HT, which has been pointed out earlier to explain the higher resilience of PBTTT to photo-induced doping in the presence of oxygen and moisture. [51] This is related to the well-known smectic phase in which a layered periodicity is maintained but with the mesogen director perpendicular to the lamellae and with positional order within the lamellae.

1.4 Charge modulation spectroscopy

The characteristics of the charge carriers are central to the properties of these organic semiconductors. Here the charges are localised polarons self-trapped by a strong electron-phonon coupling, which leads to subgap states, as well as hopping transport. In order to probe the cationic charge carriers in π-conjugated polymers, extra charges need to be introduced to the π-conjugated backbone. One conventional technique used to obtain optical information of the nature of charge carriers is chemical doping. The π-conjugated polymers are positively doped with a certain oxidising agent to remove electronic charges from the polymer chains. And the spectrum of chemical doping is usually done in solution phase. In 1998, van Haare *et al.* used thianthrenium perchlorate to dope substituted oligothiophenes (6, 9 and 12 thiophene units) in dichloromethane solution, which produced optical evidence of single polaron and bipolaron. As thiophene chains get longer, the presence of two individual polarons rather than a bipolaron on a single chain was observed. [52]

The disadvantage of chemical doping technique is that it introduces a counter-ion into the π-conjugated system, which may cause further complication to the study of π-conjugated polymer. Charge modulation spectroscopy (CMS) is a powerful electro-optical experimental technique to directly probe the charge carriers present in the conducting layer of FET and other device structures, such as metal-insulator-semiconductor (MIS) device, using injected charge without the presence of counter ions.

Ziemelis *et al.* [53] measured CMS on thin films of region-random P3HT and assigned the features observed to those of polarons and bipolarons predicted by the one-dimensional FBC model. Harrison *et al*., [54] have done an extensive CMS measurements which provided the evidence for weak interchain interactions in oligothiophene with six thiophene rings, which

results in a transverse bipolaron (π-dimer). CMS technique has been used to study the charge carriers present in the conducting channels of rrP3HT FETs by Brown *et al.* [55,56]. They demonstrated that the CMS spectra of charge carriers in high mobility rrP3HT FETs were independent of charge density, modulation frequency and temperature, so as to prove the presence of a single, intrinsic charge carrier as a single charged polaronic species. Their results also gave evidence that interchain coupling in highly ordered rrP3HT is sufficiently strong so charge carriers cannot be considered to be confined to a single chain; rather, they exhibit quasi-two-dimensional characteristics.

1.5 References

1 Heeger, A. J. Nobel Lecture: Semiconducting and metallic polymers: The fourth generation of polymeric materials. *Rev. Mod. Phys.* 73, 681-700 (2001).

2 Tang, C. W. & VanSlyke, S. A. Organic electroluminescent diodes. *Appl. Phys. Lett.* 51, 913-915 (1987).

3 Bourroughes, J. H. *et al.* Light-emitting diodes based on conjugated polymers. *Nature* 347, 539-541 (1990).

4 Horowitz, G., Peng, X. Z., Fichou, D. & Garnier, F. A field-effect transistor based on conjugated alpha-sexithienyl. *Solid State Commun.* 72, 381-384 (1989).

5 Koezuka, H., Tsumura, A. & Ando, T. Field-effect transistor with polythiophene thin film. *Synth. Met.* 18, 699-704 (1987).

6 Bourroughes, J. H., Jones, C. A. & Friend, R. H. New semiconductor device physics in polymer diodes and transistors. *Nature* 335, 137-141 (1988).

7 Sirringhaus, H. *et al.* Two-dimensional charge transport in self-organized, high-mobility conjugated polymers. *Nature* 401, 685-688 (1999).

8 McCullough, R. D., Tristram-Nagle, S., Williams, S. P., Lowe, R. D. & Jayaraman, M. Self-orienting head-to-tail poly(3-alkylthiophenes): new insights on structure-property relationships in conducting polymers. *J. Am. Chem. Soc.* 115, 4910-4911 (1993).

9 Aasmundtveit, K. E. *et al.* Structural anisotropy of poly(alkylthiophene) films. *Macromolecules* 33, 3120-3127 (2000).

10 Kline, R. J., McGehee, M. D., Kadnikova, E. N., Liu, J. & Fréchet, J. M. J. Controlling the field-effect mobility of regioregular polythiophene by changing the molecular weight. *Adv. Mater.* 15, 1519-1522 (2003).

11 Brown, P. J. *et al.* Effect of interchain interactions on the absorption and emission of poly(3-hexylthiophene). *Phys. Rev. B* 67, 064203 (2003).

12 Bolognesi, A. *et al.* Structural features in aligned poly(3-alkylthiophene) films revealed by grazing incidence x-ray diffraction. *Polymer* 45, 4133-4138 (2004).

13 Kline, R. J. *et al.* Dependence of regioregular poly(3-hexythiophene) film morphology and field-effect mobility on molecular weight. *Macromolecules* 38, 3312-3319 (2005).

14 Kline, R. J., McGehee, M. D. & Toney, M. F. High oriented crystals at the buried interface in polythiophene thin-film transistors. *Nature Mater.* 5, 222-228 (2006).

15 Ho, P. K. H. *et al.* Solvent effects on chain orientation and interface pi-interaction in conjugated polymer thin fims: Direct measurements of the air and substrate interfaces by near-edge x-ray absorption spectroscopy. *Adv. Mater.* 19, 215-221 (2007).

16 Gurau, M. C. *et al.* Measuring molecular order in poly(3-alkylthiophene) thin films with polarising spectroscopies. *Langmuir* 23, 834-842 (2007).

17 Clark, J., Silva, C., Friend, R. H. & Spano, F. C. Role of intermolecular coupling in the photophysics of disordered organic semiconductors: aggregate emission in regioregular polythiophene. *Phys. Rev. Lett.* 98, 206401-206404 (2007).

18 Chang, J. F. *et al.* Molecular-weight dependence of interchain polaron delocalisation and exciton bandwidth in high-mobility conjugated polymers. *Phys. Rev. B* 74, 115318-115311-115312 (2006).

19 Kim, Y. *et al.* A strong regioregularity effect in self-organizing conjufated polymer films and high-efficiency polythiophene:fullerene solar cells. 5, 197-203 (2006).

20 Ballantyne, A. M. *et al.* The effect of poly(3-hexylthiophene) molecular weight on charge transport and the performance of polymer:fullerene solar cells. *Adv. Funct. Mater.* 18, 2373-2380 (2008).

21 Yoshino, K., Nakajima, S., Park, D. H. & Sugimoto, R.-I. Thermochromism, photochromism and anomalous temperature dependence of luminescence in poly(3-alkylthiophene) film. *Jpn. J. Appl. Phys.* 27, L716-L718 (1988).

22 Ingänas, O., Gastafsson, G., Salaneck, W. R., Österholm, J.-E. & Laakso, J. Thermochromism in thin films of poly(3-alkylthiophenes). *Synthetic Met.* 28, C377-384 (1989).

23 Tashiro, K. *et al.* Structure and thermochromic solid-state phase transition of poly(3-alkylthiophene). *J. Polym. Sci. B Polym. Phys.* 29, 1223-1233 (1991).

24 Zerbi, G., Chierichetti, B. & Inganäs, O. Thermochromism in polyalkylthiophenes: molecular aspects from vibrational spectroscopy. *J. Chem. Phys.* 94, 4646-4658 (1991).

25 Roux, C. & Leclerc, M. Thermochromic properties of polythiophene derivatives: formation of localized and delocalized conformational defects. *Chem. Mater.* 6 (1994).

26 Zerbi, G., Chierichetti, B. & Ingänas, O. Thermochromism in polyalkylthiophenes: molecular aspects from vibrational spectroscopy. *J. Chem. Phys.* 94, 4646-4658 (1991).

27 Yang, C., Orfino, F. P. & Holdcroft, S. A phenomenological model for predicting thermochromism of regioregular and noregioregular poly(3-alkylthiophenes). *Macromolecules* 29, 6510-6517 (1996).

28 Prosa, T. J., Winokur, M. J. & McCullough, R. D. Evidence of a novel side chain structure in regioregular poly(3-alkylthiophenes). *Macromolecules* 29, 3654-3656 (1996).

29 Meille, S. V. *et al.* Influence of molecular weight and regioregularity on the polymorphic behavior of poly(3-decylthiophenes). *Macromolecules* 30, 7898-7905 (1997).

30 Baolognesi, A. *et al.* Structural and thermal behaviour of poly(3-octylthiophene): a DSC, ^{13}C MAS NMR, XRD, photoluminescence and Raman scattering study. . *Macromol. Chem. Phys.* 202, 2586-2591 (2001).

31 Causin, V., Marega, C., Marigo, A., Valentini, L. & Kenny, J. M. Crystallization and melting behavior of poly(3-butylthiophene), poly(3-octylthiophene) and poly(3-dodecylthiophene). *Macromolecules* 38, 409-415 (2005).

32 Yazawa, K., Inoue, Y., Yamamoto, T. & Asakawa, N. Twist glass transition in regioregulated poly(3-alkylthiophene). *Phys. Rev. B* 74 (2006).

33 Ihn, K. J., Moulton, J. & Smith, P. Whiskers of poly(3-alkylthiophene)s. *J. Polym. Sci. Part B: Polym. Phys.* 31, 735-742 (1993).

34 Zen, A. *et al.* Effect of molecular weight and annealing of poly(3-hexylthiophene)s on the performance of organic field-effect transistors. *Adv. Funct. Mater.* 14, 757-764 (2004).

35 Zhang, R. *et al.* Nanostructure dependence of field-effect mobility in regioregular poly(3-hexylthiophene) think film field effect transistors. *J. Am. Chem. Soc.* 128, 3480-3481 (2006).

36 Chang, J. F. *et al.* Enhanced mobility of poly(3-hexylthiophene) transistors by spin-casting from high-boiling-point solvents. *Chem. Mater.* 16, 4772-4776 (2004).

37 Liu, J., Arif, M., J., Z., Khondaker, S. I. & Zhai, L. Controlling poly(3-hexylthiophene) crystal demension: nanowhiskers and nanoribbons. *Macromolecules* 42, 9390-9393 (2009).

38 Kim, D. H., Park, Y. D., Jang, Y., Kim, S. & Cho, K. Solvent vapor-induced nanowire formation in poly(3-hexylthiophene) thin films. *Macromol. Rapid Commun.* 26 (2005).

39 Samitsu, S., Shimomura, T., Heike, S., Hashizume, T. & Ito, K. Effective production of poly(3-akylthiophene) nanofibers by means of whisker method using anisole solvent: structural, optical, and electrical properties. *Macromolecules* 41, 8000-8010 (2008).

40 Malik, S. & Nandi, A. K. Crystallization mechanism of regioregular poly(3-alkyl thiophene)s. *J. Polym. Sci. B, Polym. Phys.* 40, 2073-2085 (2002).

41 Hugger, S., Thomann, R., Heinzel, T. & Thurn-Albrecht, T. Semicrystalline morphology in thin films of poly(3-hexylthiophene). *Colloid Polym. Sci.* 2004, 932-938 (2004).

42 Mena-Osteritz, E. *et al.* Two-dimensional crystals of poly(3-alkylthiophene)s: direct visualisation of polymer folds in submolecular resolution. *Angew. Chem. Int. Ed.* 39, 2680-2684 (2000).

43 Heeney, M. *et al.* Stable polythiophene semiconductors incorporting thieno[2,3-b]thiophene. *J. Am. Chem. Soc.* 127, 1078-1079 (2005).

44 Chabinyc, M. L., Toney, M. F., Kline, R. J., McCulloch, I. & Heeney, M. X-ray scattering study of thin films of poly(2,5-bis(3-alkylthiophen-2-yl)thieno[3,2-b]thiophene). *J. Am. Chem. Soc.* 129, 3226-3237 (2007).

45 McCulloch, I. *et al.* Influence of molecular design on the field-effect transistor characteristics of terthiophene polymers. *Chem. Mater.* 17, 1381-1385 (2005).

46 McCulloch, I. *et al.* Liquid-crystalline semiconducting polymers with high charge-carrier mobility. *Nature Mater.* 5, 328-333 (2006).

47 Wang, S. *et al.* Solvent effects and multiple aggregate states in high-mobility organic field-effect transistors based on poly(bithiophene-alt-thienothiophene). *Appl. Phys. Lett.* 93, 162101-162103 (2008).

48 Wang, C. *et al.* Microstuctual origin of high mobility in high-perfomance poly(thieno-thiophene) thin-film transistors. *Adv. Mater.* 22, 697-701 (2010).

49 DeLongchamp, D. M. *et al.* Variations in semiconducting polymer microstructure and hole mobility with spin-coating speed. *Chem. Mater.* 17, 5610-5612 (2005).

50 Umeda, T., Tokito, S. & Kumaki, D. High-mobility and air-stable organic thin-film transistors with highly ordered semiconducting polymer films. *J. Appl. Phys.* 101, 054511-054515 (2007).

51 Zhuo, J. M. *et al.* Direct spectroscopic evidence for a photodoping mechanism in polythiophene and poly(bithiophene-alt-thienothiophene) organic semiconductor thin films involving oxygen and sorbed moisture. *Adv. Mater.* 21, 4747-4752 (2009).

52 vanHaare, J. A. E. H. *et al.* Redox states of long oligothiophenes: two polarons on a single chain. *Chem. Eur. J.* 4, 1509-1522 (1998).

53 Ziemelis, K. E. *et al.* Optical Spectroscopy of Field-Induced Charge in Poly(3-hexyl thienylene) Metal-Insulator-Semiconductor Structures - Evidence For Polarons. *Phys. Rev. Lett.* 66, 2231 (1991).

54 Harrison, M. G., Fichou, D., Garnier, F. & Yassar, A. In Situ Charge-Modulation Spectroscopy of Oligothiophene Field-Effect Diodes: From Sexithiophene Towards Polythiophene. *Opt. Mater.* 9, 53 (1998).

55 Brown, P. J., Sirringhaus, H. & Friend, R. H. Electro-optical characterisation of field effect devices with regioregular poly-hexylthiophene active layers. *Synth. Met.* 101, 557-560 (1999).

56 Brown, P. J., Sirringhaus, H., Harrison, M., Shkunov, M. & Friend, R. H. Optical spectroscopy of field-induced charge in self-organized high mobility poly(3-hexylthiophene). *Phys. Rev. B* 63 (2001).

Chapter 2. The origin of the monolayer-terraced morphology in PBTTT films

In this chapter, we propose here a model to explain the formation of large terraces in PBTTT films, which suggests that this morphology can be general. Key evidences steps have been obtained from measurements of the Mark–Houwink–Sakurada exponent, variable-concentration and variable-temperature solution-state UV-Vis spectroscopy and atomic force microscopy. Furthermore, we have employed a series of well-defined molecular-weight PBTTT oligomers and polymers with the degree of polymerization n_0 between 3–22 to probe the chain-length dependence of these steps. The results suggest that pre-ordering of the π-stacked aggregates in a borderline poor solvent is central to the development of the extended chain lamellar morphology. We demonstrate that this is general also for regioregular poly(3-hexylthiophene).

2.1 Introduction

The alkyl-substituted PBTTT has been reported recently, and films of this material give unprecedentedly large terraces with monolayer step heights and high hole field-effect mobility μ_{FET}.[1] This well-oriented lamellar morphology persists to both substrate and air interfaces, which makes it particularly suitable for investigating the correlation between charge transport at semiconductor dielectric interface and structural excitations of the π-conjugated polymer backbone.

Such a monolayer lamellar morphology has not previously been observed in rrP3HT film despite numerous studies of its morphological dependence on solvent, molecular weight and casting method.[2] [3-6] Low-molecular-weight (low-MW) rrP3HT for example gives whiskers and fibrils in which the chains traverse the short axis and π-stack along the long axis. High-MW rrP3HT however usually gives a nodular morphology, of which very little is known. Recently, it was shown however that even high-MW-rrP3HT can give the whisker or fibrillar morphology if the material is deposited by slow evaporation using a high boiling point solvent[7,8] or a poor solvent. [9] The typical width of these whiskers and fibrils is *ca*. 15 nm, which is shorter than the contour length of the chains, so the chains must fold to be accommodated within the whisker. [4,8] This gives the folded-chain lamellar crystal in which at least 2–3 π-stacked lamellae occur together connected by the folds. rrP3HT nanowire consist of more extended chains with width more than 20 nm induced by solvent vapor pressure [10] and mix solvent[11] was also suggested, although the hight of the nanowire indicated there are 2-3 layers of polymer backbone edge-on stacking parallel to the surface and perpendicular to the long axis of the nanowire. These folded-chain crystals or fringed-micelle crystals have been well-established in high-MW material by TEM, and also the expected crystal thickening effect in Hoffman–Weeks plot of

melting temperature *vs* isothermal annealing.[12,13] Therefore, the monolayer although nominally identical to PBTTT except for the side-chain density and the presence of the stiff thienothiophene-2,5-diyl unit, gives a completely different morphology for its π-stacks with limited size and orientational order in the film plane. Yet it seems desirable to achieve the extended chain lamellae morphology in general. Therefore, we sought to understand the origins of this unusual morphology in PBTTT.

2.2 Experimental methods

2.2.1 Synthesis of PBTTT polymers

The PBTTT polymers were synthesised broadly following the McCulloch route[1] using Stille coupling, but with thermal instead of microwave heating, and partially endcapping with phenyl to avoid reactive end groups. Recrystallized 5,5'-dibromo-4,4'-bis(tetradecyl)-2,2'-bithiophene (purity > 99.8%; 1000 mg, 1.40 mmol) was mixed with recrystallized 2,5-bis(trimethylstannyl)thieno[3,2-b]thiophene (purity > 99.8%) and tris(dibenzylideneacetone)dipalladium (26 mg, 2 mol equiv%), and tri(*o*-tolyl)phosphine (68mg, 16 mol equiv%) in a round-bottom flask, and flushed with N_2. Chlorobenzene (24 mL) was added also under continuous N_2 flow at room temperature, and then heated with stirring to 130°C (bath temperature) for 20 h. In order to generate four batches PBTTT of different molecular weight, various weight of 2,5-bis(trimethylstannyl)thieno[3,2-b]thiophene was used [50 mg (1.40 mmol); 890 mg (1.27 mmol); 541 mg (1.16 mmol) and 433 mg (0.93 mmol)]. The polymers formed were then nominally end-capped with trimethylstannylbenzene of different volume (25 μL (0.14 mmol); 50 μL (0.28 mmol); 100 μL (0.56 mmol); 190 μL (1.07 mmol)) and heated at 130 °C for another 20 h. For the highest MW PBTTT, bromobenzene

(28 μL, 0.28 mmol) was also added and heated for another 20 h to endcap the trimethylstannyl ends. The reaction mixture was cooled to 50 °C, and the polymer was precipitated into a stirred mixture of methanol (200 mL) and concentrated hydrochloric acid (15 mL) at room temperature. The precipitate was filtered and Soxhlet extracted with methanol and acetone for 24 h each in the dark and under nitrogen to obtain the purified material. ^{1}H NMR confirmed the purity of the final products.

2.2.2 Intrinsic viscosity measurement

In order to extract a few parameters, we performed intrinsic viscosity measurement of PBTTT. Intrinsic viscosities of PBTTT solutions were measured on a Viscolab 450 (Cambridge Viscosity) laboratory viscometer. Variable concentrations of PBTTT solutions (1mg/ml, 2mg/ml, 3mg/ml and 4mg/ml) were prepared in chlorobenzene and cooled down from 85°C for 30min. The average viscosity value was taken over 10 readings and the temperature was controlled at 20.8°C ± 0.1°C during each measurement.

2.2.3 Solution UV-vis-NIR absorption spectroscopy.

Absorption spectra were obtained using a diode-array UV-vis spectrograph (DW1024, Ocean Optics). Solution-state spectra were collected through 1.0-cm-pathlength cuvette or photolithography patterned spacer optical pathlength between two fused silica plates between 100μm to 2μm. The solution in the thin-film cell was briefly annealed at 75ºC, and then cooled to room temperature. No difference in spectra was found over 5–10 min and so they are characteristic of concentration alone.

2.3 Results and discussions

2.3.1 Determination of the true polymer chain length by NMR

In the literature, it is a usual practice to report polymer MWs using gel-permeation chromatography (GPC) with polystyrene as MW standards. This method incurs a sizeable systematic error due to the marked differences in their Kuhn segment length, which is thus acceptable only for relative comparisons. Here we wish to determine the true number average molecular weight n_o. We used ^{1}H NMR determination of the end units in $CDCl_3$ (Figure 2.2). We found two sets of proton signals arising from the central and end units which can thus be integrated to determine n_o: (i) The signal at δ2.54 ppm (triplet) arises from the innermost CH_2 protons of the tetradecyl side-chain bonded to the terminal thiophene rings, while that at δ2.78 ppm (unresolved multiplet) arises from the same protons bonded to the central thiophene rings. (ii) The signals at δ6.94 and δ6.86 ppm (singlets) arise from thiophene β-H of the terminal thiophene rings (denoted c in Figure 2.1), while that at δ7.04 ppm arises from the central thiophene rings appears (denoted b in Figure 2.1). The ratio of the integrated intensities of these central signals to the chain-end signals gives n_o. Accuracy of integration is typically better than 2%. No monomer signal was found in the polymer spectra (< 0.01 %; bithiophene monomer β-H expected at 6.77 ppm, and thienothiophene monomer β-H at 7.30 ppm). We found thus that n_o increases geometrically from 3 to 22 in accordance with theoretical prediction from the monomer feed ratio (Table 2.1), except for the highest MW sample which appears limited by solubility in chlorobenzene at the polymerization temperature. Therefore these oligomers and polymers are well-defined, and we denote them Pn_0 (n_o = 3–22). Although n_o is small, the repeat unit is large, and so the series here corresponds to relatively large π-electron systems (from 48 to 320 π-electrons). As a further demonstration, P3 shows a

π–π* transition gap that already approaches within 10 meV (in the solid state) of that of P22, and so all these materials have practically attained the electronic structure of the infinite-chain polymer. P22 is the highest MW barely soluble in hot chlorobenzene (and less so in hot chloroform!) and lies at the edge of the processability window in common solvents. rrP3HT of the same MW is far more soluble than PBTTT, probably because of the decrease in the alkyl side-chain density (1 alkyl chain per 6 π-electrons in PBTTT vs 1 per 4 π-electrons in rrP3HT) and the stiffening effects of the thienothiophene ring. The computed number-average contour length based on PM3 molecular modeling $L_{n,c}$ varies from 4 nm to 30 nm is shown in Table 2.1.

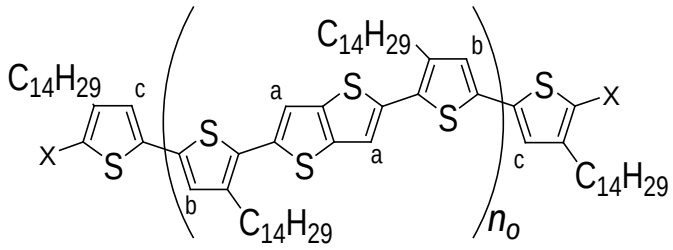

Figure 2.1 Chemical structure of poly(2,5-bis(3-tetradecylthiophen-2-yl)thieno[3,2-b]thiophene (PBTTT), a, b and c denote proton contribution from the biothiophene central unit, from the thiophene central unit and thiophene end unit.

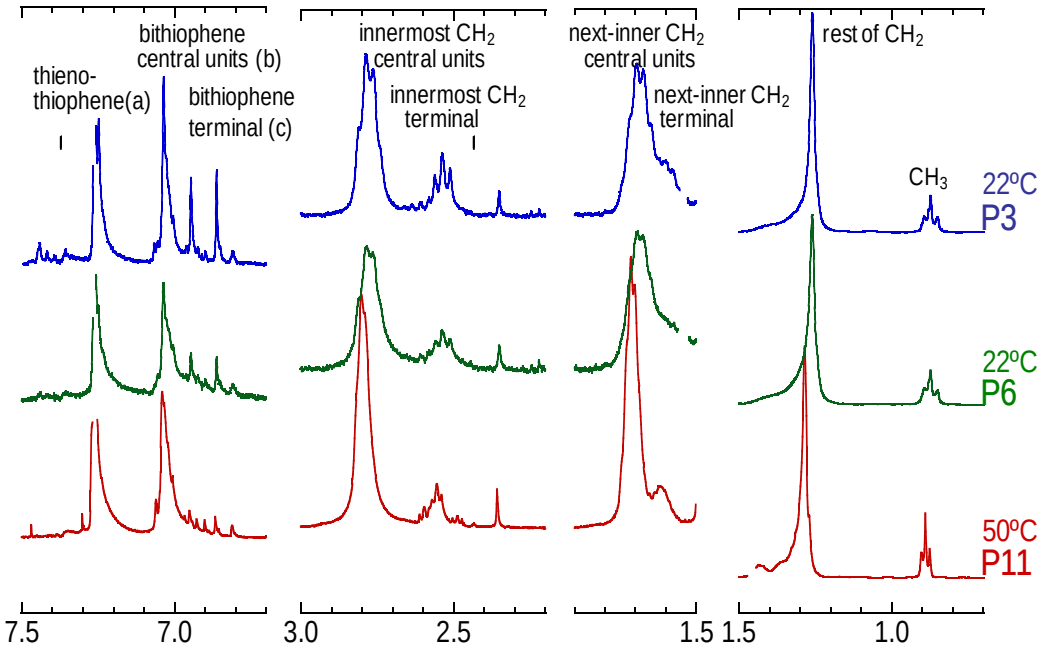

Figure 2.2 End-group analysis by ^{1}H NMR of P3 (in CDCl3, 22ºC) , P5 (in CDCl3, 22ºC) and P11 (in CDCl3, 50ºC).

	P22	P11	P6	P3
$n_{theo} = \frac{1}{1-r}$	>150	11	5.8	3.0
n_o	22	11±2	5.5±0.3	2.9±0.1
n_w	37	19±3	8.8±0.5	4.1±0.1
$M_{n,o}$	16k	8.2k	4.3k	2.6k
$L_{n,c}$ *(PBTTT)*= 13.8 Å *n_o	30 nm	15 nm	7.5 nm	4.0 nm
no of π electrons	320	160	86	48
M_n / $M_{n,o}$	2.18	2.31±0.14	2.28±0.04	2.5±0.02

Table 2.1 Parameters extracted from end-group analysis ^{1}H NMR

n_o is number average repeat unit determined by end-group analysis ^{1}H NMR; n_{theo} is the theoretical number average repeat unit where r is the feed ratio; $L_{n,c}$ is the computed number average contour length where 13.8Å is the length of PBTTT repeat unit; $M_{n,o}$ is the number average molecular weight given by [(n_o* molar mass of repeat unit) + molar mass of end unit)

2.3.2 Determination of chain conformational properties in dilute chlorobenzene

We then evaluated the conformation of these polymers through their Kuhn segment length ℓ_k and their Mark–Houwink–Sakurada exponent (a). To determine ℓ_k we employed the well-known "universal calibration" method of GPC. GPC was performed using differential refractometer (Waters 2414) detector, using a thermo-regulated column set (Jordi Gel DVB) with toluene as the eluent (flow rate, 0.35 mL min–1) and polystyrene MW standards from 2.6 k to 190 k.

GPC makes use of the property that the elution time of polymer chains depends solely on their hydrodynamic volume, which scales as $< s_g^2 >^{3/2}$, where $< s_g^2 >$ is the mean square radius of gyration of the chain.[14] $< s_g^2 >$ is related to ℓ_k according to:

$$< s_g^2 >= \frac{1}{6} n_k \ell_k^2 , \qquad \text{Eq (1)}$$

where n_k is the number of Kuhn segments; which in turn is related to the contour length:

$$L_{n,c} = n_k \ell_k . \qquad \text{Eq (2)}$$

Therefore the $< s_g^2 >$ values of these PBTTT polymers are given by those of the PS MW standards with the same elution time in hot toluene (75ºC) used as the eluant (Figure 2.3). The $< s_g^2 >$ values of PS in toluene as a function of MW have been determined previously by small-angle neutron scattering.[15] Then from Eqs (1) and (2), we can determine ℓ_k for PBTTT, and compare with PS (Table 2.2). We found there is a weak trend towards increasing ℓ_k with

chain length of PBTTT over the MW range studied, but a stronger one in PS. Neglecting this for now, the average ℓ_k is 9.0 nm for PBTTT and 2.8 nm for PS. Therefore, the persistence length of PBTTT chains given by $\frac{1}{2}\ell_k$ is about three repeat units long, and is longer than PS by a factor of *ca*. 3. As a consequence, the estimation of the MW of PBTTT using GPC with PS standards introduces a positive factor error $M_n / M_{n,o}$ of *ca*. 2–3, where M_n is the apparent number-average MW and $M_{n,o}$ is the true number-average MW (Table 2.1). This is likely to be the case for other related conjugated polymers also.

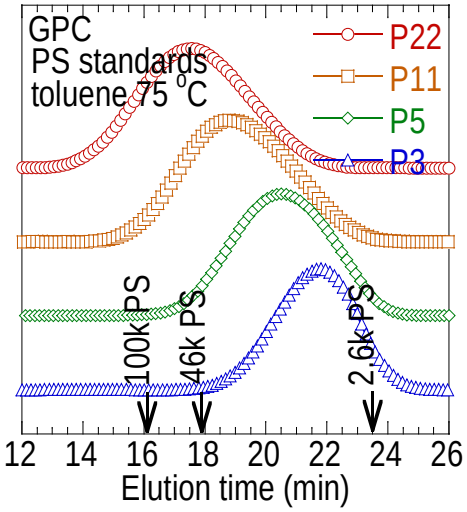

Figure 2.3 Gel permeation chromatography of PBTTT in hot toluene. Polystyrene standards MW marked on the plot to determine MW of PBTTT. All PBTTTs are narrowly dispersed.

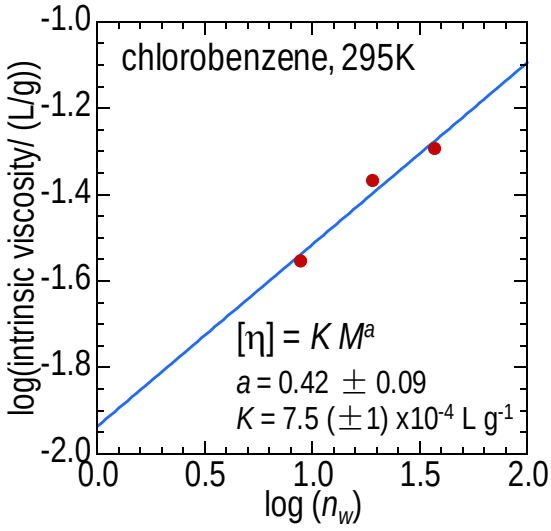

Figure 2.4 Intrinsic viscosity plots against number weight-average. The experiment data fits the Mark-Houwink equation nicely. Mark-Houwink slope of 042 ± 0.09 and K of 7.5 (±1) x10^{-4} Lg^{-1} were extracted

To determine the Mark-Houwink slope *a,* we obtained the intrinsic viscosity [η] of PBTTT–chlorobenzene solutions from the extrapolated zero-concentration limit of their specific viscosities,[16] i.e., $[\eta] = \lim_{c \to 0} \eta_{sp}$, where the specific viscosity $\eta_{sp} = \frac{\eta - \eta_{solv}}{c\eta_{solv}}$, where *c* is the polymer concentration, and also from the normalized relative viscosity, i.e., $[\eta] = \lim_{c \to 0} \frac{1}{c} \ln \frac{\eta}{\eta_{solv}}$. We plotted this as a function of the weight-average chain-length n_w in Figure 2.4. Using the Mark–Houwink–Sakurada equation $[\eta] = KM^a$, where *M* is viscosity-average *MW* but usually approximated by the weight-average *MW*, and we obtained the Mark–Houwink–Sakurada exponent *a* to be 0.42 ± 0.09 and intercept to be 7.5 (±1) x10^{-4} Lg^{-1}.

	P22	P11	P6	P3
Polydispersity, M_w / M_n	1.7	1.7	1.6	1.4
M_n	35k	19k	10k	6.6k
$L_{n,c}$ *(PS)* = 2.5 Å * n_o				
$\langle s^2 \rangle^{1/2}$	7.0 nm	4.8 nm	3.2 nm	2.4 nm
$\ell_{k,PBTTT}$	9.8 nm	9.2 nm	8.2 nm	8.6 nm
$\ell_{k,PS}$	3.4 nm	3.0 nm	2.5 nm	2.2 nm

Table 2.2 Useful parameters calculated and tabulated to obtain the Kuhn segment length

M_n is the number average molecular weight; M_w is the weight average molecular weight; n is the number average repeat unit; $\langle s^2 \rangle^{1/2}$ is the radius of gyration; $L_{n,c}$ is the computed number average contour length where 2.5Å is the length of PS repeat unit;

These two results clearly show that in dilute solution the PBTTT chain primarily adopts a random coil (rather than rigid rod, as might have be hypothesized), but its Kuhn segment length is enhanced by the stiffening effect of π-electron conjugation. Secondly, the usual working solvent for PBTTT, chlorobenzene, is in fact a slightly poorer solvent than the theta solvent at room temperature. These two characteristics lead to a coil-rod transition in solution that occurs at an unusually low polymer volume fraction, which is key to the formation of the extended-chain lamellar (para)crystals, as discussed next. For comparison *a* has been determined to be 0.58 ± 0.05 for rrP3HT in THF (which shows that THF is slightly better than a theta solvent), with ℓ_k of 4.8 nm.[17] Thus rrP3HT and PBTTT are both semi-flexible polymers in solution, but PBTTT is considerably stiffer than rrP3HT possibly as a result of a lower density of side chains, and the incorporation of the linear 2,5-thienothiophenediyl unit. Secondly, the

solvents have poorer solvating power for PBTTT. Whereas THF is a moderately good solvent for rrP3HT, it is distinctly a poor solvent for PBTTT; even chlorobenzene, which is a good solvent for rrP3HT, is a moderately poor solvent for PBTTT.

2.3.3 Coil→**rod transition** of PBTTT onset in the highly-dilute regime

We now show the existence of a coil→rod transition in PBTTT that occurs at an unusually low volume fraction Φ. This transition is related to those seen in rrP3ATs, poly(9,9-dialkylfluorene) and other π-conjugated polymers, when the solvent quality changes from good to poor,[18,19] or when the polymer passes from the solution to the solid state, or when it cools from the melt.[20-24] However such transitions have previously been observed at high Φ, where gelation and/or precipitation immediately follows.

In the highly dilute regime (i.e., $\Phi < s_g^2 >^{-3/2}$), the result is qualitatively different. Since the π-stacks first emerge in highly dilute solutions, the chains can aggregate in the extended state without passing into a neighboring π-stack. As the solution concentrates by evaporation, these π-stacks are deposited onto the substrate with some degree of orientational ordering of the π-stacks in the plane of the film. Subsequent annealing into the liquid crystal phase (LCP) where the chains have significant center-of-mass motion but still keep a rigid rod character, then allows the improvement in the perfection of order and growth of these nuclei into large monolayer lamellar paracrystals. The role of this transition in highly dilute solution in promoting the formation of the monolayer lamellae state has not previously been recognized. The two key aspects of this mechanism, π-stacking at high dilution and deposition of aligned π-stacks, will be established in this section and the next. If the transition occurs late in the semi-

concentrated state, as is the case for other π-conjugated polymer solutions, then chain entanglement becomes inevitable, and the fringed-micelle or folded-chain morphology predominates.

Figure 2.5(a) compares the solution state spectra of P3–22 at $\Phi = 1x10^{-5}$ (*ca*. 0.01 mg mL^{-1}), which is close to the "infinite"-dilution regime. The maximum in the absorption band decreases slightly from 2.7 eV in P3 to 2.6 eV in P22, and generally corresponds to the conformationally-disordered δ-state,[25] which is blue-shifted from the solid-state spectra. These spectra appear to be true equilibrium spectra as they are stable for days.[25] With increasing MW, a red-shifted tail emerges which at 2.1–2.2 eV which corresponds to the α, β and γ states identified in the solid-state spectra.[25] Therefore a population of planarized π-stacked aggregates co-exists with the conformationally disordered state in dilute chlorobenzene solution.

To probe its temperature dependence, we measured the solution-state spectra of P22 as a function of temperature in Figure 2.5(b). The concentration of red-shifted states clearly decreases strongly above 30 ºC, which suggests its formation is exothermic. Above 35 ºC the band shape (and band maximum) in fact approaches that of P3.

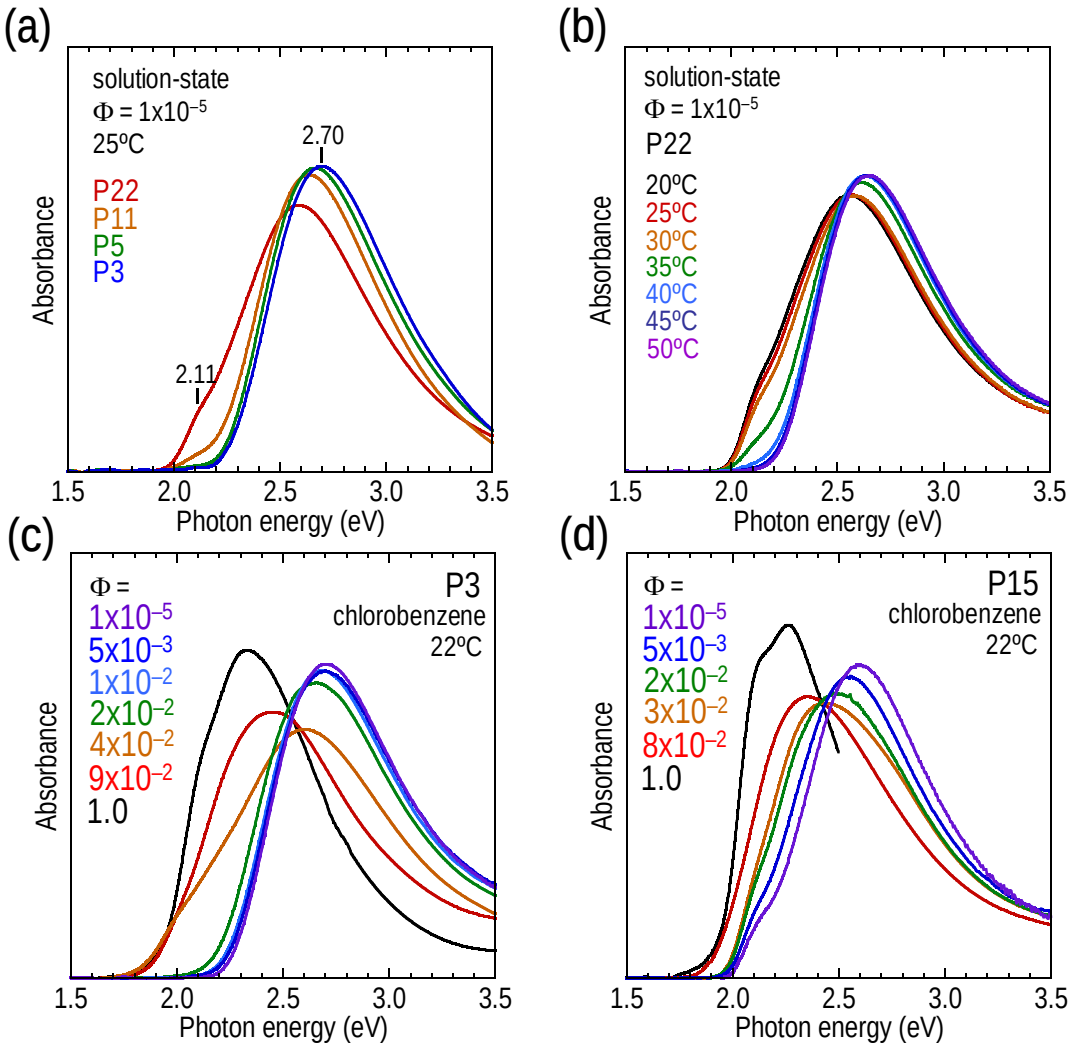

Figure 2.5 UV- visible absorption spectra of PBTTT solutions. (a) P3, P6, P11, P22 of volume fraction $1x10^{-5}$ in the "infinite" dilution regime. Progressive increase in the population of red-shift states (α,β and γ). (b) P22 of volume fraction $1x10^{-5}$ taken from 20ºC to 50ºC with 5ºC step increment (c) P3 taken at various volume fraction from $1x10^{-5}$ to $9x10^{-2}$ at 22ºC (d) P15 taken at various volume fraction from $1x10^{-5}$ to $9x10^{-2}$ at 22ºC

The question then arises whether these red-shifted states are formed by intrachain folding or interchain π-stacking. To address this, we measured the spectra as a function of Φ for P3 and P15 in Figure 2.5(c) and (d) respectively. In order to measure over a very wide volume fraction range from 1 x 10^{-5} to 9 x 10^{-2} (with the solid-state spectra representing Φ = 1.0), we used lithographically-patterned spacers to set the optical path-length between two fused silica plates from *ca*. 100 μm to 2 μm. The spectra clearly showed a strong systematic Φ dependence. The red-shift begins at *ca*. 1 x 10^{-2} for P3, but *ca*. 1 x 10^{-3} for P15. This suggests that interchain π-stacking rather than intrachain folding is the origin of the red-shifted state. A pseudo-isobestic point was observed at 2.4–2.5 eV, which suggests that the equilibrium predominantly involves two spectrally distinct states, the δ-state and the π-stacked aggregate.

This situation thus appears to be simple and the spectral transition can be quantitatively modeled to reveal the nature of the equilibrium. To do this, we first decomposed each solution-state spectrum $S(E)$ into the sum of a fixed infinite-dilution spectrum (at Φ = 1 x 10^{-5}) taken to be the random-coil spectrum $S_{coil}(E)$ and a slightly variable π-stacked aggregate spectrum $S_{agg}(E)$, i.e., $S(E) = \xi\, S_{coil}(E) + S_{agg}(E)$. At high Φ, the $S_{agg}(E)$ closely approaches the respective solid-state spectrum. The fraction ξ of $S_{coil}(E)$ thus directly gives the fraction of chains in the random coil conformation as a function of Φ for different n_o.

We can then select different ξ values (0.9, 0.7 and 0.5) and plot the corresponding Φ against n_o to give a phase diagram as shown in Figure 4a. The region in this Φ–n_o diagram with ξ > 0.9 (bottom left corner of diagram) corresponds to PBTTT chains existing predominantly in the random-coil state, while the region with ξ < 0.5 (top edge) corresponds to chains predominantly

in the π-stacked aggregated state. We found the following key features: (i) The transition width is broad: for example for n_o = 3, this spans two orders of magnitude with an onset Φ = 1 x 10^{-2} defined at ξ = 0.9. (ii) This onset clearly decreases with increasing n_o: for n_o = 15, aggregation begins even at Φ = 1 x 10^{-3}, which corresponds to 1 mg mL^{-1} solutions. At typical concentrations of 10–20 mg mL^{-1}, almost 30% of the chains reside in π-stacked clusters.

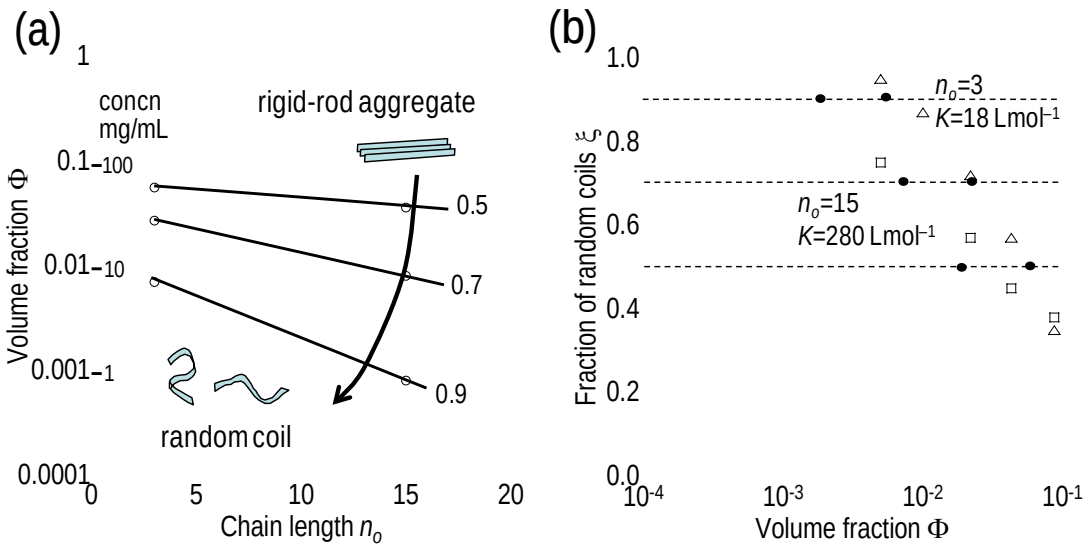

Figure 2.6 (a) Volume fraction of polymer (Φ) as a function of n_o showing fraction of chains in the random conformation(ξ) of 0.5, 0.7 and 0.9. ξ is obtained from quantitative modeling of each UV-vis solution-state spectrum S(E) at different concentrations into $S(E) = S_{coil}(E) + S_{agg}(E)$ where $S_{coil}(E)$ is the infinite dilution for each n_o. For typical solution concentration of 10–20 mg/mL, nearly half of the chains exist in π-stack clusters. (b) Dependence of ξ on volume fraction of polymer Φ. Solid triangle (▲) and square (■) are experiment data and solid line are fitted by solving applying mass balance equation together with stepwise association equilibrium model. $K=280 Lmol^{-1}$ fit P15 and $K=18 Lmol^{-1}$ fit P3 relatively well.

Then we quantitatively modeled this data to show that it can be described in first order by a simple stepwise association equilibrium model. This confirms that the primary event is that of a coil→rod transition with π-stacking to give simple aggregates that remain dispersed in solution. Our model comprises the following steps:

$P_1 + P_1 = P_2$ $\qquad K_2 = \dfrac{c_{P_2}}{{c_{P_1}}^2} \qquad \ln K_2 = -\dfrac{\Delta G_2}{RT} = -\dfrac{\Delta H_2}{RT} + \dfrac{\Delta S_2}{R}$

$P_1 + P_2 = P_3$ $\qquad K_3 = \dfrac{c_{P_3}}{c_{P_1} c_{P_2}} \qquad \ln K_3 = -\dfrac{\Delta G_3}{RT} = -\dfrac{\Delta H_3}{RT} + \dfrac{\Delta S_3}{R}$

…

$P_1 + P_{j-1} = P_j$ $\qquad K_j = \dfrac{c_{P_j}}{c_{P_1} c_{P_{j-1}}} \qquad \ln K_j = -\dfrac{\Delta G_j}{RT} = -\dfrac{\Delta H_j}{RT} + \dfrac{\Delta S_j}{R}$

where j is the cluster size of the π-stack (P_1 denotes the isolated chain). The usual thermodynamic quantities (ΔH_j, ΔS_j and ΔG_j) and stepwise formation constants (K_j) are written for molar concentrations c_j. Assuming that the stepwise association quantities are all identical, i.e., $\Delta H_2 = \Delta H_3 = \ldots = \Delta H_j = \Delta H$; and $\Delta S_2 = \Delta S_3 = \ldots = \Delta S_j = \Delta S$; and so $\Delta G_2 = \Delta G_3 = \ldots \Delta G_j = \Delta G$; and $K_2 = K_3 = \ldots = K_j = K$) since the change in enthalpy and entropy for each additional chain associated into the π-stack may not vary much, we can apply mass balance $n_{P,0} = \sum_{j=1}^{\infty} j c_{P_j}$ (i.e., total concentration of chains equals sum of the cluster size times cluster concentration) to get $n_{P,0} - \sum_{j=1}^{\infty} j K^{j-1} {c_{P_1}}^j = 0$. This equation can be solved to obtain ξ as a function of Φ for n_0 and a single variable K, which thus becomes the fitting parameter.

Two examples of these curves are plotted in Figure 2.6(b), for n_o = 15 and K = 280 L mol^{-1}; and n_o = 3 and K = 18 L mol^{-1}. The K values were chosen to give the best match to the experimental data (theory, curve; experimental data, symbols). We can see that this model reproduces the experimental data adequately, and so we can conclude that the spectral transition is indeed a coil→rod transition involving π-stacking (and planarization) of the PBTTT chains in simple clusters. From these K values, we can compute the stepwise Gibbs free energy ΔG to be –7.1 kJ mol^{-1} for n_o = 3, and –14 kJ mol^{-1} for n_o = 15.

2.3.4 Mechanism for formation of the extended-chain monolayer lamellae.

The P3 film shows a hay-stack ribbon morphology.[26] We measured 10^2 ribbons to obtain statistics on the width of these ribbons as shown in Figure 2.8(d). The ribbons are mostly 20–50-nm wide, which suggests several chains (5–10) aligned across its width, since L_{nc} = 4.0 nm. The thickness histogram of the ribbon shows peaks at 2.2 and 4.4 nm which corresponds to the thickness and twice the thickness of the PBTTT chain in the alkyl-chain direction (i.e., the crystallographic (100) direction).[1] The histogram is not sharp because the overlying ribbon may not rest conformally on the underlying one. Nevertheless it is clear that monolayer ribbons predominate, different from rrP3ATs in which the minimum whisker thickness is at least 2 or 3 times the (100) thickness, which was then taken as evidence of chain folding.[4,8] This also shows that the π-stacking direction also predominantly lies on the film plane. Several layers of ribbons can be seen with the lower layers coalesced with adjacent ribbons, which suggests that the nano-ribbon morphology persists deep into the sub-surface. Before annealing, the film has a mixed modular and rod morphology 20–40-nm across, and also 2–4 nm high.

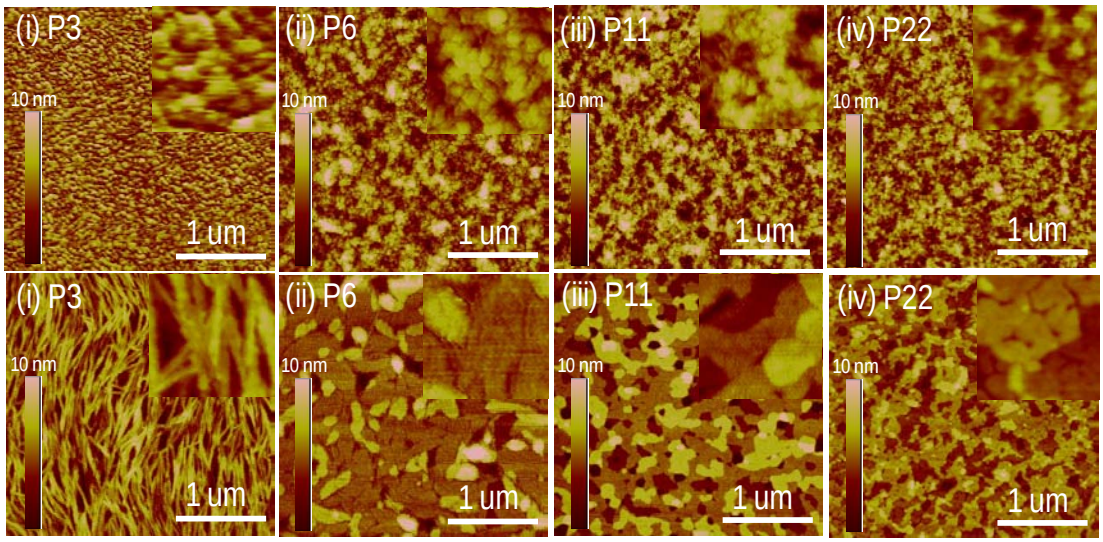

Figure 2.7 3 x 3 μm atomic force microscopy (AFM) of 30-nm-thick PBTTT film on HMDS-treated silicon oxide substrate spin-coated from 10 mg/ml PBTTT in chlorobenzene after cooled down from 85°C for 30min. (top) P3, P6, P11, P22 pristine films. (bottom) after annealed into individual liquid crystalline phase for 10 min and quenched cool. (Inset) zoom-in of 500nm x 500nm areas.

In contrast, the annealed P6 film shows a platelet morphology with more nearly similar lengths (within a factor of 2–3) of its major and minor axes. The exposed diameter is typically 80–250 nm (Figure 2.8(c)), which is many times of the $L_{n,c}$ of 7.5 nm, while the height is very narrowly distributed at the expected (100) thickness of 2.0–2.2 nm (Figure 2.9 (a)). These platelets are coalesced in the lower layers to give a continuous film. The as-spincast film has a worm-like morphology comprising straight, bent, and U-shaped structures that are 20–40-nm across and 2-nm high, and therefore are of similar size scale as P3.

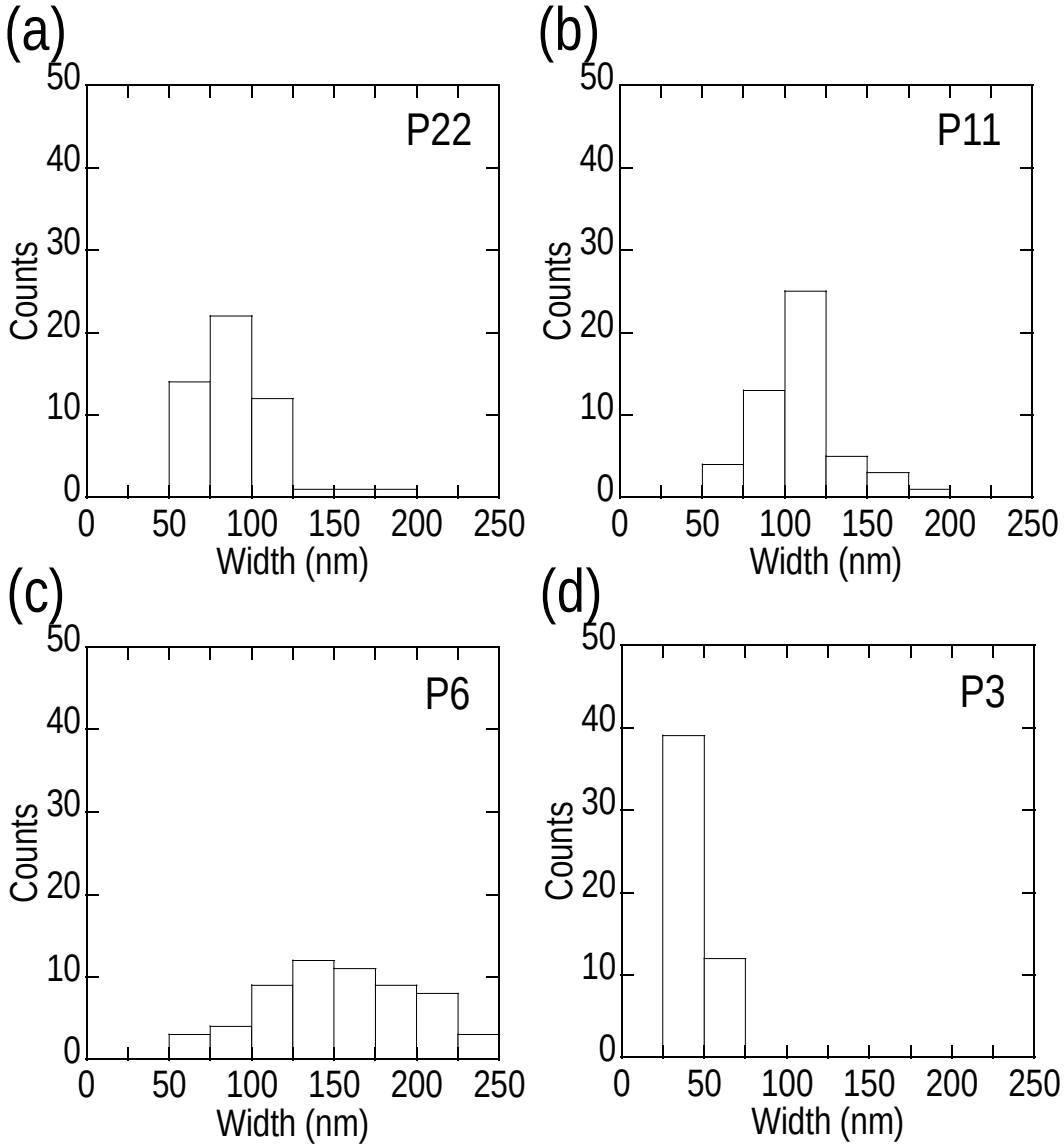

Figure 2.8 Histogram of the width of the ribbons in PBTTT films. About 50 data points are taken for each set. (a) P22 has typical width mostly between 50-125 nm. (b) P11 between 75-125 nm. (c) P6 has broader width range from 50-250 nm, contributed by the coalescen of underlying ribbons (d) P3 has narrow-dispersed width between 25-75 nm.

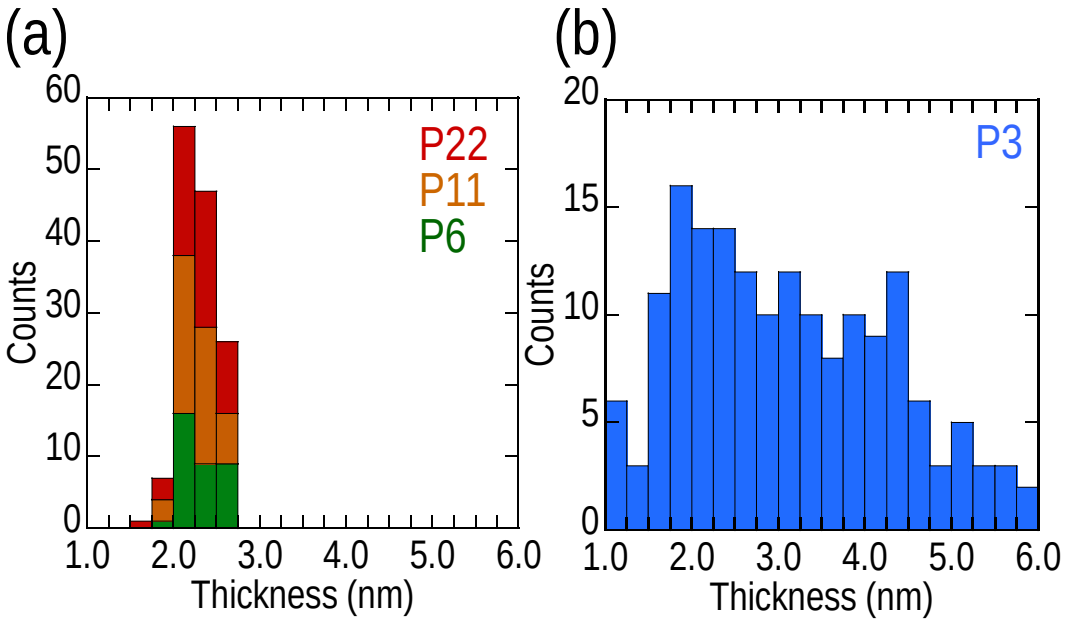

Figure 2.9 Histogram of the thickness of the ribbons in PBTTT films. About 50 data points are taken for each set. (a) P6, P11 and P22 have typically molecular thickness of 2.2 nm. (b) P3 showing molecular thickness of 2.2 nm and multiples stacks.

As n_o increases to P11, the annealed film now shows the characteristic terrace morphology with increasing degree of coalescence in the underlayers that is widely reported for PBTTT. The nominal width of these terraces is 75–150 nm (Figure 2.8(b)), while the thickness remains narrowly distributed at 2.0–2.2 nm (Figure 2.9 (b)). Before annealing, the morphology is again worm-like at the 20–40-nm length scale. Finally the annealed P22 film also exhibits terrace morphology with a nominal width that is slightly smaller (50–125 nm, (Figure 2.8 (a)) which is still 2–4 times of the $L_{n,c}$ of 30 nm, with the same monolayer thickness (2.0–2.2 nm, Figure 2.9 (a)). The narrowest width observed here is thus still compatible with fully extended chains. Before annealing, the morphology is a mixture of worm-like and nodular structures at a similar length scale as P6.

In summary, detailed quantitative analyses of the dependence of the AFM morphology on n_o reveals the following characteristics. The exposed top-surface morphology of the as-spincast films is independent of n_o. It is characterized in all cases by very fine features (nodules and worm-like structures) on a lateral length scale of 20–40-nm with a height of 2 nm that corresponds to the deposited π-stacks. These dimensions indicate that the π-stacked aggregates are deposited generally lying down parallel to the film plane, although there is still a considerable amount of disorder at this stage. This is a crucial step in our proposed mechanism that is separately confirmed by variable-angle spectroscopic ellipsometry (vide infra). The pre-orientation makes it possible for the π-stacks to subsequently grow in large monolayer lamellae upon annealing into the LCP. The thickness of these aggregates corresponds primarily to a monolayer and so the chains are not back folded in the (100) direction, while the width of these aggregates appears to span several chains for small n_o, but a single chain for P22.

Annealing into the LCP allows the π-stacks to grow in size and attain better perfection. There is however a strong n_o dependence in this process. The systematic evolution: nano-ribbon → platelet → large terrace → fine terrace, with n_o demonstrates the importance of chain diffusion in determining the extent of growth in the lateral π-stack direction. The transition from ribbon to terraces has previously been noted but briefly.[26] Initially for small n_o, the polymer chain diffusivity is large which appears to favor the growth of long π-stacks to give nano-ribbons. Then as n_o increases, the lateral extension of the π-stacks becomes favored to give more equi-axed domains. Finally, as n_o becomes large, both these processes become limited and the terrace structure becomes finer. Therefore the final film morphology is largely controlled by n_o, = undoubtedly through the kinetics of nucleation and growth. In all cases, the lamellae

thickness corresponds to the (100) thickness, and so the PBTTT chains are packed edge-on for all MWs here.

The mechanism is based on formation of extended-chain π-stacked 2-D aggregates in highly dilute solutions, which are deposited onto the substrate, as schematically illustrated in Figure 2.10. There are three key stages: (1) In the first stage, as the solution evaporates and concentrates, the fraction of PBTTT chains aggregating into 2-D π-stacks increases with the attendant coil→rod transition of the individual chains. For PBTTT in chlorobenzene, the transition begins in the dilute regime where inter-stack interaction does not occur, and so the chains can adopt fully extended conformation without entanglement in each π-stack. This is driven by having the appropriate borderline poor solvent that provides sufficient driving force for early π-stacking. (2) In the second stage, towards the final drying state, these 2-D π-stacked aggregates grow and are deposited with their π-stacking direction predominantly parallel to the film plane, perhaps are a result of the shear flow during spin-casting. At this stage, there is considerable disorder within and between the π-stack aggregates that are in the sub-100-nm size scale, but unimolecular thick. (3) In the third and final stage, when the film is annealed into the nematic LCP, the lamellae structure is melted, but the orientation and anisotropy of the domains remain. When subsequently cooled, this allows the nascent oriented π-stacked nuclei to grow laterally and to develop registration between neighboring lamellae to give a 3-D lattice. This contrary to speculation in the literature does not require the side-chains to crystallize and interdigitate to provide the "locking". In fact, it is known from detailed variable-temperature FTIR spectroscopy that the side-chains are increasingly disordered above 220 K. The situation is therefore similar to rrP3HT for which a 3-D lattice is obtained also without side-chain crystallization. The resultant film morphology is MW-dependent probably as a result of the dependence of crystallization and growth kinetics on MW. The exposed surface reveals a

ribbon or platelet or terrace morphology depending on MW, but with unimolecular step height as previously well known already.

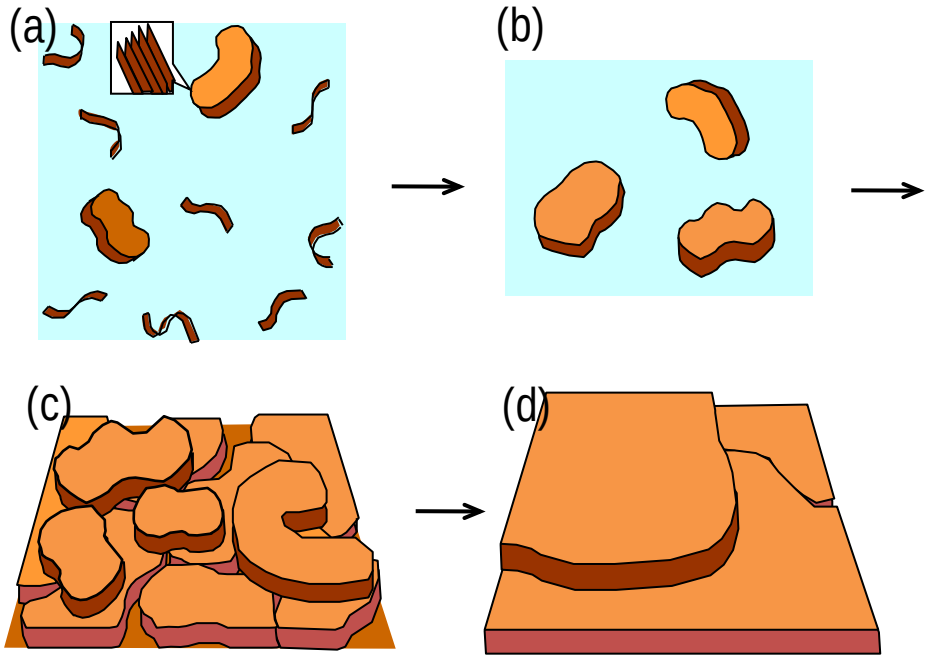

Figure 2.10 The formation of extended-chain π-stacked 2-D lamellae onto the substrate. (a) in diluted solution, the majority of the polymer chains extend while some inter-stack interaction starts to take place. (b) 2-D π-stacked aggregates grow as concentration gets higher. (c) These aggregates are deposite onto the substrates with π-stacking dierection parallel to the film plane. (d) after annealing above LCP to nematic phase and cooling down to room temperature, big lamellae with neighboring registration are formed.

The evidence comes from: (i) Mark–Houwink–Sakurada exponent, which reveals that PBTTT behaves as flexible coils and chlorobenzene as a sub-theta solvent, (ii) concentration-dependent and temperature-dependent solution-state UV-vis spectra which show a well-behaved coil–rod equilibrium characteristic of π-stacking with dependence on MW, (iii) AFM of the as-spincast film which show evidence of π-stacked aggregates typically 20–40-nm in lateral size, but monolayer thick, (iv) AFM of the annealed film which show the facile growth of the lamellae on the exposed surface but with monolayer step heights. (v) UV-Vis spectroscopy which shows that the films have remarkably similar absorption coefficients as-spincast and after annealing, and hence the deposited film already has the π-stacks oriented predominantly in the plane of the film.

2.3.5 Generality of mechanism: monolayer-terraced morphology in rrP3HT films

Finally, to illustrate that this mechanism is general, we sought to create the monolayer π-stacked morphology in rrP3HT films. rrP3HT has been well known to give whisker or nodular morphology but not monolayer terraces. Although rrP3HT is more flexible than PBTTT, which may suppress stage (i) of the mechanism, we overcome this by selecting a sufficiently poor solvent. We first confirmed that rrP3HT too has a liquid crystalline phase between 440–500 K by a combination of variable-temperature XRD and POM.[24] Then rrP3HT is dissolved into a mixture of chlorobenzene: mesitylene (1:9 by vol). The large mesitylene volume fraction turns the mixture into a borderline poor solvent. A 15-nm film is then spin-cast onto Si wafer, annealed at 465 K for 10 min and cooled at a rate of 10 ºC/min.

Figure 2.11 (a) shows the AFM image of the as-spincast rrP3HT film. It exhibits molecular terraces (typically 20–40-nm wide, 1.6-nm high) that are characteristic of monolayer π-stacked lamellae that have not been observed previously in this material, in addition to the whisker morphology. The usual nodular morphology for this material was not observed. Upon annealing the terrace morphology becomes more pronounced (

Figure 2.11 (b)), with a height distribution clustered at 1.5–1.75 nm, 3.0–3.25 nm and 4.75–5.0 nm (Figure 2.12) corresponding to the expected thickness of the lamellae in the (100) direction (1.6 nm), and its multiples.

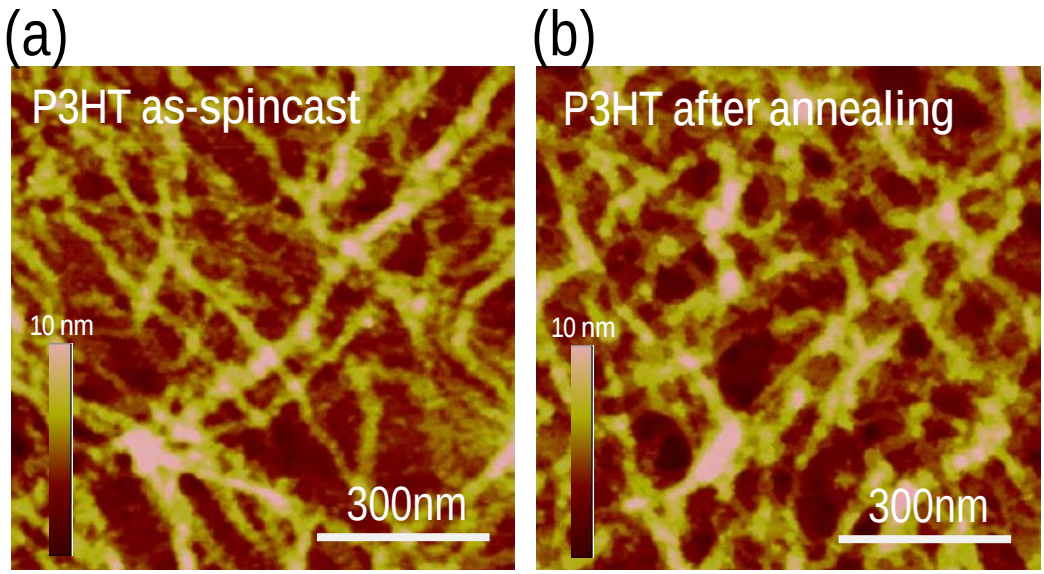

Figure 2.11 1x1 μm AFM images of rrP3HT films. (a) pristine rrP3HT film spin-coated from chlorobenzene:mesitylene (1:9) showing whisker ribbons, when annealed into LCP for 10 min and cool-down from hot plate to 50ºC at 10 ºC /min (b) shows molecular terrace. Z-scale is 10 nm.

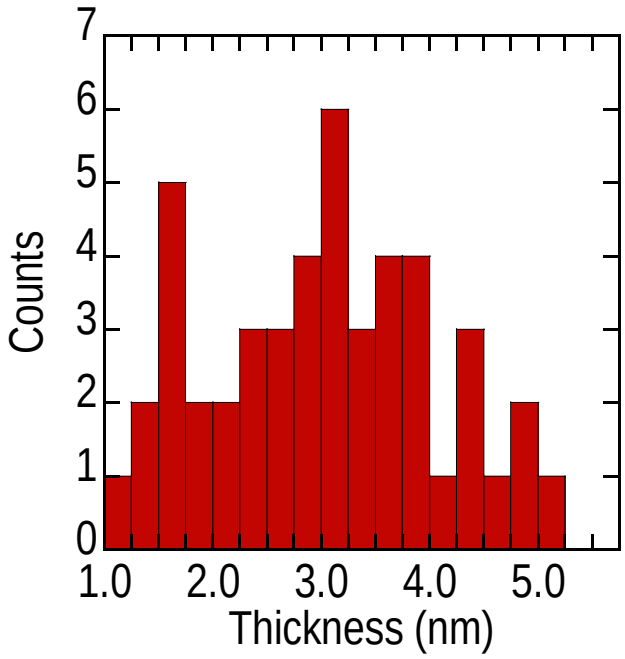

Figure 2.12 Histogram of the thickness of the rrP3HT whisker. About 50 data points are collected. Molecular thickness of 1.6 nm and also multiples molecular stacks are observed.

2.4 Summary

In summary, we have described a new model that explains the formation of the extended-chain lamellae morphology in π-conjugated polymers with a propensity to π-stack. It involves the pre-ordering of the conjugated polymer into 2-D π-stacked monolayer aggregates in dilute solution using a borderline poor solvent. Deposition of these by spin-casting then gives the monolayer π-stacks pre-disposed to in-plane alignment. A subsequent anneal into the nematic phase followed by cooling recrystallization then promotes the formation of well-ordered lamellae. We have demonstrated that this occurs in PBTTT from chlorobenzene solutions, and also in rrP3HT from a mixed chlorobenzene–mesitylene solution. The results appear to be general, and so points to a new processing "design" rule to make highly-ordered films for optoelectronic applications.

2.5 References

1 McCulloch, I. et al. Liquid-crystalline semiconducting polymers with high charge-carrier mobility. Nature Mater. 5, 328-333 (2006).

2 Zhang, R. et al. Nanostructure dependence of field-effect mobility in regioregular poly(3-hexylthiophene) think film field effect transistors. J. Am. Chem. Soc. 128, 3480-3481 (2006).

3 Kline, R. J. et al. Dependence of regioregular poly(3-hexythiophene) film morphology and field-effect mobility on molecular weight. Macromolecules 38, 3312-3319 (2005).

4 Ihn, K. J., Moulton, J. & Smith, P. Whiskers of poly(3-alkylthiophene)s. J. Polym. Sci. Part B: Polym. Phys. 31, 735-742 (1993).

5 Zen, A. et al. Effect of molecular weight and annealing of poly(3-hexylthiophene)s on the performance of organic field-effect transistors. Adv. Funct. Mater. 14, 757-764 (2004).

6 Kline, R. J., McGehee, M. D., Kadnikova, E. N., Liu, J. & Fréchet, J. M. J. Controlling the field-effect mobility of regioregular polythiophene by changing the molecular weight. Adv. Mater. 15, 1519-1522 (2003).

7 Chang, J. F. et al. Enhanced mobility of poly(3-hexylthiophene) transistors by spin-casting from high-boiling-point solvents. Chem. Mater. 16, 4772-4776 (2004).

8 Chang, J. F. et al. Molecular-weight dependence of interchain polaron delocalisation and exciton bandwidth in high-mobility conjugated polymers. Phys. Rev. B 74, 115311-115312 (2006).

9 Liu, J., Arif, M., J., Z., Khondaker, S. I. & Zhai, L. Controlling poly(3-hexylthiophene) crystal demension: nanowhiskers and nanoribbons. Macromolecules 42, 9390-9393 (2009).

10 Kim, D. H., Park, Y. D., Jang, Y., Kim, S. & Cho, K. Solvent vapor-induced nanowire formation in poly(3-hexylthiophene) thin films. Macromol. Rapid Commun. 26 (2005).

11 Samitsu, S., Shimomura, T., Heike, S., Hashizume, T. & Ito, K. Effective production of poly(3-akylthiophene) nanofibers by means of whisker method using anisole solvent: structural, optical, and electrical properties. Macromolecules 41, 8000-8010
(2008).

12 Malik, S. & Nandi, A. K. Crystallization mechanism of regioregular poly(3-alkyl thiophene)s. J. Polym. Sci. B, Polym. Phys. 40, 2073-2085 (2002).

13 Hugger, S., Thomann, R., Heinzel, T. & Thurn-Albrecht, T. Semicrystalline morphology in thin films of poly(3-hexylthiophene). Colloid Polym. Sci. 2004, 932-938 (2004).

14 Mena-Osteritz, E. et al. Two-dimensional crystals of poly(3-alkylthiophene)s: direct visualisation of polymer folds in submolecular resolution. Angew. Chem. Int. Ed. 39, 2680-2684 (2000).

15 Gedde, U. W. Polymer physics. (Chapman & Hall, 1995).

16 Huber, K., Bantle, S., Lutz, P. & Burchard, W. Hydrodynamic and thermodynamic behavior of short-chain polystyrene in toluene and cyclohexane at 34.5ºC. Macromolecules 18, 1461-1467 (1985).

17 Sperling, L. H. Introduction to physical polymer science. Third edn, (Wiley-interscience, 2001).

18 Heffner, G. W. & Pearson, D. S. Molecular characterisation of poly(3-hexylthiophene). Macromolecules 24, 6295-6299 (1991).

19 Rughooputh, S. D. D. V., Hotta, S., Heeger, A. J. & Wudl, F. Chromism of soluble polythienylenes. J. Polym. Sci. B, Polym. Phys. 25, 1071-1078 (1987).

20 Inganäs, O., Salaneck, W. R., Österholm, J. E. & Laakso, J. Thermochromism and solvatochromism effects in poly(3-hexylthiophene). Synth. Met. 22, 395-406 (1988).

21 Yoshino, K., Nakajima, S., Park, D. H. & Sugimoto, R. Thermochromism, photochromism and anamolous temperature dependence of luminescence in poly(3-alkylthiophene) film. Jap. J. Appl. Phys. 27, L716-718 (1988).

22 Inganäs, O., Gustafsson, G., Salaneck, W. R., Österholm, J. E. & Laakso, J. Thermochroism in thin films of poly(3-alkylthiophenes). Synth. Met. 28, C377-384 (1989).

23 Tashiro, K. et al. Structure and thermochromic solid-state phase transition of poly(3-alkylthiophene). J. Polym. Sci. B, Polym. Phys. 29, 1223-1233 (1991).

24 Zerbi, G., Chierichetti, B. & Inganäs, O. Thermochromism in polyalkylthiophenes: molecular aspects from vibrational spectroscopy. J. Chem. Phys. 94, 4646-4658 (1991).

25 Tashiro, K. et al. Structure and thermochromic solid-state phase transition of poly(3-alkylthiophene): III. Effects of alkyl side chain length on the phase transitional behavior. Synth. Met. 55-57, 321-328 (1993).

26 Wang, S. et al. Solvent effects and multiple aggregate states in high-mobility organic field-effect transistors based on poly(bithiophene-alt-thienothiophene). Appl. Phys. Lett. 93, 162101-162103 (2008).

27 McCulloch, I. et al. Semiconducting thienothiophene copolymers: design, sythesis, morphology, and performance in thin-film organic transistors. Adv. Mater. 21, 1091-1109 (2009).

Chapter 3. The nature of the liquid crystalline and isotropic transitions in PBTTT and their dependence on molecular weight

In this chapter, we systematically studied the temperature dependence of the birefringence using polarizing optical microscopy, and crystal lattice using wide-angle X-ray scattering in a particularly important tetradecyl sidechain-substituted PBTTT as a function of molecular weight. We found that the lamellar paracrystals exhibit well-defined (*h*00) reflections in the lamellar stacking direction and a (010) reflection in the π-stacking direction, but their intensities have different temperature dependences. In particular, we showed from the systematic dependence on degree of polymerisation n_o, that the thermal transitions comprise a pair of closely-spaced T_k' and T_k'' transitions to the ordered nematic and the nematic liquid-crystal phase respectively, followed by the isotropic melting (T_i).

3.1 Introduction

The dependence of the properties of rrP3HT on the MW has been extensively studied, including field-effect mobility and morphology. Low MW rrP3HT is known to give whisker rods where π-stacking direction is the whisker long axis.[5] High MW rrrP3HT usually give nodular morphology, [6] although recently studies showed that whisker rod are also possible for high MW by slow evaporation using high boiling point solvent. [8]

For PBTTT, several detailed characterization studies in particular by X-ray diffraction have been reported recently. In the literature so far only the MW dependence of film morphology has been reported.[26] Simple assignments of phase transitions are suggested based on previous common named transition such as side-chain and main-chain melting. Therefore, several essential aspects, such as thermal transitions, nature of the liquid crystallinity order, and charge-transport characteristics, have to be better understood. However, no detail works are reported so far. Even the phase transitions of the earlier results also appear to be incomplete. Previously it was widely accepted that the high field-effect mobility arose from 3-D crystallization with interdigitation of primarily all-trans side-chains. We will show that this is not suppoted in the next chapter by detailed variable temperature vibrational and electronic spectroscopies taken over a far wider range of temperature.

Furthermore while extensive sets of XRD have been reported to investigate the orientation within thin films of this material, “powder” diffraction of the bulk state, and in particular its temperature dependence have not been published. The understanding therefore of what has imparted these comparably complicated set of thermal transitions and the dependence on MW

in this apparently most-ordered polymer known to date is central to the development of materials.

3.2 Experimental methods

3.2.1 Differential scanning calorimetry (DSC)

DSC was measured on TA Instruments 2920 Differential Scanning Calorimeter. PBTTT films were prepared on an aluminum pan at 85°C by drying from 10mg/mL chlorobenzene solutions in a nitrogen glovebox. The films were annealed at 150°C for 10 min and cooled down together with the hotplate in glovebox. The aluminum pan was closed by crimping with its cover and loaded into the calorimeter. The DSC data was obtained by making two complete heating and cooling cycles –50°C → 250°C → –50°C at a rate of 10°C min^{-1} in flowing nitrogen. The calorimeter was calibrated with indium.

3.2.2 Variable temperature polarised optical microscopy (POM)

Approximately 20-μm-thick films of PBTTT with various MWs were drop-cast from chlorobenzene solutions onto glass slides in the nitrogen glovebox, and encapsulated with glass cover slips using Parafilm M perimeter spacers. The sample was then mounted on a Linkam hotstage and heated at an average rate of 10ºC min^{-1} in a polarising optical microscope under crossed polarizer condition. The samples were illuminated in transmission with 656-nm light obtained through a narrow bandpass interference filter to avoid fluorescence (and the attendant depolarization), and their transmission images samples recorded as a function of temperature.

3.2.3 Wide-angle X-ray scattering (WAXS).

Approximately 100-μm-thick PBTTT films were deposited onto the Al_2O_3 "powder" sample holders at 110°C (isothermal well temperature) by drying 50 mg mL^{-1} solutions in chlorobenzene directly into the sample holders in a nitrogen glovebox. The films were then annealed at 160°C for 15 min and cooled slowly together with the hotplate in the glovebox. This procedure removed the solvent and recrystallized the films. The sample holders were then mounted inside an Anton Paar HTK 1200 high-temperature vacuum chamber (< 1x 10^{-2} mbar) of a Bruker-AXS D8 powder X-ray diffractometer. θ–2θ diffraction scans were recorded between 3.00º to 30.00º in steps of 0.05º (1 s $step^{-1}$), using monochromatized 1.541-Å Cu K_α radiation (30 mA and 40 kV). The films were heated to the selected temperature and stabilized for 10 min before collecting data. Two diffractograms were collected at each temperature to check for equilibrium and absence of degradation, and then averaged. Because the (para)crystalline domains in such thick films are practically isotropically oriented, the WAXS diffractograms can be interpreted using "powder" diffraction techniques. A substrate Bragg reflection from the Al_2O_3 sample holder visible in all the diffractograms was used to check for 2θ accuracy (at room temperature, 26.60º, lit. 26.60º) and instrumental width (fwhm, 0.16º).

The XRD patterns were deconvoluted to separate the crystalline and amorphous components using a sum of Gaussians to represent the amorphous scattering.

3.3 Results and discussions

3.3.1 Indication of a rich thermal transition behavior by DSC

The first- and second-cycle DSC thermograms of Pn for different *n* values are shown in Figure 3.1 (a) - (d). In general, three sets of endothermic transitions on heating can be discerned between –50ºC and 250ºC. The lowest transition at 50ºC has been marked the ring-twist transition T_r, following the conclusions of a detailed study, which is going to be discussed in the next chapter. The highest transition (varying between 140 to 240 ºC from P3 to P22) has been assigned the isotropic melting transition T_i, based on the results of this chapter. A weak endotherm is often discernible in the first cycle, together with the weak exotherm of the cooling crystallization downshifted by 20–30ºC due to supercooling. This transition is strongly dependent on MW as expected in general of melting transitions. Because of the small heat flow, this transition is marked based on POM observations described in the next part.

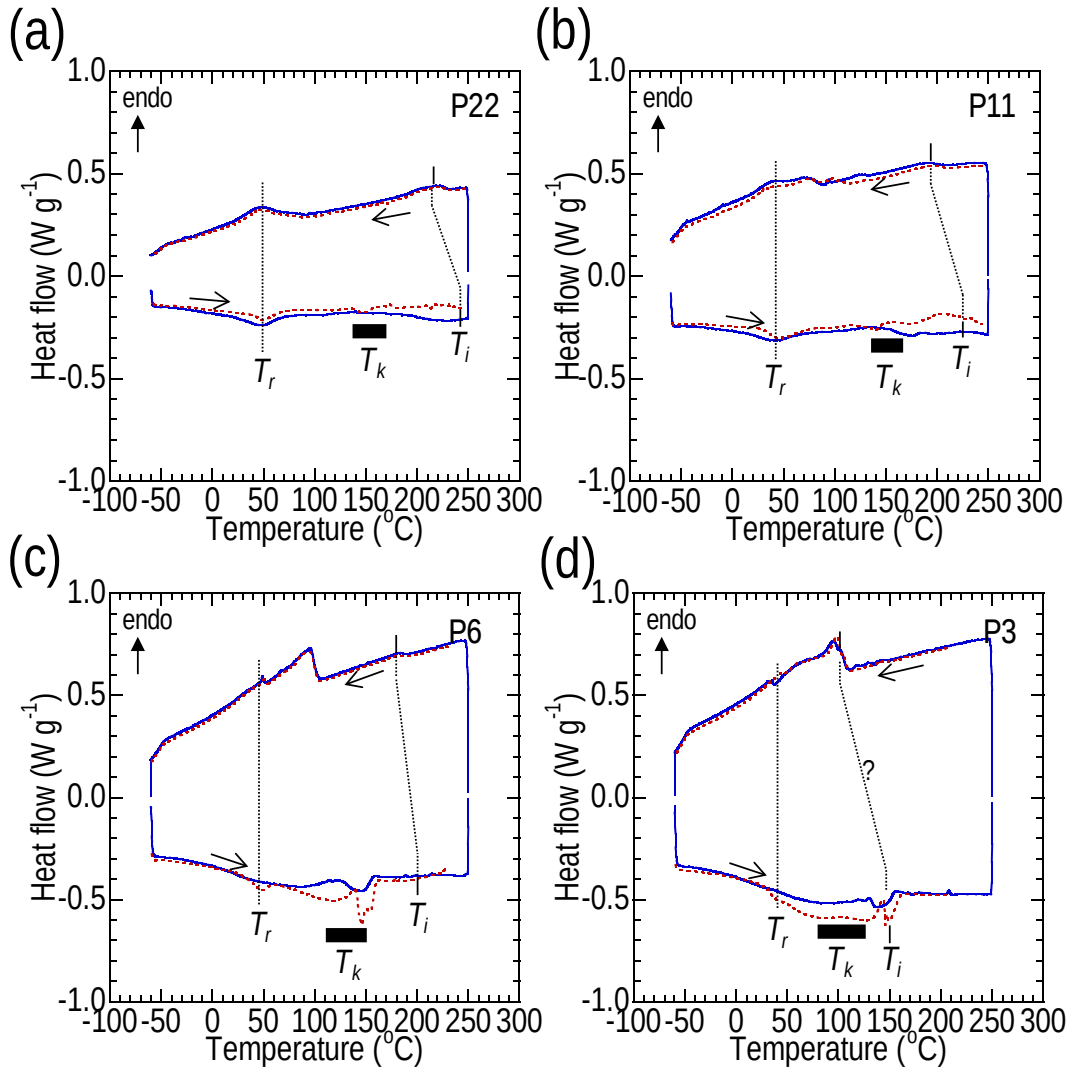

Figure 3.1 DSC thermograms of PBTTT films recrystallized by annealing to 150ºC (10 min) followed by slow cooling in the Al pans. (a) P22 (b) P11 (c) P6 (d) P3. First heating/ cooling cycle (dotted red lines); second cycle (blue solid lines) under nitrogen at a heating rate of 10 °C /min. Direction of scan is indicated. Ring-twist transition Tr, melting transition to liquid-crystal Tk (comprising a pair of transitions for the lower-MW materials) and melting transition to isotropic phase Ti are marked on the plot. The nature and location of T_k and T_i transitions are separately determined by POM and variable-temperature XRD.

In between T_r and T_i lies an apparently complex but weak set of thermal transitions. Previously, the dominant transition here was assigned to side-chain melting from their apparent

dependence on side-chain length.[1,26,27] However the POM and WAXS data show that the phase transitions in this region in fact arise from melting of the paracrystal to lower-order liquid crystalline structures that is characterized by separate or congruent melting of the π-stacks and the lamellar stacks. In particular the liquid crystalline phase between T_i and T_k' has been confirmed by birefringence under crossed polarizers. The small transition enthalpies, similar to other liquid crystalline polymers,[28,29] make it difficult to unambiguously locate these transitions in the DSC thermograms. For example, the enthalpy of the 150ºC transition in P6 is only 10–15 J g^{-1} (cf. enthalpy of fusion of perfectly crystalline polyethylene of 295 J g^{-1}; and polypropylene 205 J g^{-1}). In the figure, we have therefore marked a range of temperatures where we expect them based on the POM and WAXS data demonstrated in the next parts.

3.3.2 Confirmation of the location of the T_i transition by variable temperature POM

To determine T_i, the formation of the isotropic state was observed under crossed polarizers in POM. The drying of the solution droplet under quiescent conditions leads to radial movement of the drying front, and hence radial film deposition. This leads to a centrosymmetrically-oriented deposition of the polymer chains that are most likely tangentially aligned to the circular film, with radial growth of the π-stacks. Under crossed polarizers, a single centrosymmetric Maltese cross pattern spans the entire film. [Similar patterns are found also in drop-cast films of other semicrystalline conjugated polymers such as poly(9,9-alkylfluorene), but not in amorphous polymers.]

A sub-set of the crossed-polarized images collected at the center of the P11 film as a function of temperature are shown as illustration in Figure 3.2. At room temperature, the Maltese cross

pattern confirms that the initial film is birefringent as is expected of the centrosymmetric deposition of anisotropic semicrystalline polymers. The pattern also shows slip–stick marks characteristic of the receding solution from the film surface. As temperature increases, the images initially brighten (up to 190ºC) then darken and finally become completely black (240ºC). The temperature at which the film appears fully black marks the temperature (T_i) for complete melting into the isotropic phase. Reversing the temperature cycle shows that the birefringence reappears at 200ºC after a super-cooling of 30ºC. However, the cross-polarizer texture is now granular and the initial macroscopic orientation is thus lost, as expected of recrystallization of a melt. The images then further dim as temperature reduces to room temperature. The reversal of the sequence of POM images in the cooling half-cycle shows that no degradation of the polymer film occurred.

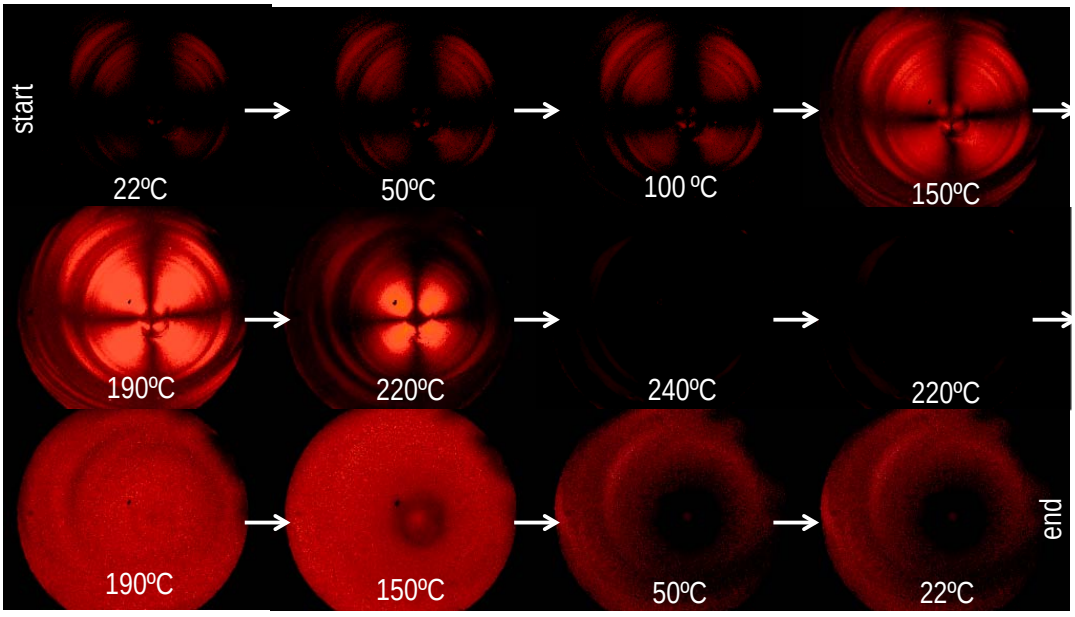

Figure 3.2 Variable temperature polarizing optical microscopy of P11 film. Images are taken at every 10K after equilibrated at each temperature for 1min but only select images are shown. The intensity diminishes at about 240ºC indicating isotropic melting point has reached.

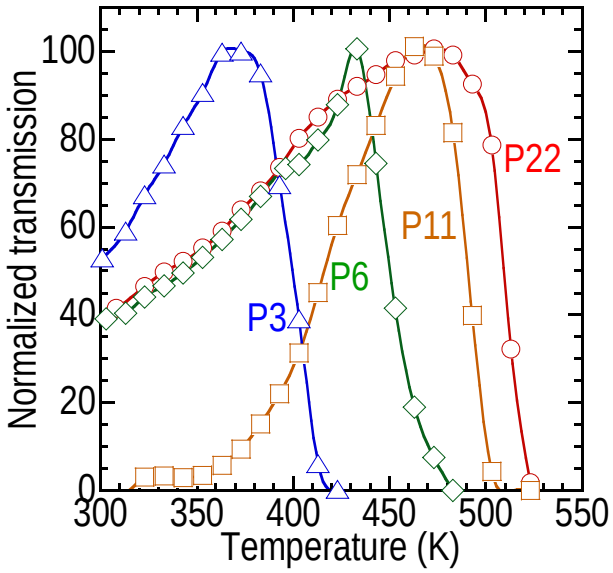

Figure 3.3 Temperature dependence of the intensity of the optical POM images for all PBTTT films. Isotropic melting point is taken from near diminishing intensity of the images. P22 is at 525K, P11 at 505K, P6 at 470K and P3 at 415K.

To more precisely locate T_i, the intensity of the images was quantified as shown in Figure 3.3 for different n in the heating half-cycle. All the Pn polymers show the same behavior of gradual intensity peaking, followed by sharp fall and complete extinction, but at different temperatures. The transition width (between 10% and 90%) was typically 20ºC under our experimental conditions. We defined T_i to be the temperature where 25% intensity remains. From the data, this clearly increases with n.

3.3.3 Resolving the T_k' and T_k'' transitions by WAXS

Figure 3.4(a)–(d) show the XRD for different n_o as a function of temperature. The recrystallization ensured (quasi-)thermodynamic were studied rather than kinetic relaxation effects. The films were thick enough (*ca*. 100 μm) that the orientation ordering at interfaces contributed negligibly to the diffractogram. Hence, these are in essence "powder" diffraction patterns.

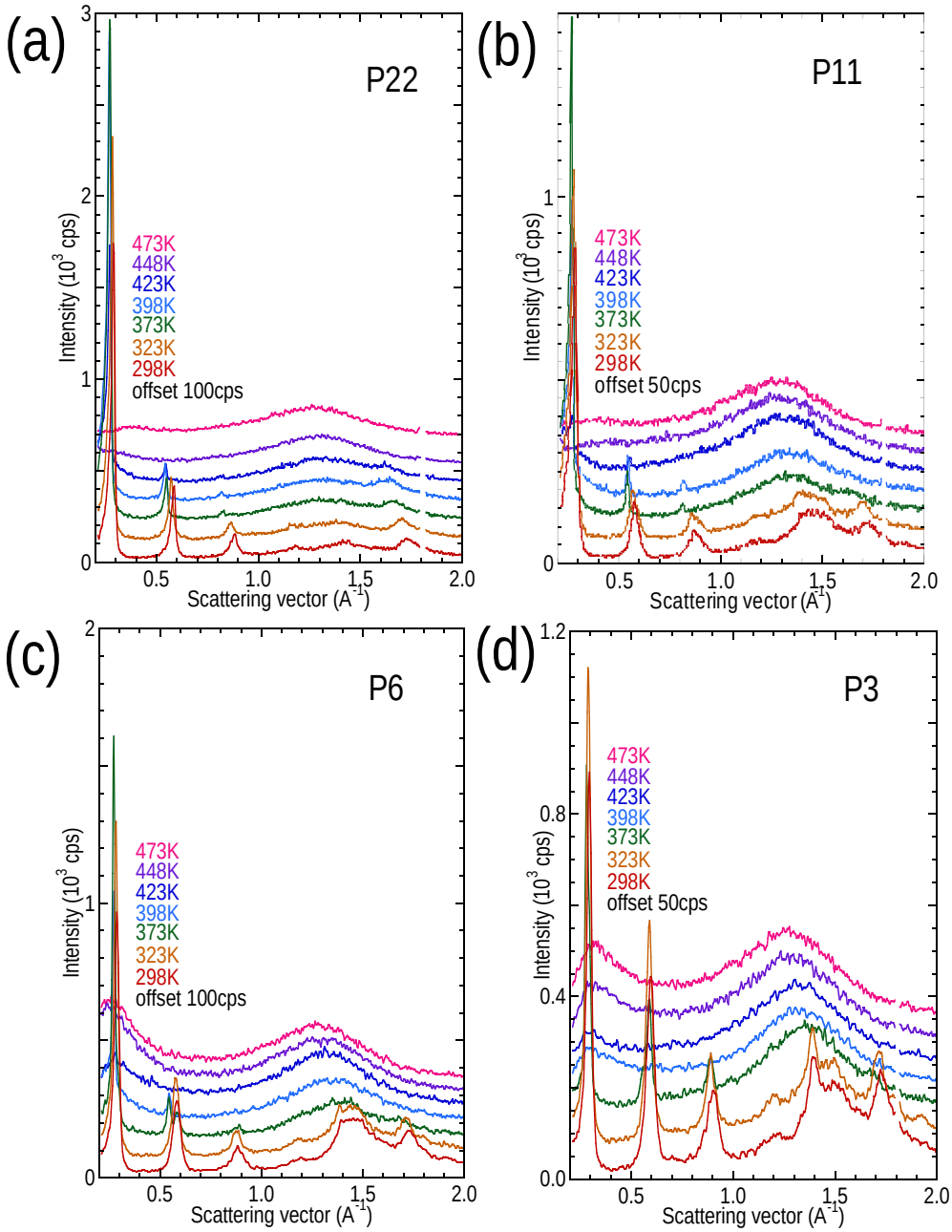

Figure 3.4 XRD patterns of 100-μm-thick PBTTT films recrystallized by annealing to 160ºC (15 min) followed by slow cooling. (a) P22, (b) P11, (c) P6 and (d) P3. Intensities are unnormalized. (cps stands for counts per second)

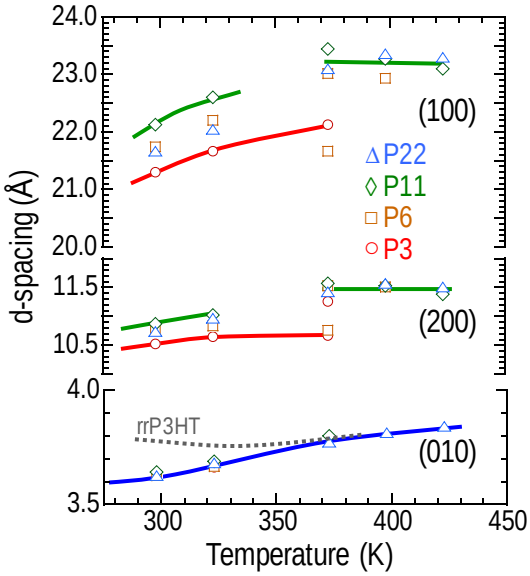

Figure 3.5 d-spacings of (100), (200) and (010) as a function of temperature. (010) spacing of rrP3HT of 3.76Å is also shown.

A Bragg reflection progression of up to five members with fundamental at *ca*. 21.8 Å at room temperature (i.e., 21.8, 10.7, 7.11, 5.30 and 4.35 Å; corresponding to q = 0.29, 0.59, 0.88 and 1.2 and 1.5 Å^{-1}) arises from the well-known (*h00*) lamellar spacing.[30,31] The peak centers were extracted and plotted as a function of temperature in Figure 3.5. They show a small but systematic variation with n_o. The (100) reflection increases by 3.5% on going from P3 to P11, and then falls back to an intermediate value for P22. The most significant observation here is a lamellae→lamellae transition at *ca*. 360–375 K. The temperature step size of 25 K precludes a better precision than 10 K, but it is clear that this phase transition exists both from the break and the different temperature dependence of the *d*-spacing before and after this transition. The same trend is seen in the (200) data also. The high-temperature lamellar phase appears to be more ordered (narrower fwhm) than the low-temperature phase, and has nearly zero thermal expansion coefficient. We speculate it arises from a slightly different average conformation of alkyl side chains, but little else is known at present. In fact the co-existence of these two lamellar phases with slightly different lamellar thicknesses in equilibrium is coincidentally

captured in the XRD of P6, which show the simultaneous presence of two sets of (*h00*) spacings in the 373-K diffractogram.

The Bragg reflection at 3.63 Å (i.e., q = 1.73 Å^{-1}) is truly independent of MW (± 0.01 Å) and assigned to the (010) reflection (we indexed on a primitive orthorhombic lattice for simplicity, for a face-centered orthorhombic lattice, this would have been assigned to (020), but conclusions are unchanged). This corresponds roughly to the π-stacking direction. It has a sigmoidal temperature dependence with a center (*ca*. 320 K) that coincides with the T_r transition. Thus the expansion coefficient of this spacing reaches a maximum (4.7x10^{-4} K^{-1}) around T_r, which is an anomalous behavior attributed to the T_r transition.[32] This *d*-spacing increases smoothly through the lamellae→lamellae transition at 360–375 K. The corresponding reflection for rrP3HT is also shown for comparison. In rrP3HT this reflection occurs at 3.76 Å and has a non-monotonic temperature dependence. Therefore, it is clear that below *ca*. 370 K, the (010) spacing in PBTTT is smaller than in rrP3HT. This suggests that the π-conjugated backbone of PBTTT is more tightly packed than in rrP3HT, which has been pointed out earlier to explain the higher resilience of PBTTT to photo-induced doping in the presence of oxygen and moisture. [33]

The only other reflection with significant intensity occurs at a *d*-spacing of 4.5 Å (i.e., k = 1.40 Å^{-1}) which can be observed particularl in the lower MW samples such as P3 sitting on a broad amorphous halo. The intensity of this peak decreases systematically with increasing MW. It can be assigned to the (003) reflection due to periodicity along the chains (repeat unit distance is 13.8 Å from PM3 molecular modeling). The intensities of expected mixed reflections are very weak or practically absent, in agreement with literature reports. Hence the degree of long-range order of the crystal lattice in other than the (100) and (010) directions is in fact quite poor, similar to rrP3HT.

Therefore these lamellar crystals are “paracrystals” in the sense that there is well-defined long-range order only in the lamellar (thickness) direction and in the π-stacking direction, but not even in the chain-axis direction particularly in the higher MWs. There is certainly no evidence for long-range registration of the alkyl or ring atoms across the lamellar faces.

PBTTT	Peak position (Å) (Scherrer width (Å)[a])			
	(100)	(200)	(300)	(010)
P22	21.66 (560)	10.74 (420)	7.12 (290)	3.63 (130)
P11	22.12 (360)	10.87 (290)	7.16 (140)	3.65 (140)
P6	21.74 (450)	10.76 (250)	7.10 (210)	3.63 (170)
P3	21.30 (400)	10.52 (240)	6.96 (170)	3.64 (180)

Table 3.1 *d*-spacing and effective coherence length of the (*h00*) and (*010*) reflections.

[a] Computed using Scherrer’s equation $D = \frac{K \cdot \lambda}{\theta_{fwhm} \cdot \cos\theta}$, where the Scherrer factor K is 0.9.

We can compute an effective Scherrer coherence length from $D_{\perp} = \frac{K \cdot \lambda}{\theta_{fwhm} \cdot \cos\theta}$, where $D_{\perp}$ is the coherence length in the direction of the *d*-spacing, *K* is the Scherrer shape factor taken to be 0.9, θ_{fwhm} is the full-width at half maximum in radians, θ is the Braggs angle in radians and λ is the X-ray wavelength (1.54 Å). The results are tabulated in Table 3.1 together with the *d*-spacings of the (*h00*) and the (*010*) family of reflections. This $D_{\perp}$ of the (100) reflection is of the order of 40–60 nm for these films. For the (010) reflection, this is *ca*. 18 nm for P3 decreasing to *ca*. 13 nm for P22. Therefore, the paracrystals exhibit physically longer coherence length in the lamellar thickness direction across the lamellar stacks than across the π-stacks. However, these are not considerably better than in rrP3HT. The coherence length in

the π-stack direction evidently is much shorter than the width of typical exposed monolayer terraces (100–500 nm), which are thus likely to comprise a mosaic of sub-domains sharing possibly a mixture of low and high-angle tilt boundaries. The size of these domains is likely to depend on the crystal growth conditions, and is thus not further discussed here.

For P3, the sample at room temperature is semi-crystalline with the (*h*00) reflections where *h* = 1–5, and the (003) and (010) reflections clearly visible, as discussed before. As temperature increases, the (003) and (010) reflections drop in intensity more quickly than (*h*00), so that at 373 K, only the (h00) reflections survive. The material at this temperature thus only exhibits long-range order in the lamellar stacking direction but not in the π-stacking direction. Above 398 K, all long-range order is destroyed but orientation order is preserved, as evidenced by POM birefringence (and also AFM observation of the preservation of the molecular terrace heights), and so the material is in the nematic liquid crystal state. Above 410 K, the material melts to the isotropic phase. Therefore the results suggest the existence of a new state of the polymer chains between the nematic lc and the (para)crystal, where the π-stacks within the lamellae are "melted" but lamellar stacking periodicity remains. At temperatures slightly above the upper limit of its stability, which we denote T_k", the lamellar stacking order is also lost to give the familiar nematic lc, while at temperatures slightly below the lower limit of its stability, which we denote T_k', the π-stacking order is developed to give the also familiar the (para)crystal. We denote this new state a layered nematic lc, which does not appear to have been observed before in polymer liquid crystals. This layered nematic phase has a higher order than the nematic phase because there is a layering of chains. Within the layer however, the chains have orientational order in plane but not positional order. This is related to the well-

known smectic phase, where layering exists, but the mesogen director is perpendicular to the lamellae (not parallel as in this case) and exhibits variable positional order within the lamellae.

We hypothesize that this layered nematic phase results from the molecular-scale phase segregation of the π-conjugated backbone and the alkyl side chains, when thermal disorder is high enough to disrupt the π-stacking but not the lamellar stacking. It is a logical step in the progressive disordering of these highly anisotropic, and may thus be a general state to be found also in other (short-chain) π-conjugated polymers.

For P22, the sample at room temperature is again semi-crystalline with clearly visible (*h*00) reflections, a strong (010) reflection, but a weak (003) reflection. As temperature increases, in contrast to P3, it is the (*h*00) reflections that decrease in intensity relative to the (010) reflection, so that by 423 K, they are very weak compared to the (010) reflection. This suggests that in P22, the π-stacks melt congruently with the lamellar stacks to transit from the (para)crystal state directly to the nematic liquid crystal phase. POM shows that the sample eventually transits to the isotropic melt at 515 K. Furthermore, the transition temperatures are significantly higher than in P3. The results for the intermediate P6 and P11 lie smoothly between these two limits, as an inspection of Figure 4 will show. These results suggest that the nematic lc transition temperatures increase with n_o, while the stability window of the layered nematic lc decreases with n_o.

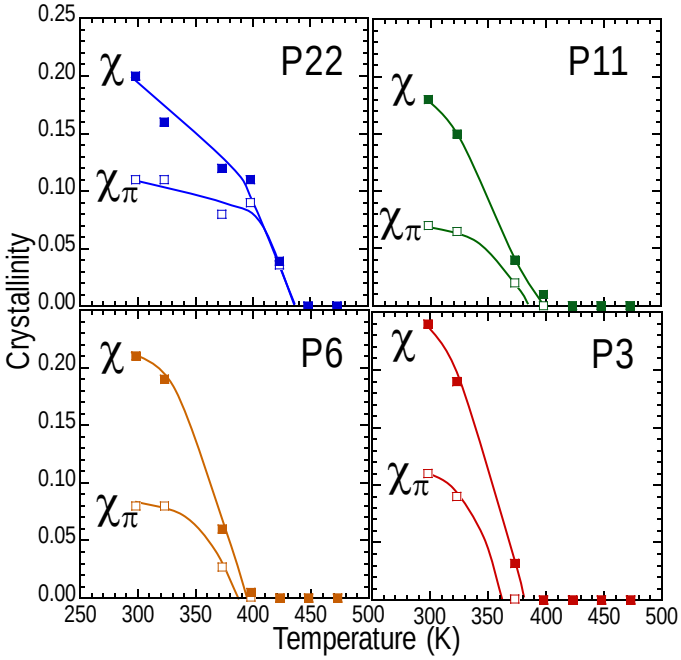

Figure 3.6 Dependence of crystallinity on temperature.

To determine the nematic lc transition temperatures, we extracted the WAXS crystallinity χ and extrapolated to zero to estimate the temperature at which long-range order is completely lost. We also resolved the contribution by the π-stacking order (χ_π) to the crystallinity by integrating the (010) reflection. The diffractograms were corrected for X-ray scattering geometry and polarization effects by multiplying with $\sin^2\theta\cdot\cos\theta$, as in standard practice.[34]

$$\chi = \frac{\int_{Bragg} I\cdot\sin^2\theta\cdot\cos\theta\cdot d\theta}{\int_{total} I\cdot\sin^2\theta\cdot\cos\theta\cdot d\theta}, \text{ and } \chi_\pi = \frac{\int_{(010)} I\cdot\sin^2\theta\cdot\cos\theta\cdot d\theta}{\int_{total} I\cdot\sin^2\theta\cdot\cos\theta\cdot d\theta},$$

where θ is the scattering angle.[34] This weighting function strongly amplifies the intensity of mid-angle Bragg reflections relative to the low-angle reflections. The difference between χ and χ_π is the contribution by the lamellar stacking order (since the contribution by (003) is negligible). The results are shown in Figure 3.6. Clearly, for P3, both χ and χ_π decay with increasing temperatures, but χ_π disappears before χ, as confirmed by the 373-K diffractogram, which reveals the layered

nematic lc phase discussed earlier existing between *ca*. 360–380 K. For the higher MWs (P6 and P11), χ_π decays more slowly with temperature, as revealed by its increasing contribution to χ at 373 K. Therefore temperature stability range of the layered nematic phase (visible in the 398-K diffractograms, Figure 4) shrinks. For P22, χ_π in fact makes the dominant contribution to χ for temperatures ≥ 400 K, as confirmed by the 423-K diffractogram. The thermal stability of the π-stacks appears to "prop up" the overall thermal stability of the lamellae, which then melts directly into the isotropic phase.

It is clear from the data that the thermal stability of the π-stacking long-range order increases with MW. At low MW, the π-stacks appear to melt before the lamellar structure to give rise to an intermediate layered nematic lc below the final melting to the isotropic phase. At high MW, the π-stacks help stabilize the lamellar structure, which then melts directly to the isotropic phase.

3.3.4 Phase diagram: dependence of T_k and T_i on chain length

The phase diagram summarizing the results from variable-temperature POM and WAXS is shown in Figure 3.7. To quantify the dependence of T_i on MW, we assume that it obeys the melting point depression equation: $T = T^o \frac{A+n}{B+C\ln n+n}$, where T^o is the transition temperature in the infinite-chain limit, and *A*, *B* and *C* are dimensionless parameters that respectively relate to the relative contribution to the enthalpy of chain ends, entropy of chain ends and the Flory chain-end decorrelation term.[14,35] This equation can be derived from the standard equation $T = \frac{\Delta H}{\Delta S}$ for phase equilibrium, assuming $\Delta H = n \cdot \Delta h^{ru} + \Delta h^{end}$ and

$\Delta S = n \cdot \Delta s^{ru} + \Delta s^{end} + \Delta s^{conf} \cdot \ln n$, where the superscripts "*ru*", "*end*" and "*conf*" denote respectively the repeat unit, chain end and conformational contributions. This assumes that the temperature dependence of ΔH and ΔS is zero, which requires that heat capacity change ΔC_p to be zero. This assumption is confirmed to be valid by the lack of significant change in the baseline of the DSC thermograms at the onset and end of these transitions. Then

$$A = \frac{\Delta h^{end}}{\Delta h^{ru}}; \quad B = \frac{\Delta s^{end}}{\Delta s^{ru}}; \text{ and } C = \frac{\Delta s^{conf}}{\Delta s^{ru}}; \text{ with } T^o = \frac{\Delta h^{ru}}{\Delta s^{ru}}.$$

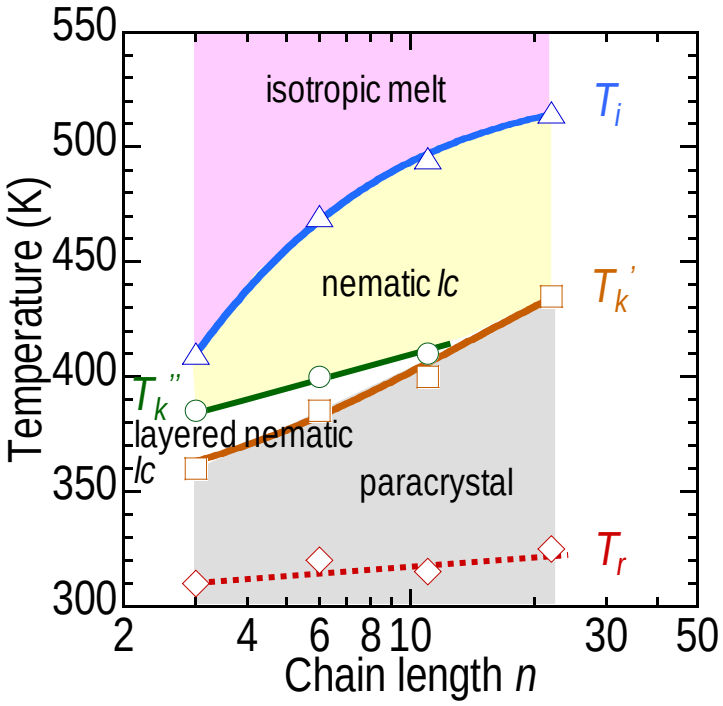

Figure 3.7 Phase diagram showing the dependence of T_r, T_k, T_k' and T_i transition with n_0. The useful liquid crystalline gap between T_k and T_i opens up significantly with n_0. T_r shows slow increase with n_0.

The best-fit curve (dark blue) through the T_i data in Figure 3.7 gives A = 0.041, B = 1.1, C = –0.15, T^o = 525 K (R^2 = 0.9985), which suggests that the end-chain contributions to enthalpy is larger than for entropy, which appears reasonable. The asymptotic behavior shows that P22 has practically attained the infinite-chain limit in its isotropic melting behavior. If we assume the

same considerations apply to the melting of the paracrystal, the best-fit curve (orange) through the T_k' data gives A = 7.4, B = 11, C = 0.26, T^o = 500 K (R^2 = 0.9828), which suggests a sizeable end-chain contribution to both enthalpy and entropy, which is also reasonable for this transition. The net competition between these two effects is that the temperature stability range of the useful nematic lc phase at first increases with MW, and then diminishes, and achieves a maximum for n = 10–20.

3.4 Summary

A set of rich thermal transitions have been observed in highly crystalline polymer PBTTT of various MW. For small degree of polymerisation n_o, detailed VT-XRD and VT-POM π-stacks melt tens of degree K earlier than the lamellar order to give a new ordered nematic phase (related to the smectic phase of low-molecular-weight mesogens but with the director oriented in-plane and no positional order), but for large n_o, both melt congruently to the nematic phase. We can thus establish that the 150ºC transition to comprise two-closely occurring liquid crystal transitions to the layered and normal nematic phases T_k' and T_k''. These temperatures and the isotropic melt temperature T_i saturate for n_o > 10, but the ring-twist transition temperature T_r is largely independent of n_o.

3.5 References

1 McCulloch, I. *et al.* Liquid-crystalline semiconducting polymers with high charge-carrier mobility. *Nature Mater.* 5, 328-333 (2006).

2 Zhang, R. *et al.* Nanostructure dependence of field-effect mobility in regioregular poly(3-hexylthiophene) think film field effect transistors. *J. Am. Chem. Soc.* 128, 3480-3481 (2006).

3 Kline, R. J. *et al.* Dependence of regioregular poly(3-hexythiophene) film morphology and field-effect mobility on molecular weight. *Macromolecules* 38, 3312-3319 (2005).

4 Ihn, K. J., Moulton, J. & Smith, P. Whiskers of poly(3-alkylthiophene)s. *J. Polym. Sci. Part B: Polym. Phys.* 31, 735-742 (1993).

5 Zen, A. *et al.* Effect of molecular weight and annealing of poly(3-hexylthiophene)s on the performance of organic field-effect transistors. *Adv. Funct. Mater.* 14, 757-764 (2004).

6 Kline, R. J., McGehee, M. D., Kadnikova, E. N., Liu, J. & Fréchet, J. M. J. Controlling the field-effect mobility of regioregular polythiophene by changing the molecular weight. *Adv. Mater.* 15, 1519-1522 (2003).

7 Chang, J. F. *et al.* Enhanced mobility of poly(3-hexylthiophene) transistors by spin-casting from high-boiling-point solvents. *Chem. Mater.* 16, 4772-4776 (2004).

8 Chang, J. F. *et al.* Molecular-weight dependence of interchain polaron delocalisation and exciton bandwidth in high-mobility conjugated polymers. *Phys. Rev. B* 74, 115311-115312 (2006).

9 Liu, J., Arif, M., J., Z., Khondaker, S. I. & Zhai, L. Controlling poly(3-hexylthiophene) crystal demension: nanowhiskers and nanoribbons. *Macromolecules* 42, 9390-9393 (2009).

10 Kim, D. H., Park, Y. D., Jang, Y., Kim, S. & Cho, K. Solvent vapor-induced nanowire formation in poly(3-hexylthiophene) thin films. *Macromol. Rapid Commun.* 26 (2005).

11 Samitsu, S., Shimomura, T., Heike, S., Hashizume, T. & Ito, K. Effective production of poly(3-akylthiophene) nanofibers by means of whisker method using anisole solvent: structural, optical, and electrical properties. *Macromolecules* 41, 8000-8010 (2008).

12 Malik, S. & Nandi, A. K. Crystallization mechanism of regioregular poly(3-alkyl thiophene)s. *J. Polym. Sci. B, Polym. Phys.* 40, 2073-2085 (2002).

13 Hugger, S., Thomann, R., Heinzel, T. & Thurn-Albrecht, T. Semicrystalline morphology in thin films of poly(3-hexylthiophene). *Colloid Polym. Sci.* 2004, 932-938 (2004).

14 Gedde, U. W. *Polymer physics*. (Chapman & Hall, 1995).

15 Huber, K., Bantle, S., Lutz, P. & Burchard, W. Hydrodynamic and thermodynamic behavior of short-chain polystyrene in toluene and cyclohexane at 34.5ºC. *Macromolecules* 18, 1461-1467 (1985).

16 Sperling, L. H. *Introduction to physical polymer science*. Third edn, (Wiley-interscience, 2001).

17 Heffner, G. W. & Pearson, D. S. Molecular characterisation of poly(3-hexylthiophene). *Macromolecules* 24, 6295-6299 (1991).

18 Rughooputh, S. D. D. V., Hotta, S., Heeger, A. J. & Wudl, F. Chromism of soluble polythienylenes. *J. Polym. Sci. B, Polym. Phys.* 25, 1071-1078 (1987).

19 Inganäs, O., Salaneck, W. R., Österholm, J. E. & Laakso, J. Thermochromism and solvatochromism effects in poly(3-hexylthiophene). *Synth. Met.* 22, 395-406 (1988).

20 Yoshino, K., Nakajima, S., Park, D. H. & Sugimoto, R. Thermochromism, photochromism and anamolous temperature dependence of luminescence in poly(3-alkylthiophene) film. *Jap. J. Appl. Phys.* 27, L716-718 (1988).

21 Inganäs, O., Gustafsson, G., Salaneck, W. R., Österholm, J. E. & Laakso, J. Thermochroism in thin films of poly(3-alkylthiophenes). *Synth. Met.* 28, C377-384 (1989).

22 Tashiro, K. *et al.* Structure and thermochromic solid-state phase transition of poly(3-alkylthiophene). *J. Polym. Sci. B, Polym. Phys.* 29, 1223-1233 (1991).

23 Zerbi, G., Chierichetti, B. & Inganäs, O. Thermochromism in polyalkylthiophenes: molecular aspects from vibrational spectroscopy. *J. Chem. Phys.* 94, 4646-4658 (1991).

24 Tashiro, K. *et al.* Structure and thermochromic solid-state phase transition of poly(3-alkylthiophene): III. Effects of alkyl side chain length on the phase transitional behavior. *Synth. Met.* 55-57, 321-328 (1993).

25 Wang, S. *et al.* Solvent effects and multiple aggregate states in high-mobility organic field-effect transistors based on poly(bithiophene-alt-thienothiophene). *Appl. Phys. Lett.* 93, 162101-162103 (2008).

26 McCulloch, I. *et al.* Semiconducting thienothiophene copolymers: design, sythesis, morphology, and performance in thin-film organic transistors. *Adv. Mater.* 21, 1091-1109 (2009).

27 Northrup, J. E. Atomic and electronic structure of polymer organic semiconductors: P3HT, PQT and PBTTT. *Phys. Rev. B* 76, 245201-245206 (2007).

28 Cao, M. Y. & Wunderlich, B. Phase transitions in mesophase macromolecules. V. Transitions in poly(oxy-1,4-phenylene carbonyl-co-oxy-2,6-naphthaloyl). *J. Polym. Sci. B. Polym. Phys.* 23, 521-535 (1985).

29 Bershtein, V. A. & Egorov, V. M. *Differential scanning calorimetry of polymers: physics, chemistry, analysis, technology*. (Ellis Horwood, 1994).

30 Chabinyc, M. L., Toney, M. F., Kline, R. J., McCulloch, I. & Heeney, M. X-ray scattering study of thin films of poly(2,5-bis(3-alkylthiophen-2-yl)thieno[3,2-*b*]thiophene). *J. Am. Chem. Soc.* 129, 3226-3237 (2007).

31 Brocorens, P. *et al.* Solid-state supramolecular organisation of polythiophene chains containing thienothiophene units. *Adv. Mater.* 21 (2009).

32 Zhao, L. H. *et al.* On the origin of the monolayer-terraced morphology poly(bithiophene-*alt*-thienothiophene) (PBTTT) films: the role of solvent-induced pre-ordering into 2-d π-stacked extended-chain lamellae aggregates. *Manuscript in preparation* (2010).

33 Zhuo, J. M. *et al.* Direct spectroscopic evidence for a photodoping mechanism in polythiophene and poly(bithiophene-alt-thienothiophene) organic semiconductor thin films involving oxygen and sorbed moisture. *Adv. Mater.* 21, 4747-4752 (2009).

34 Cullity, B. D. *Elements of X-ray diffraction*. (Addison-Wesley, 1978).

35 Flory, P. J. & Vrij, A. Melting points of linear-chain homologs: the normal paraffin hydrocarbons. *J. Am. Chem. Soc.* 85, 3548-3553 (1963).

Chapter 4. Evidence for the T_r ring-twist transition in PBTTT

In this chapter, we demonstrate the existence of a previously unknown cooperative second-order ring-twist transition in PBTTT at 320 K, denoted here T_r, by detailed variable temperature FTIR, Raman and UV-vis spectroscopies. We find that this T_r transition preserves the backbone persistence length unlike the well-known rod-to-coil transition widely studied in rrP3HT. It shifts the phonon frequencies of backbone and CH out-of-plane modes (Raman and infrared) which can thus report the ring-twist angles through PM3 semiempirical quantum chemical calculations. We found excellent spectroscopic agreement that these angles increase from *ca*. 0º to 5–25º several tens of K above T_r, which occurs at 320 K for PBTTT, depending on the inter-ring bond.

4.1 Introduction

A few thermal transitions have been observed from DSC of PBTTT in last chapter, which are denoted T_r at *ca.* 320K, T_k due to melting from a paracrystal phase to a less ordered nematic phase, and T_i due to isotropic melting. These transitions have previously been identified and described.[1,2] Both the T_k and T_i transitions are well-established first-order transitions, and show the expected under-cooling that usually occurs in nucleated transitions. The 320-K transition however does not show significant hysteresis and the peak disappears into a very broad heat-capacity step for low molecular-weight materials. This 320-K transition was previously assigned to side-chain melting. In fact such a broad heat-capacity step has also been found in thermotropic liquid crystalline polymer, where it has been interpreted as an anomalous glass transition.[3] We will show here in fact that the disordering of side chains occurs at an onset temperature of 220 K, and the 320-K transition is a new second-order transition that involves ring twists of the π-conjugated backbone. In order to examine the 320K transition, we took P11 to perform a variable temperature spectroscopy measurement for this chapter, followed by semi-empirical PM3 quantum chemistry calculation to verify the origin of this transition.

4.2 Experimental methods

4.2.1 General PBTTT film preparation

The native silicon oxide substrates were cleaned by an SC-1 recipe (H_2O:H_2O_2:NH_4OH = 10:2:0.5; 75ºC, 30 min), followed by oxygen plasma (10 min) and then silylated with hexamethyldisilazane (HMDS) in the vapor phase (hotplate 120°C, 10 min). 30-nm-thick PBTTT (P11) films were then spin-coated on these substrates from 10 mg/mL PBTTT in

chlorobenzene at 85 °C after cooling down for 30 min before spinning. The films were then annealed above LCP (hotplate 150°C for 10 min) in the glovebox to remove residual solvents and recrystallize the polymer.

4.2.2 Variable temperature spectroscopies

Variable-temperature Fourier-transform infrared (FTIR) spectra were collected on a Nicolet 8700 FTIR spectrometer on a uniform 700-nm-thick film of PBTTT drop-cast from 10 mg/mL chlorobenzene solution (annealed to 85°C in glovebox, then cooled to room temperature for 30 min before casting) onto intrinsic silicon wafers with native oxide and recrystallized by annealing in the glovebox (150ºC, hotplate, 10 min; then slowly cooled to room temperature). The sample was mounted into a closed cycle He cryostat (Janis APD HC-2) with KBr windows and evacuated to 10^{-6} mbar.

Variable-temperature Raman spectra were collected on a Renishaw 2000 Raman microscope with 514-nm Ar-ion laser excitation through x5 microscopy objective on a 50-nm-thick film of PBTTT spin-cast from the same solution onto a 0.17-mm-thick glass cover slip, and recrystallized as before. The polymer film was encapsulated in nitrogen with 0.17-mm glass cover slip and Parafilm spacer to avoid photo-oxidation during measurement. The sample was mounted on a Linkam THMS600 hotstage. The wavenumber axis was calibrated with Si Γ phonon defined to be 520.0 cm^{-1}.

Variable-temperature UV-Vis spectra were collected using a home-built transmission rig on a 100-nm-thick film of PBTTT spin-cast from the same solution on a fused silica substrate and

recrystallized as before. The sample was mounted into a closed cycle He cryostat (Janis APD HC-2) with fused silica windows and evacuated to 10^{-6} mbar.

4.2.3 Quantum chemical calculations

We described the local molecular geometry using a three-repeat unit oligomer conformational model α,ω-dibromo-(3-ethylthiophene-2,5-diyl)-thieno[3,2-b]thiophene-5,5'-diyl-(3-ethylthiophene-2,5-diyl) with two unique dihedral angles in an overall S_2 symmetry (i.e., the two non-equivalent thiophene rings lie on different planes separated by angle θ, while the thienothiophene plane is separated from the adjacent thiophene plane by angle ϕ). This provides a simple long-range correlation of the dihedral angles that preserve the persistence length of the chain that is consistent with experiment. The ground-state geometry was first optimised using the semiempirical MNDO-PM3 Hamiltonian, and the π–π^* electronic spectrum and phonon mode spectra were then computed and scaled using monomer models. The MNDO-PM3 Hamiltonian is well known to give accurate molecular structures of large π-conjugated molecules at reasonable computation costs. (e.g., the computed $C_\alpha C_\beta$, $C_\beta C_\beta$ and SC_α bond lengths are all within 0.02 Å of experimental values for oligothiophenes) Br termination in the 5-position was found to be effective to suppress the oligomer end effect. The T_2 and TT CH δ_{oop} modes were assigned from correspondence with unambiguous modes in the monomers (5,5'-dibromo-4,4'-bistetradecyl-2,2'-bithiophene, 804 cm^{-1}; 2,5-bis(trimethylstannyl)thieno[3,2-b]thiophene, 820 cm^{-1}).

To take into account the background temperature dependence of the phonon mode frequency (such as arising from bond anharmonicity), we define the "excess" thermal shift here as the

deviation from the low-temperature trend. This excess shift is then fitted to the computed mode frequency vs (θ, ϕ) surface to extract the (θ, ϕ) vs temperature trajectory.

4.3 Results and discussions

4.3.1 Evidences for a well-defined 320K transition in variable temperature spectroscopies

Figure 4.1(a) shows the differential scanning calorimetry (DSC) thermogram of a highly-ordered PBTTT thick film that has been pre-annealed to 423 K in the sample pan in the glovebox. This film gives three sets of transitions at 510 K, 420 K and 320 K. These three transitions have been reported in the literature[1,2] but the origins of 420-K and 320-K transitions have not been full established. They were speculatively assigned to side-chain melting and to an "unknown origin" respectively. From detailed polarised optical microscopy and variable temperature X-ray diffraction, we can firmly assign the 510-K and 420-K transitions to melting to the isotropic phase (T_i) and melting to the nematic liquid crystalline phase (T_k) respectively in 0. They both show the characteristic under-cooling of first-order phase transitions during thermal cycling. The 320-K transition on the other hand does not show significant under-cooling. Furthermore, it evolves into a broad heat-capacity step for low molecular weight PBTTT. Such a feature has also been found also in other thermotropic liquid crystalline polymers, where it has been interpreted as an anomalous glass transition.[3] We will show here in fact that this 320-K transition is a second-order ring-twist transition (T_r) of the π-conjugated backbone. In contrast, the disordering of side chains occurs at a much earlier onset temperature of 220 K.

Figure 4.1(b) shows the temperature-dependent π–π^* UV-Vis absorption spectra of a highly-ordered PBTTT thin film. The spectra show a blue shift and a broadening of the vibronic features above room temperature. Figure 4.1(c) shows the temperature dependence for the mean transition energy <*E*> of this π–π^* band. This is defined by $< E >= \frac{\int_{band} AEdE}{\int_{band} AdE}$, where *A* is the absorbance, integrating over the entire band from 1.8 to 3.2 eV. The temperature dependences of <*E*> and its derivative d<*E*> / d*T* reveal a change of slope and a step respectively at *ca*. 320 K. The temperature coefficient is initially relatively constant at 1 x 10^{-4} eV K^{-1} below 300 K, but increases at 320 K to continually increase over the next 150 K. Similar results were obtained when plotting the red edge (at half height) of the transition. These temperature dependences (together with the thermal data) are characteristic of a second-order transition occurring at 320 K.

Figure 4.2 (a) shows the key phonon modes in the temperature-dependent FTIR absorption spectra of a highly-ordered PBTTT thick film: side-chain alkyl CH_2 rock (CH_2 ρ), bithiophene (T_2) and thienothiophene (TT) backbone CH out-of-plane bend (CH δ_{oop}), alkyl CH_2 bend (CH_2 δ), CH_2 symmetric and asymmetric stretch (ν_s and ν_{as}) and backbone CH stretch (CH ν). The FTIR spectrum is completely dominated by CH modes because of their large vibrational dipole moment. These mode assignments are confirmed by quantum chemical calculations, group frequencies[4] and extensive literature.[5,6]

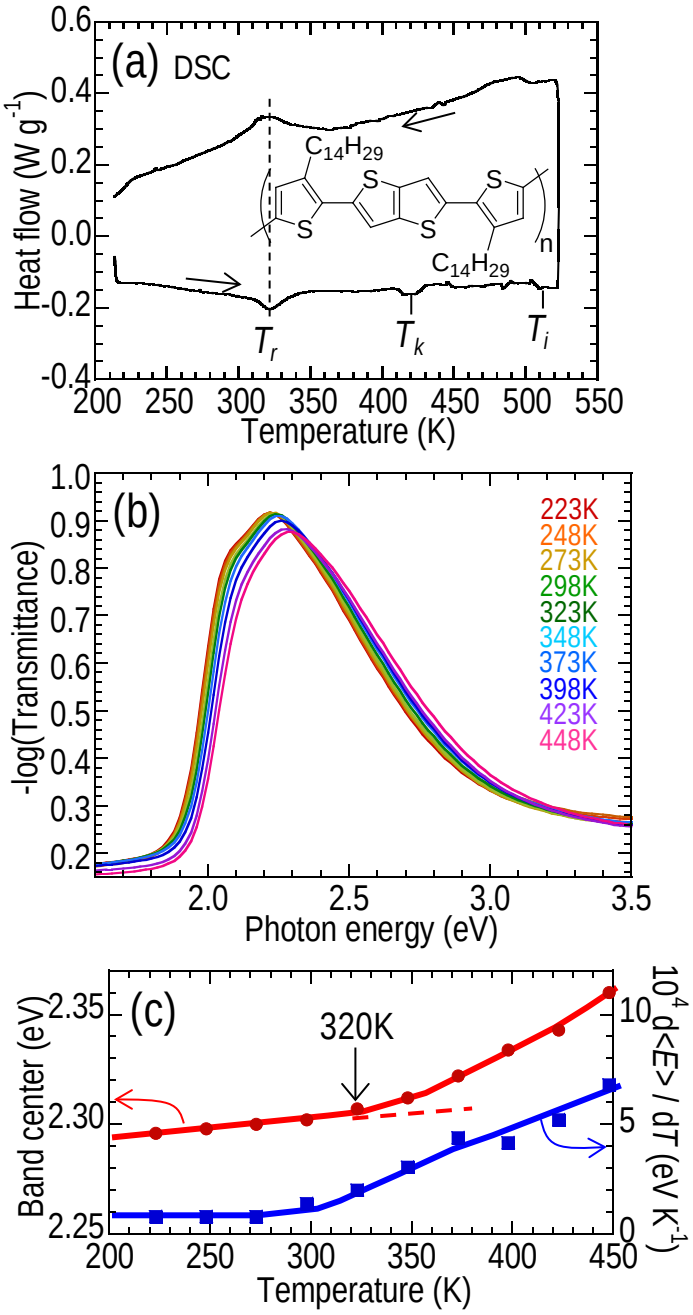

Figure 4.1 The second-order nature of the 320-K transition in well-ordered PBTTT films (pre-annealed on hotplate 150ºC; 10 min; N_2). (a) First-cycle differential scanning calorimetry in Al pans measured in flowing N_2. Inset: Chemical structure of PBTTT. (b) UV-visible transmittance spectra on fused silica substrates measured in vacuum. (c) Plots of mean π–π^* transition energy and its temperature dependence against temperature. Lines are guides to the eye.

The key observation here is that the temperature dependence of these modes falls neatly into two types. This can be clearly seen in the temperature plots of their mean phonon wavenumbers $<\bar{\nu}>$ (Figure 4.2(b)), defined by $<\bar{\nu}>=\frac{\int_{mode} A\bar{\nu}d\bar{\nu}}{\int_{mode} Ad\bar{\nu}}$, where *A* again is the absorbance, and integrating over the entire phonon band: (i) The alkyl side-chain modes (CH_2 ρ and δ) show very little temperature dependence from 77 K until *ca*. 220 K, at which they shift and broaden continually until beyond T_k. This is characteristic of the dynamic *trans* (T)→*gauche* (G) disordering of the alkyl-chain segments.[5,6] Moreover the intensities of the *gauche* CH_2 δ modes (1455 and 1432 cm^{-1}) increase at the expense of the *trans* CH_2 δ mode (1470 cm^{-1}). Also the GTG' CH_2 ω mode at 1365 cm^{-1} intensifies, while the CH_2 ρ mode diminishes and broadens. Therefore, it is firmly established that side-chain disordering in PBTTT occurs at an onset temperature of 220 K. Similar changes also occur in rrP3ATs[7-9] and hexabenzocoronenes.[10] (ii) In contrast, the backbone modes of the T_2 and TT rings (both CH δ_{oop} and ν) show very little temperature dependence until *ca*. 320 K after which they shift and broaden. This shows that backbone conformational motion onsets *ca*. 100 K above that of the side chain motion.

Thus the temperature dependence of all the modes that are sensitive to the alkyl-chain conformation unequivocally agree that the side-chain "freezes" into an imperfect all-*trans* conformation below 220 K (as evidenced by the residual *gauche* CH_2 δ intensities) and is substantially disordered at room temperature. Therefore, there is no evidence for the literature suggestions of all-*trans* alkyl side-chains and 3-dimensional alkyl-chain interdigitation. This is further in accord with the weak intensity of mixed-indexed X-ray reflections[11,12] that are not anyway too different from those of rrP3ATs.[13]

Figure 4.2(c) shows the temperature-dependent Raman spectra of the PBTTT film for the C=C–C backbone ring-stretch region. These modes have been labeled ν_1 to ν_4 in the order of decreasing Raman shift. The temperature dependence of ν_4 also shows a kink at 320 K (inset of Figure 2c). Quantum chemical calculations show that some of these phonon modes are particularly sensitive to the polymer chain conformation. This allows us to infer from their temperature dependence the ring-twist dihedral angles, for the first time.

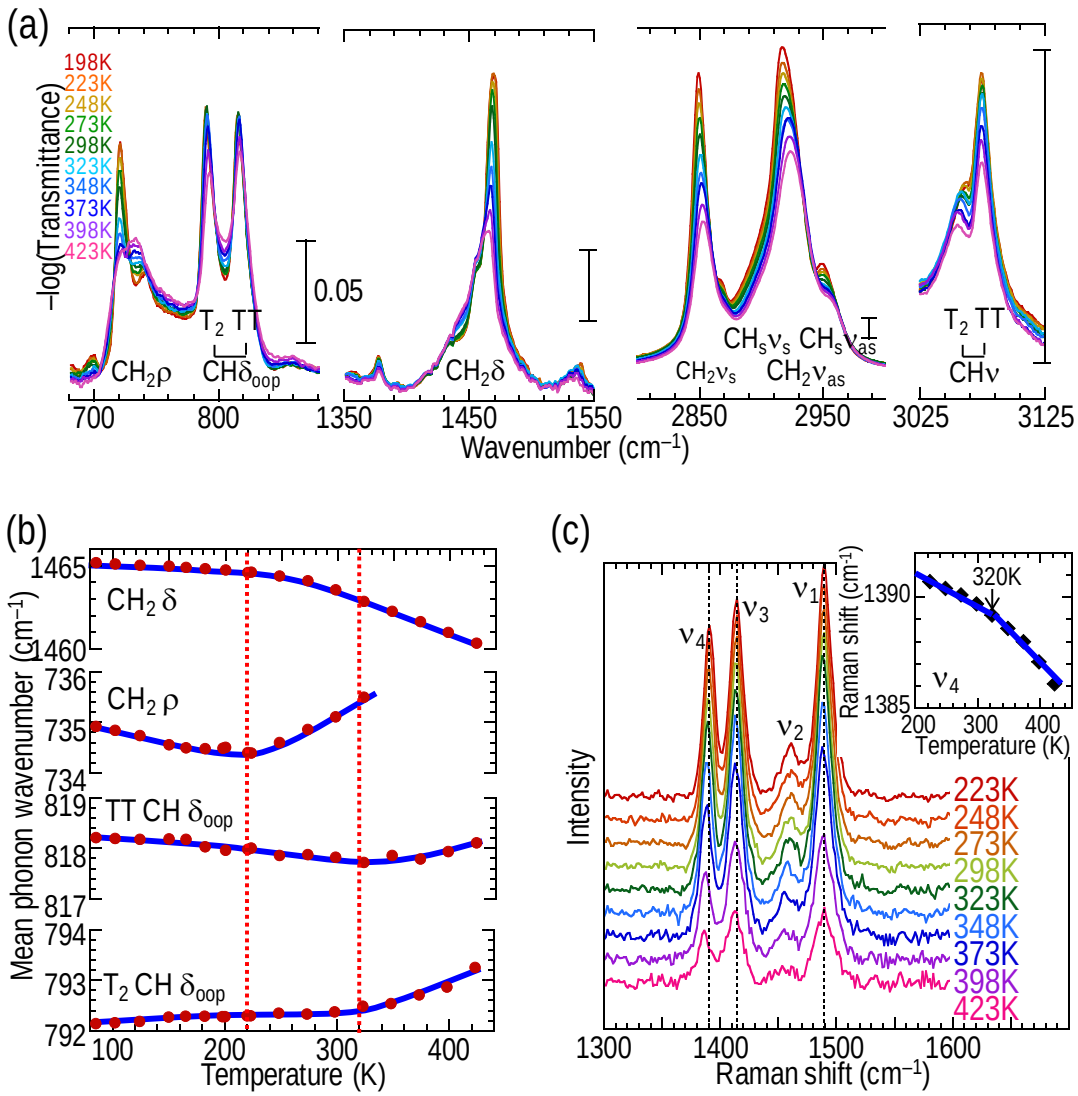

Figure 4.2 Temperature-dependent FTIR and Raman spectra reveal separate onset temperatures for side-chain disordering (220 K) and ring-twisting (320 K) in well-ordered PBTTT films. (a) Temperature dependence of the FTIR phonon modes: alkyl CH_2 rock (CH_2 ρ), bithiophene (T_2) and thienothiophene (TT) CH out-of-plane bend (CH δ_{oop}), alkyl CH_2 bend (CH_2 δ), CH_2 symmetric (ν_s) and asymmetric (ν_{as}) stretch and aromatic CH stretch (CH ν). Scale bar corresponds to 0.05 absorbance units. (b) Plot of mean phonon wavenumber against temperature for selected phonon modes. Lines are guides to the eye. (c) Temperature dependence of the Raman C=C–C backbone stretching phonon modes ν_1–ν_4. Inset: Plot of ν4 against temperature.

4.3.2 Quantitative determination of dihedral ring-twist angle by quantum chemical calculations

For these calculations, we employed a simple conformer model of a three-repeat-unit oligomer characterised by two unique dihedral angles, θ between the adjacent thiophene rings, and ϕ between the thienothiophene and thiophene rings, and with *anti* orientation of the rings, as known in oligothiophenes[14,15] and polythiophene.[16] We impose a long-range correlation of the sense (and magnitude) of rotation of θ and ϕ in S_2 symmetry to reproduce the experimentally known long coherence of the chains in the solid state. Variable-temperature AFM has confirmed that the lamellae structure, and hence the long persistence length of the PBTTT chains in the solid film, persists to T_k (Figure 4.3), while polarized optical microscopy has confirmed chain anisotropy persists to T_i (Figure 3.2).

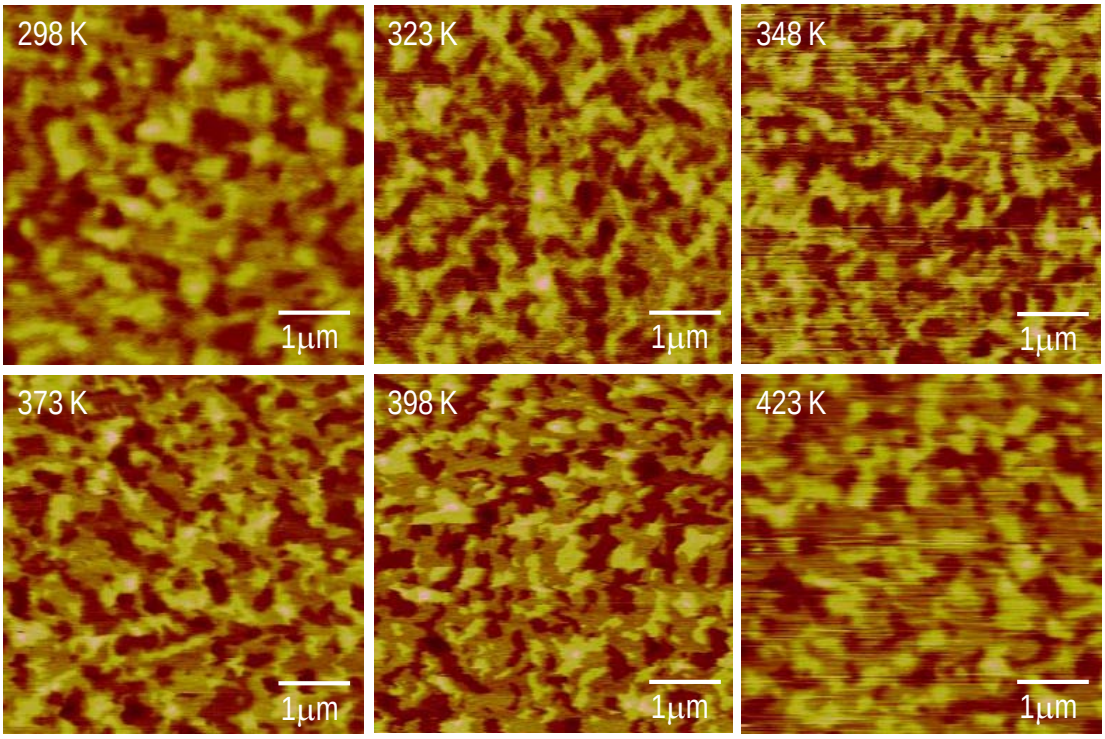

Figure 4.3 Variable temperature-AFM images of pBTTT film from room temperature up to 423K

A fragment of the conformer model is shown in Figure 4.4 (f). Because the ring torsional modes are far slower (< 80 cm^{-1})[17] than the backbone vibrational modes, the dihedral angles can be regarded stationary at appropriate mean values, for the backbone vibrational and electronic transitions. The ground-state geometry was optimised for every (θ, ϕ) value, the electronic structure was computed, followed by the phonon mode spectrum at the PM3 semiempirical level.

Figure 4.4 (a) – (d) show the computed mode frequency *vs* (θ, ϕ) together with schematic illustrations of the mode pattern (i.e., atomic displacements). Although the absolute frequencies have to be scaled to match experiment as is standard practice, their variation with (θ, ϕ) are small perturbations and are thus reliable. The calculations reveal that because of localisation, the T_2 and TT CH δ_{oop} modes blue shift independently with θ and ϕ respectively (Figure 4.4 (a) and (b)). Hence it is possible to infer the change in these angles from the shift of these modes quite reliably. However it is also useful to have an independent confirmation from backbone C=C-C modes. We found the three highest-frequency C=C–C Raman branches (ν_1 to ν_3) are localised within the T_2 unit with the centre TT bond stationary (Figure 4.4(c)), while the ν_4 branch is delocalized (Figure 4.4(d)). These four modes involve significant the benzenoid–quinoid oscillation and hence large Raman cross-sections. In particular the frequencies of both the ν_1 and ν_4 modes depend on (θ, ϕ) significantly.

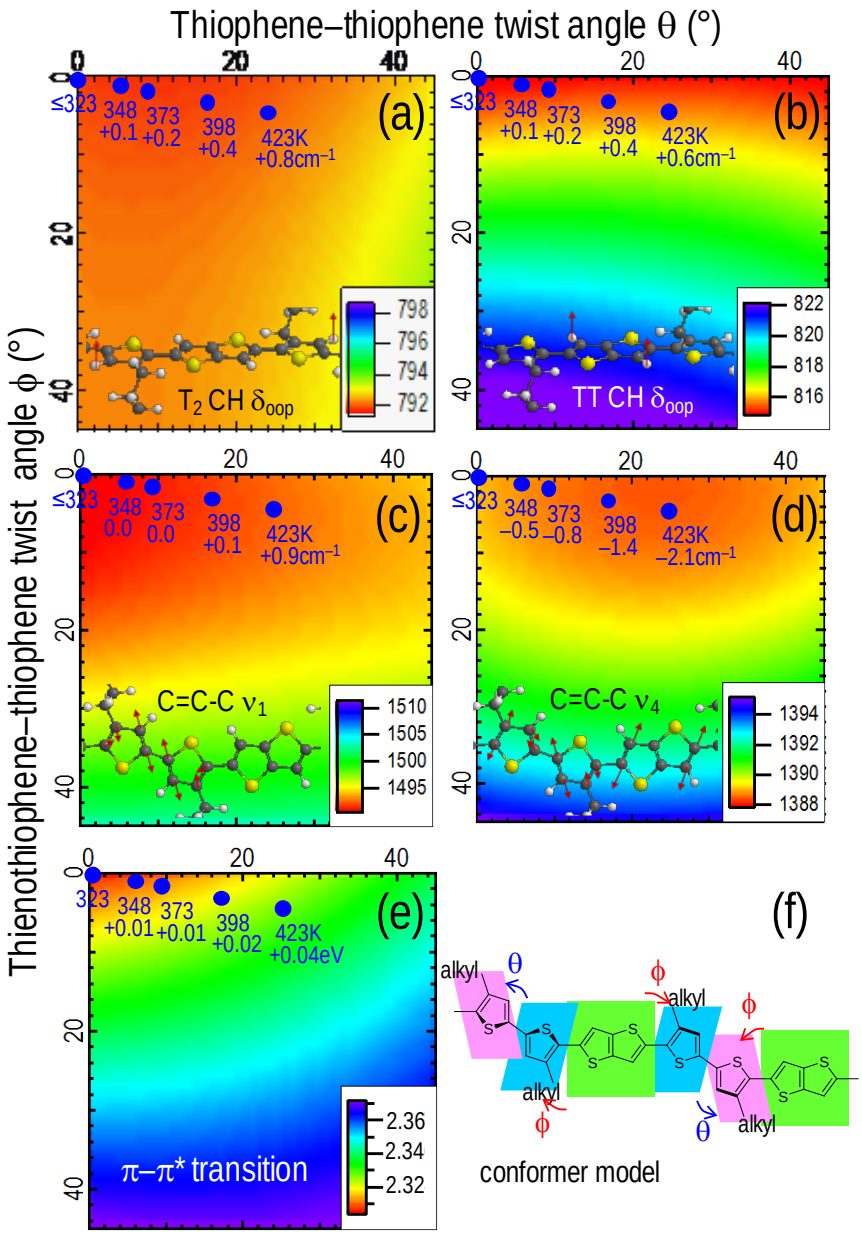

Figure 4.4 Computed spectral properties parametric in thiophene–thiophene dihedral angle (θ) and thienothiophene–thiophene dihedral angle (ϕ) to extract their temperature dependence from experimental results. Computed phonon mode frequency surface for: (a) T_2 CH_{oop}, (b) TT CH_{oop}, (c) C=C–C ν_1, and (d) C=C–C ν_4. (e) Computed mean π–π* electronic transition energy surface. (f) Schematic diagram of the conformer model used in the quantum chemical calculations. The computed phonon mode frequencies and electronic transition energy were scaled by standard corrections. The blue dots give the best (θ, ϕ) coordinates that account for the experimental excess mode shift at various temperatures. A self-consistent temperature trajectory was obtained in this way to fit all the phonon mode data. This trajectory also describes excellently the π–π* transition energy data.

We found a self-consistent (θ, ϕ)–temperature trajectory that simultaneously describes the excess thermal shifts of all these four phonon modes (see the blue dots in Fig. 3a–d). This validates our model and provides confidence in the results. We have assigned the initial state (θ, ϕ) below 320 K to (0º, 0º) in agreement with the known crystal structure of oligothiophenes[14,15] and polythiophene.[16] Above 320 K, we found that ϕ and in particular θ increase significantly with T to reach (θ, ϕ) = (25º, 5º) just below T_k. We also plot in Figure 3e this trajectory superimposed on the computed π–π* transition energy surface. We found an excellent agreement between the experimental shift in the mean π–π* energy (+ 40 meV) and the computed results. This demonstrates that the 320-K transition is the T_r transition.

The observation that $d\theta/dT > d\phi/dT$ indicates that the ring twist occurs preferentially about the thiophene–thiophene inter-ring bond rather of the thienothiophene–thiophene bond. This suggests that the ring twist is driven by conformational mobility of the alkyl side chains attached to the thiophene rings in competition with π-electron delocalization, which tends to planarise the backbone.

Variable-temperature X-ray diffraction results are also in accord with the T_r transition, which was shown in last chapter. The (010)-spacing which is nearly parallel to the π-stacking direction shows a thermal expansion coefficient of 4.7×10^{-4} K^{-1} between 320 K and 370 K, which is much larger than those of acenes in the basal plane direction ($< 1 \times 10^{-4}$ K^{-1}).[18] On the other hand, the (100)-spacing shows an anomalous contraction over this temperature range.

4.4 Summary

Using a well-ordered highly crystalline PBTTT as model polymer semiconductor, we demonstrate here the existence of a previously unknown cooperative second-order ring-twist transition, denoted here T_r. This T_r transition preserves the backbone persistence length unlike the well-known rod-to-coil transition. It shifts the phonon frequencies of backbone and CH out-of-plane modes (Raman and infrared) which can thus report the ring-twist angles through PM3 semiempirical quantum chemical calculations. We subsequently found excellent spectroscopic agreement that these angles increase from *ca*. 0º to 5–25º several tens of K above T_r, which occurs at 320 K for PBTTT, depending on the inter-ring bond.

4.5 References

1 McCulloch, I. et al. Liquid-crystalline semiconducting polymers with high charge-carrier mobility. Nature Mater. 5, 328-333 (2006).

2 McCulloch, I. et al. Semiconducting thienothiophene copolymers: design, sythesis, morphology, and performance in thin-film organic transistors. Adv. Mater. 21, 1091-1109 (2009).

3 Cao, M. Y. & Wunderlich, B. Phase transitions in mesophase macromolecules. V. Transitions in poly(oxy-1,4-phenylene carbonyl-co-oxy-2,6-naphthaloyl). J. Polym. Sci. B. Polym. Phys. 23, 521-535 (1985).

4 Colthup, N. B., Daly, L. H. & Wiberley, S. E. Introduction to infrared and Raman spectroscopy. (Academic Press, Inc, 1990).

5 Zerbi, G. et al. Molecular mechanics for phase transition and melting of n-alkanes: a spectroscopic study of molecular mobility of solid n-nondecane. J. Chem. Phys. 75, 3175-3194 (1981).

6 Almirante, C., Minoni, G. & Zerbi, G. Mechanism of solid to liquidlike phase transition of alkyl chains in bilayer systems. An infrared spectroscopic study of [CH3(CH2)13NH3]2MnCl4 and [CH3(CH2)13NH3]2ZnCl4. J. Phys. Chem. 90, 852-859 (1986).

7 Tashiro, K. et al. Structure and thermochromic solid-state phase transition of poly(3-alkythiophene). J. Polym. Sci. B. Polym. Phys. 29, 1223-1233 (1991).

8 Zerbi, G., Chierichetti, B. & Inganäs, O. Thermochromism in polyalkylthiophenes: molecular aspects from vibrational spectroscopy. J. Chem. Phys. 94, 4646-4658 (1991).

9 Ho, P. K. H. et al. Solvent effects on chain orientation and interface pi-interaction in conjugated polymer thin fims: Direct measurements of the air and substrate interfaces by near-edge x-ray absorption spectroscopy. Adv. Mater. 19, 215-221 (2007).

10 Carminati, M., Brambilla, L., Zerbi, G., Muellen, K. & Wu, J. Nanoscale architectures for molecular electronics: vibrational spectroscopy and structure of solid hexa-n-dodecyl-hexa-peri-hexabenzocoronene. J. Chem. Phys. 123, 144701-144713 (2005).

11 Kline, R. J. et al. Critical role of side-chain attachment density on the order and device performance of polythiophenes. Macromolecules 40, 7960-7965 (2007).

12 Chabinyc, M. L., Toney, M. F., Kline, R. J., McCulloch, I. & Heeney, M. X-ray scattering study of thin films of poly(2,5-bis(3-alkylthiophen-2-yl)thieno[3,2-b]thiophene). J. Am. Chem. Soc. 129, 3226-3237 (2007).

13 Prosa, T. J., Winokur, M. J. & McCullough, R. D. Evidence of a novel side chain structure in regioregular poly(3-alkylthiophenes). Macromolecules 29, 3654-3656 (1996).

14 Barbarella, G., Zambianchi, M., Bongini, A. & Antolini, L. Crystal structure of 4,4',3",4"'-tetramethyl-2,2':5',2":5",2"'-tetrathiophene: a comparison with the conformation in solution. Adv. Mater. 4, 282-285 (1992).

15 Barbarella, G., Zambianchi, M., Bongini, A. & Antolini, L. The deformability of the thiophene ring: a key to the understanding of the conformational properties of oligo- and polythiophenes. Adv. Mater. 5, 834-838 (1993).

16 Porzio, W., Destri, S., Mascherpa, M. & Brückner, S. Structural aspects of oligothienyl series from X-ray powder diffraction data. Acta Polymer. 44, 266-272 (1993).

17 Papanek, P. et al. Inelastic-neutron-scattering studies of poly(p-phenylene vinylene). Phys. Rev. B 50, 15668-15677 (1994).

18 Haas, S. et al. Large uniaxial negative thermal expansion in pentacene due to steric hindrance. Phys. Rev. B 76,205201-205205 (2007).

Chapter 5. Effects of the T_r ring-twist transition on polaron and the transport density-of-states

In this chapter, we demonstrate the spectrum of the field-induced polarons in both the IR and NIR-Vis regions using charge-modulation spectroscopy (CMS) as a function of temperature. We also measured the temperature and carrier-density dependence of μ_{FET} in a top-gate PBTTT FET, in order to eludicate the reason why the improved polaron interchain delocalisation did not translate to higher μ_{FET}. We find that the character of polarons is in fact sensitive to the T_r ring twist transition. Several distinct polaron species co-exist in well-ordered films of PBTTT, not previously reported and the population of the most weakly self-trapped (i.e., most delocalised) polarons surprisingly increases above T_r. Furthermore, recent theoretical advances allow the parameters of the transport density-of-states (DOS, assumed Gaussian) to be extracted from such data.

5.1 Introduction

A number of recent theoretical studies on single polymer OSC chains have shown that polarons are localised by high-angle ring twists along single bonds connecting the aromatic rings which thus impede their transport.[1,2] Such ring twisting has often been implicated in disordered polymer OSCs, and particularly at high temperatures, although the relevant structure–properties have not yet been quantitatively established. For regioregular poly(3-alkylthiophenes) (rrP3ATs), an important class of polymer OSCs, a rod-to-coil transition has been found at the melting temperature at which interchain coherence is destroyed, presumably as a result of severe ring twisting and the attendant conformational disordering.[3-5] Below the melting temperature however, the π– π * transition spectra of rrP3ATs continually red shift as temperature decreases, which has been interpreted to suggest decreasing ring-twist disorder,[6-8] although details were obscured by various polymorphic and mesophase transitions.[9-11] Therefore, our present understanding of the character of the ring twists is rudimentary even in this most extensively investigated class of polymer OSCs. Yet the existence of cooperative transitions involving ring twists if any has a fundamental impact on exciton and polaron properties of the polymer OSC.

5.2 Experimental methods

5.2.1 Field-effect transistor (FET) characteristics

Top-gate FET is employed for the study of this chapter. For top-gate FET, 50-nm-thick Au (on top of 7-nm-thick Cr layer for adhesion) source-drain arrays were pattermed by photo lithography on fused silica substrates. 50-nm-thick PBTTT film was spin-cast from 10mg/mL chlorobenzene solution on OTS/HMDS treated with lithography substrates, followed by a 200-

nm-thick Teflon AF (Dupont) dielectric polymer film (an amorphous copolymer of 65 mol% 4,5-difluoro-2,2-bis(trifluoromethyl)-1,3-dioxole with 35 mol% tetrafluoroethylene) and 37nm Cr/Ag film as gate electrode as shown in Figure 5.1. The PBTTT films were recrystallized by annealing at 150 °C for 10 min in N_2 glovebox. Variable-temperature FET measurements were obtained in LakeShore TTP4 Probe Station under 10^{-6} mBar and recorded by Keithley 4200-SCS semiconductor parameter analyzer.

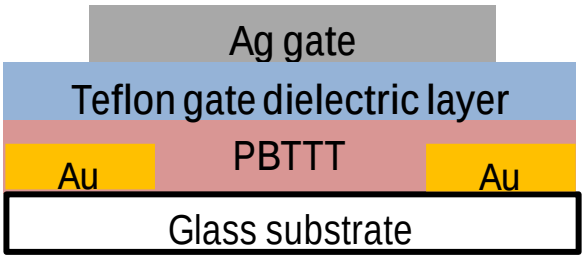

Figure 5.1 Schematic diagram of top-gate FET configuration

5.2.2 Charge modulation spectroscopy (CMS) in near-infrared-visible regime

Top-gate Field-effect transistors on glass substrate were used for NIR–Vis CMS Figure 5.2. The channel length was 20 μm and width was 225 mm with interdigitated area of *ca*. 3x3 mm. The FET devices were mounted in a closed-cycle He cryostat (Janis APD HC-2) with KBr windows for IR and fused silica windows for NIR–Vis measurements and evacuated to 10^{-6} mbar.

NIR–Vis CMS spectra were collected using a home-built optics rig. A sinusoidal drive ac voltage, which was amplified from the reference output signal of a lock-in amplifier (LIA), superposed on the selected dc bias was injected into the diode. Monochromatic light was

incident through the glass substrate at small incident angle, and its reflection collected by mirror optics onto a photodiode with transimpedance gain of 10^7. The voltage output was demodulated by a LIA phase-locked to the ac voltage.

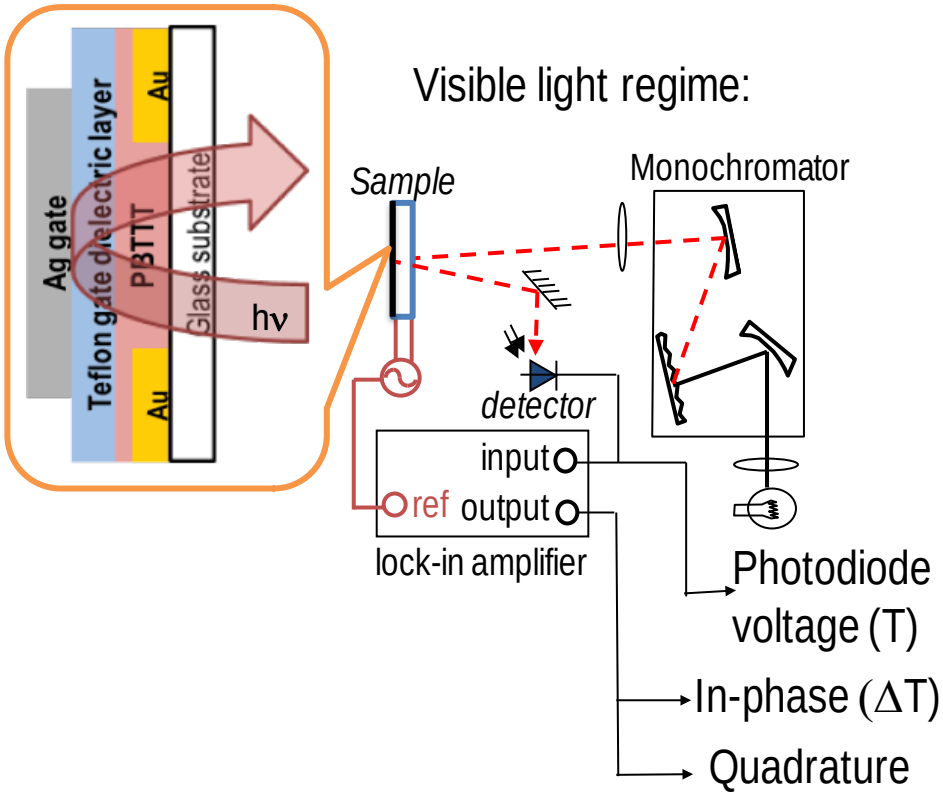

Figure 5.2 Schemetic diagram of the experimental set-up of optical CMS

5.2.3 Charge modulation spectroscopy (CMS) in IR regime using Fourier-transform (FT) technique

For IR CMS, the He cryostat was mounted in a N2-purged spectrometer (Nicolet 8700 FT-IR), the transmitted intensity was then measured by a mercury cadmium telluride detector, as shown in Figure 5.3. Bottom-gate FET devices fbricated on Si substrates were used for IR CMS. The reference output voltage from a lock-in amplifier (SRS 830) was amplified by a homebuilt high-voltage summing amplifier, superimposed on a dc bias, and injected into the electrode array. The dc interferogram (IFG) was first collected by rapid scan (T). The in-phase

and quadrature root-mean-square (rms) ac IFG was collected by step scan of the mirror displacements (retardation) and demodulating detector response at each step using the lock-in amplifier and FT to their respective ac spectra (ΔT). The ΔT/ T spectra were then obtained by normalizing the ac spectrum to the dc spectrum.

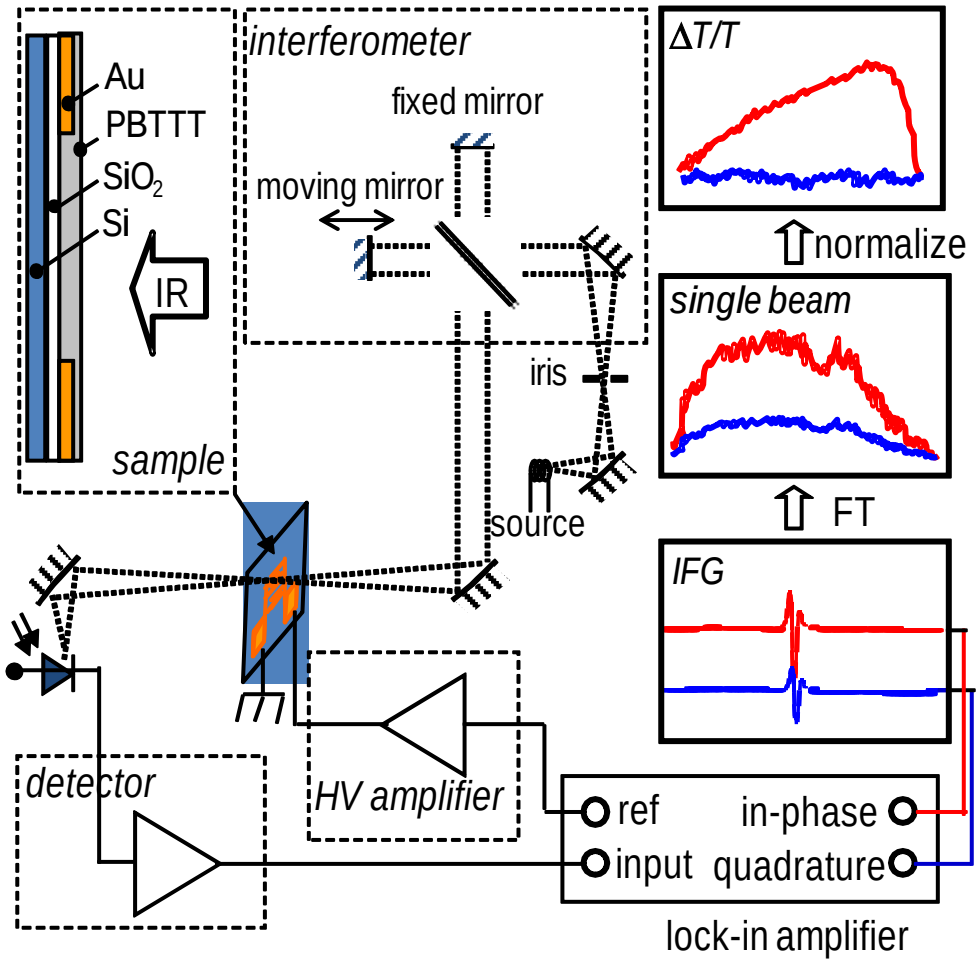

Figure 5.3 Schematic diagram interferogram-modulated FT chargemodulation spectroscopy

5.3 Results and discussions

5.3.1 T_r ring-twist transition enhances interchain polaron delocalisation

CMS was measured in top-gate PBTTT FETs by demodulating the internal reflection spectrum off the Ag top-gate at the fundamental frequency and phase-locked to the modulation of the

gate voltage (V_{ac} superimposed on a V_{dc}) using lock-in techniques. The devices comprise a spin-cast PBTTT film over an interdigitated Au source–drain array that is photolithographically-patterned on glass, and separated from the evaporated Ag top-gate by another spin-cast Teflon AF (Dupont) dielectric film. The modulated density of polarons at the interface gives rise to characteristic spectra comprising several (2 for localised, and 3 for delocalised) bands due to distinct electronic transitions between their levels.[12] In particular the energy of the highest-lying band (denoted C3) receives a contribution from interchain interaction and blue shifts with increasing interchain delocalisation.[12] With increasing delocalisation, the C3 transition approaches the zero-phonon 0–0 transition of the neutral polymer.[12]

Figure 5.4 (a) shows the in-phase CMS spectra of the C3 band for a carrier-density modulation of 0.25 x 10^{12} cm^{-2} at a mean density of 2.2 x 10^{12} cm^{-2} as a function of temperature. Two dominant polaron species with the C3 transition are seen at 1.85 and 2.0 eV respectively. The 2.0-eV population increases in intensity as T increases above T_r at the expense of the 1.88-eV band and its shoulder. This enhancement is not simply due to blue-shifting of the π–π^* gap which amounts to less than 50 meV over this T range.

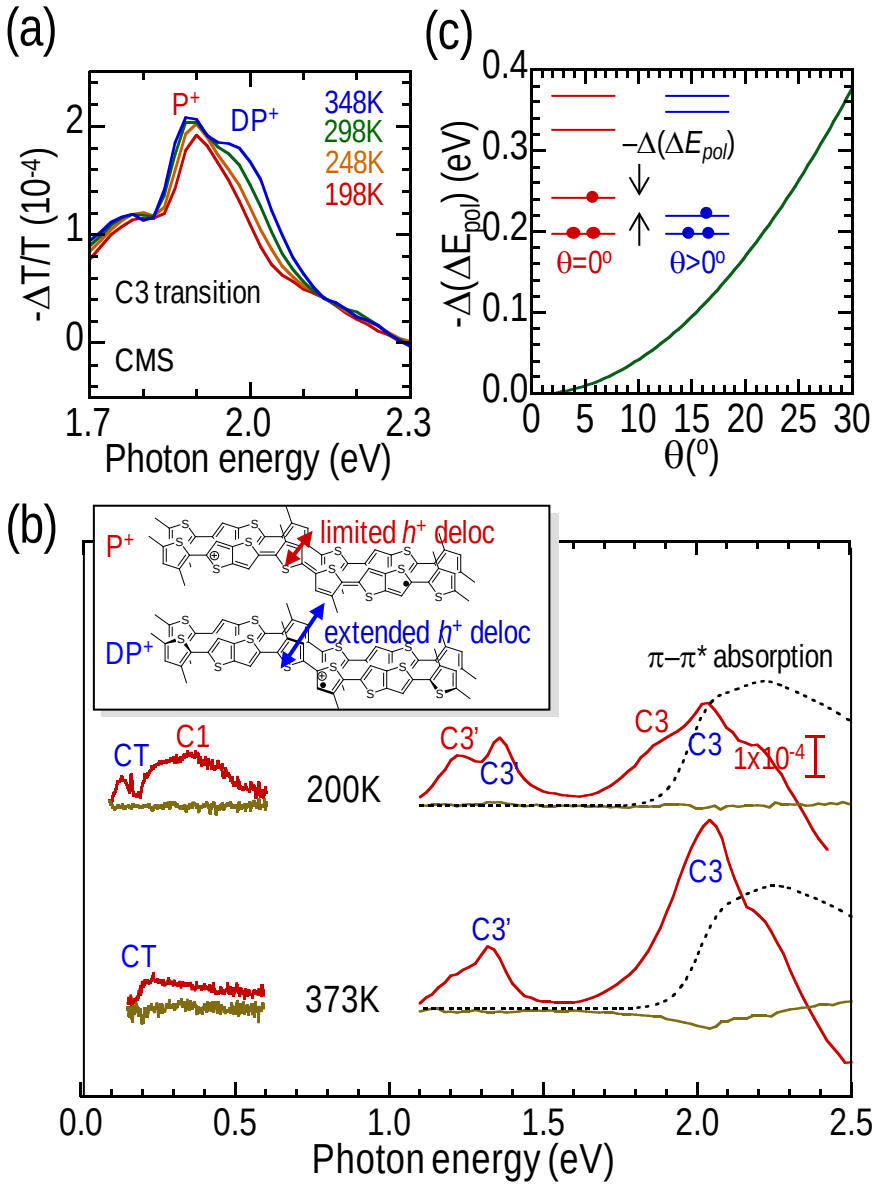

Figure 5.4 Reflection charge-modulation spectroscopy (CMS) of PBTTT FETs. (a) In-phase CMS of the C3 band region at different temperatures. (b) In-phase (red) and quadrature (orange) IR–NIR–optical CMS spectra at 200 K and 373 K. Dotted lines give the absorbance spectra. Gate-bias modulation frequency (1 kHz IR, 170 Hz NIR–optical) was well within FET bandwidth. (c) Computed polaron relaxation loss with ring dihedral angle in an oligothiophenes to illustrate the strong electron–phonon coupling.

Figure 5.4(b) shows the full IR–NIR–optical CMS spectra collected on another PBTTT FET at 200 K (top panel) and 373 K (bottom panel). The IR region was collected by demodulating the interferogram to give both the in-phase and quadrature signal.[13] The three groups of bands again reveals two polaron types with different temperature dependences. We assign the transitions in the high-temperature spectrum at 0.20, 1.35 and 2.05 eV to the charge-transfer CT, and C3' and C3 bands[12] of an interchain-delocalised polaron (DP^+). A spectrum with similar characteristics has also been observed in rrP3ATs, except that both the C3' and C3 bands are red shifted by 0.4 eV.[14,15] Here the near-degeneracy of the C3 band with the π–π^* 0–0 transition and the relative intensity of the C3' to C3 band[12] suggests that this DP^+ in PBTTT is even more delocalised than in rrP3ATs. In the low-temperature spectrum, a new set of transitions appears at 0.35, 1.20 and 1.85 eV which we assign respectively to the C1, C3' and C3 transitions of a less delocalised polaron (P^+). Nevertheless this polaron still has some interchain character, unlike those in the regiorandom P3ATs.[16] Clearly DP^+ has a smaller polaron relaxation energy (i.e., weaker electron–phonon coupling) than P^+, and this is further evidenced by its Drude-like tail.

A remarkable feature of these results is that the relative population of DP^+ over P^+ increases with temperature above T_r. To gain an insight into this result, we computed the loss of polaron relaxation energy $-\Delta(\Delta E_{pol})$ with the dihedral angle θ (between adjacent bithiophene units) in a long oligomer. The result can be described by a simple function, $-\Delta(\Delta E_{pol}) = K\,(1-\cos\theta)$ with K = 2.8 eV, according to our PM3 calculations of the energy difference between the polaron state and the ground state as a function of θ (Figure 5.4 (c)). This is equivalent to the torsional

part of the lattice Hamiltonian for the inter-ring bond neglecting the small coupling between the torsion and bond-alternation terms.[1,2]

We found that $-\Delta(\Delta E_{pol})$ can approach 0.1 eV which is significant for $\theta \approx 15°$. Twisting of rings destabilises the polaron more than the neutral chain, because the polaron has higher π-electron density in the inter-ring bond.[17] As a result, the polaron energy levels shift towards the HOMO and LUMO edge. This should also increase the interchain hopping integral and improve delocalisation. This effect however is masked in materials with poor interchain order.

5.3.2 Temperature and charge carrier density dependence of μ_{FET}

Figure 5.5 shows the temperature dependence of the hole μ_{FET} at different hole densities (p) in a top-gate PBTTT FET with Teflon AF (Dupont) dielectric, while Figure 5.6 shows the same data plotted directly against p. The μ_{FET} was evaluated in the linear regime[18] using $\mu_{FET}(p) = \frac{L}{C_{ox} w V_d} \cdot \left.\frac{di_{FET}}{dV_g}\right|_p$. Data for a bottom-gate FET with octadecyltrichlorosilane and hexamethyldisilazane-treated thermal SiO_2 as dielectric are similar. The $\log(\mu_{FET})$ data shows a $1/T$-dependence for $140 < T < 320$ K. Linear extrapolation to $T \rightarrow \infty$ gives *ca*. 10 $cm^2\ V^{-1}\ s^{-1}$, which is broadly in line with other polymers.[19]

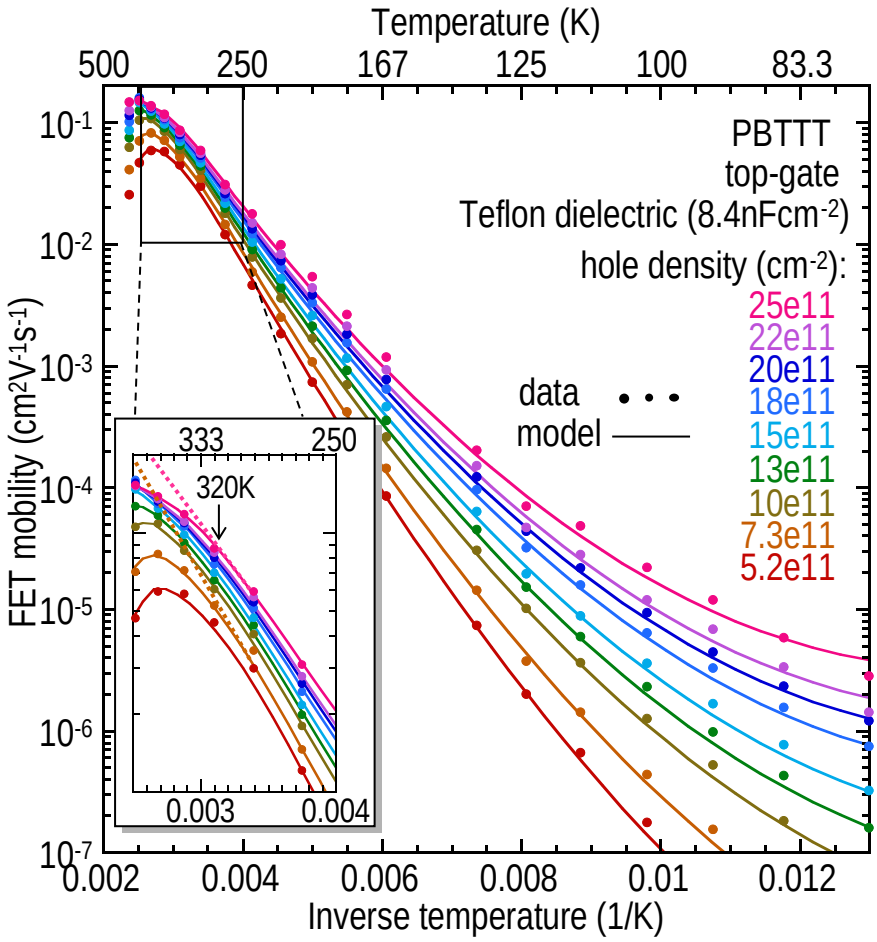

Figure 5.5 Analysis of the temperature- and carrier-density-dependence of the linear-regime hole field-effect mobility using the Coehoorn general hopping model: field-effect mobility against inverse temperature at different hole densities. Symbols are data; lines give model predictions. Inset: Zoom-in of the high temperature data revealing a transition at 320 K.

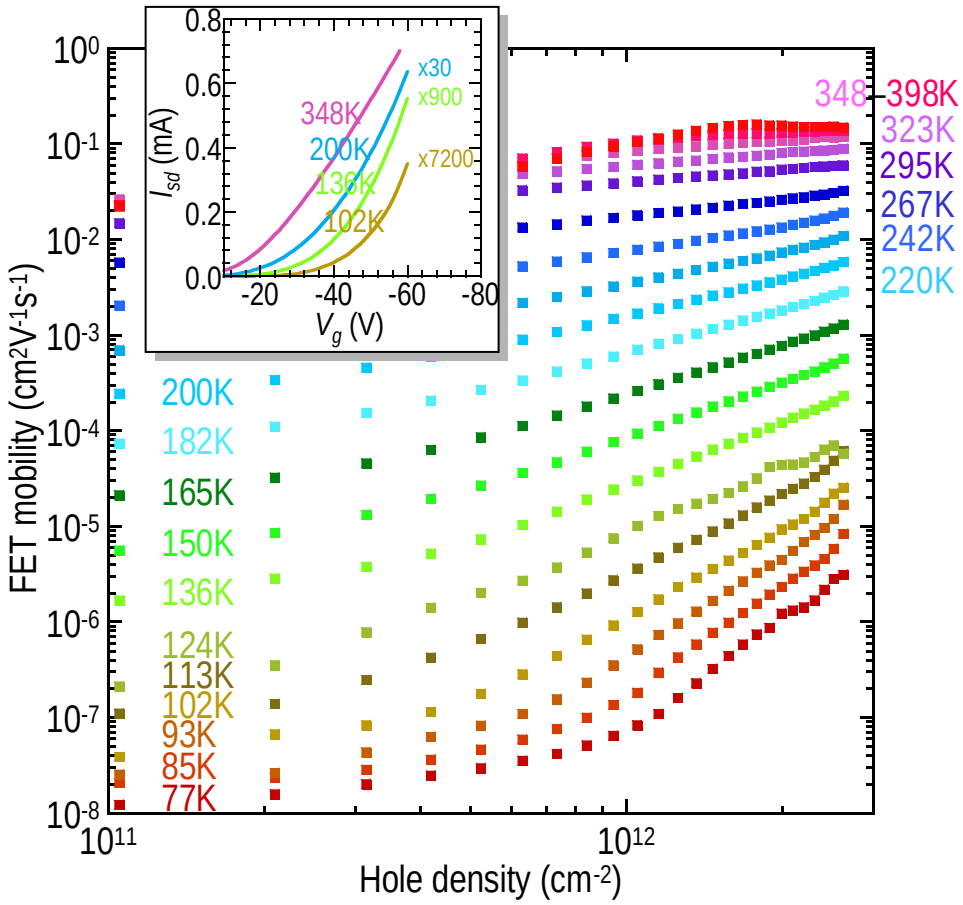

Figure 5.6 Analysis of the temperature- and carrier-density-dependence of the linear-regime hole field-effect mobility using the Coehoorn general hopping model. Plots of the same data explicitly against hole densities. Inset: Plots of source–drain currents against gate bias for different temperatures showing a transition from dispersive (i.e., trapping) to non-dispersive behaviour at high temperatures.

The low-temperature curvature of these log(μ_{FET}) *vs* 1/*T* plots and their marked *p*-dependence are the two characteristic signatures of polaron hopping in a disordered DOS.[20,21] The dispersion of μ_{FET} with carrier density (i.e., non-zero $\frac{d\mu_{FET}}{dp}$) indicates that the Fermi level (E_F) increases with *p*, and polarons populating higher up the DOS require smaller energetic hops to the percolating transport level that occurs near the DOS centre.[22] Therefore despite the excellent lamellar order in PBTTT, its hole μ_{FET} is still dominated by hopping in a disordered DOS and not the intrinsic polaron transport. This is in accord with a distribution of

local chain environments which show up as distinct absorption states,[23] and also with the lack of correlation between μ_{FET} and the interface-induced localisation of the polarons.[24]

5.3.3 Effect of ring-twist transition of density-of-state (DOS)

To quantitatively model this effect, we determined that all the $\mu_{FET}(T, p)$ data below 320 K can be fitted using a single σ_{DOS} of 71 meV in the generalized Coehoorn hopping transport model:[21]

$$\mu_{FET} = \frac{e\nu_0}{nk_BT}\Phi \exp(-p_0 - \ln(c) - (a\frac{\sigma_{DOS}}{k_BT} - \frac{E_f}{k_BT}) + \frac{d}{p_0}(\frac{\sigma_{DOS}}{k_BT})^2),$$

where *a* and *d* are parameters we have taken from the Vissenberg–Matters model,[20] Φ is of order unity (assumed 1.0), *n* is 2D hopping site density (= 1.3 x 10^{14} cm^{-2}), and p_0 = $(\frac{4B}{\pi}\frac{\alpha^2}{n})^{1/2}$ (≈ 5.9, we computed for 2D hopping), and the ν_0 obtained (4.5 x 10^{14} Hz) was reasonable. The fits are shown as solid lines to the data in symbols in Figure 5a. From these fits we derived the self-consistent E_F–*p* relationship as shown in Figure 5.7.

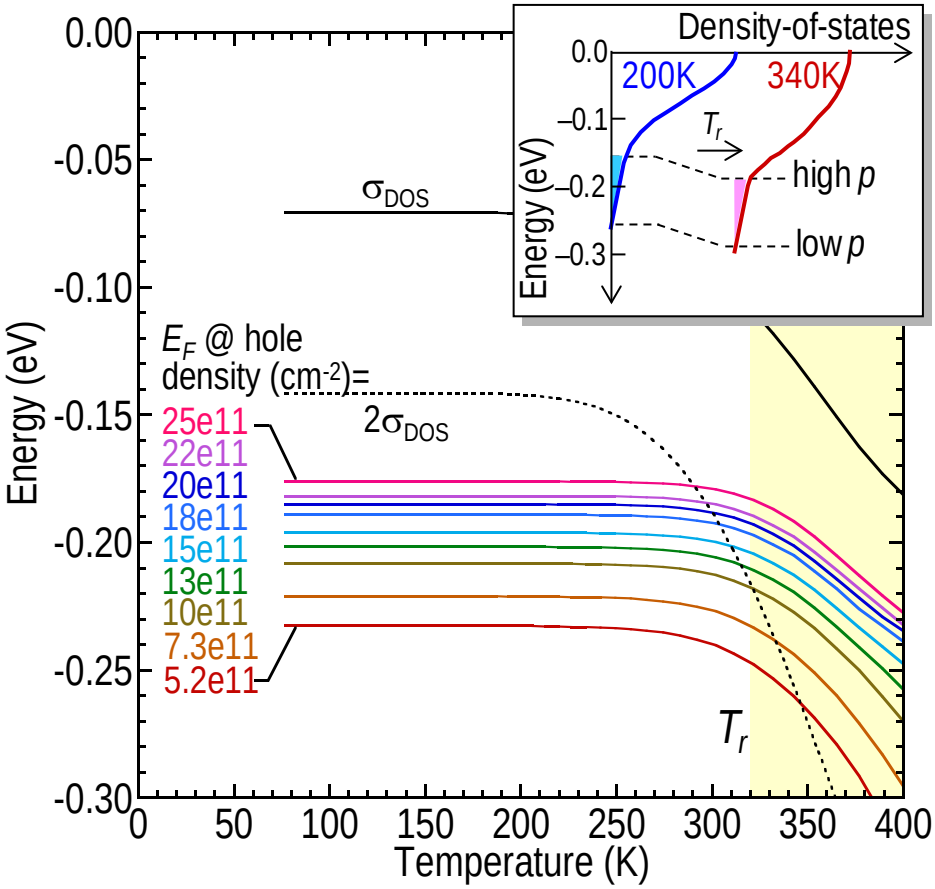

Figure 5.7 Fermi energy against temperature for different hole densities, extracted from model. Inset: schematic illustration of how the density-of-states varies from low to high temperatures showing a soft pinning of the DOS tail despite thermal broadening of the centre states.

This excellent simultaneous fits over a wide T and p range suggests that the Coehoom model provides an excellent description of transport in this FET. From the extracted p dependence of E_F, we can reconstruct the occupied DOS tail by differentiation (dp/dE) as shown in the inset of Figure 5.7. The DOS tail is thus found to be approximately linear rather than Gaussian. Crucially, the DOS width increases continually above the T_r of 320 K. This is remarkable as it confirms that the ring-twist transition measured in the bulk of the neutral PBTTT chains does affect polaron transport by broadening the hopping energy landscape, in addition to the change of character suggested by CMS. Furthermore, the constancy of the DOS width below 320 K

shows clearly that the onset of alkyl side-chain disordering at 220 K does not degrade the transport DOS.

Above T_r, in order to fit the μ_{FET} (T, p) data, we allowed σ_{DOS} to increase with T and the relative position of E_F to creep up the DOS. Good fits were obtained until T_k when severe disordering occurs. Therefore as T increases above T_r, the σ_{DOS} broadens, which is not surprising, but the E_F does not shift rigidly with this broadening. Hence the mild ring twists do not cause tail states to broaden symmetrically and extend into the gap. As a result of this "soft pinning", the E_F creeps up within $2\sigma_{DOS}$, which mitigates the effect of disordering. As a consequence, μ_{FET} become non-dispersive with p (i.e., $\frac{d(\mu_{FET})}{dp} \approx 0$), and the FET characteristics (both output and transfer) become remarkably well-behaved above T_r (see inset of Figure 5.7).

5.4 Summary

The existence of a cooperative ring twist T_r transition in a highly-ordered π-conjugated polymer with high μ_{FET} measured in the bulk of the neutral PBTTT chains does affect polaron transport through the density-of-states and the character of the polaron, which occurs at the interface. The side-chain melting at 220 K has practically no impact on the charge transport. Thermally-induced ring-twist disorder is however detrimental to polaron transport due to the inevitable DOS broadening. Nevertheless, this suggests a new direction for molecular design to ultimately reach the elusive 2-D delocalised transport regime in organic materials.

5.5 References

1 Yu, Z. G., Smith, D. L., Saxena, A., Martin, R. L. & Bishop, A. R. Molecular geometry fluctuations and field-dependent mobility in conjugated polymers. *Phys. Rev. B* 63, 085202-085201-085209 (2001).

2 Hultell, M. & Stafström, S. Impact of ring torsion dynamics on intrachain charge transport in conjugated polymers. *Phys. Rev. B* 79, 014302-014301-014307 (2009).

3 Yoshino, K., Nakajima, S., Park, D. H. & Sugimoto, R. Thermochromism, photochromism and anamolous temperature dependence of luminescence in poly(3-alkylthiophene) film. *Jap. J. Appl. Phys.* 27, L716-718 (1988).

4 Inganäs, O., Gustafsson, G., Salaneck, W. R., Österholm, J. E. & Laakso, J. Thermochroism in thin films of poly(3-alkylthiophenes). *Synth. Met.* 28, C377-384 (1989).

5 Tashiro, K. *et al.* Structure and thermochromic solid-state phase transition of poly(3-alkythiophene). *J. Polym. Sci. B. Polym. Phys.* 29, 1223-1233 (1991).

6 Zerbi, G., Chierichetti, B. & Inganäs, O. Thermochromism in polyalkylthiophenes: molecular aspects from vibrational spectroscopy. *J. Chem. Phys.* 94, 4646-4658 (1991).

7 Roux, C. & Leclerc, M. Thermochromic properties of polythiophene derivatives: formation of localised and delocalised conformational defects. *Chem. Mater.* 6, 620-624 (1994).

8 Yang, C., Orfino, F. P. & Holdcroft, S. A phenomenological model for predicting thermochromism of regioregular and nonregioregular poly(3-alkylthiophenes). *Macromolecules* 29, 6510-6517 (1996).

9 Prosa, T. J., Winokur, M. J. & McCullough, R. D. Evidence of a novel side chain structure in regioregular poly(3-alkylthiophenes). *Macromolecules* 29, 3654-3656 (1996).

10 Bolognesi, A. *et al.* Structural and thermal behaviour of poly(3-octylthiophene): a DSC, ^{13}C MAS NMR, XRD, photoluminescence and Raman scattering study. *Macromol. Chem. Phys.* 202, 2586-2591 (2001).

11 Yazawa, K., Inoue, Y., Yamamoto, T. & Asakawa, N. Twist glass transition in regioregulated poly(3-alkylthiophene). *Phys. Rev. B* 74, 094204-094201-094212 (2006).

12 Beljonne, D. *et al.* Optical signature of delocalised polarons in conjugated polymers. *Adv. Funct. Mater.* 11, 229-234 (2001).

13 Zhuo, J. M. *et al.* Direct evidence for delocalisation of charge carriers at the Fermi level in a doped conducting polymer. *Phys. Rev. Lett.* 100, 186601-186601-186604 (2008).

14 Sirringhaus, H. *et al.* Two-dimensional charge transport in self-organized, high-mobility conjugated polymers. *Nature* 401, 685-688 (1999).

15 Österbacka, R., An, C. P., Jiang, X. M. & Vardeny, Z. V. Two-dimensional electronic excitations in self-assembled conjugated polymer nanocrystals. *Science* 287, 839-842 (2000).

16 Brown, P. J., Sirringhaus, H., Harrison, M., Shkunov, M. & Friend, R. H. Optical spectroscopy of field-induced charge in self-organized high mobility poly(3-hexylthiophene). *Phys. Rev. B* 63, 125204:125201-125211 (2001).

17 Zade, S. S. & Bendikov, M. Theoretical study of long oligothiophene polycations as a model for doped polythiophene. *J. Phys. Chem. C* 111, 10662-10672 (2007).

18 Tanase, C., Meijer, E. J., Blom, P. W. M. & De Leeuw, D. M. Unification of the hole transport in polymeric field-effect transistors and light-emitting diodes. *Phys. Rev. Lett.* 91, 216601-216601-216604 (2003).

19 Craciun, N. I., Wildeman, J. & Blom, P. W. M. Universal Arrhenius temperature activated charge transport in diodes from disordered organic semiconductors. *Phys. Rev. Lett.* 100, 056601-056601-056604 (2008).

20 Vissenberg, M. C. J. M. & Matters, M. Theory of the field-effect mobility in amorphous organic transistors. *Phys. Rev. B* 57, 12964-12967 (1998).

21 Coehoorn, R., Pasveer, W. F., Bobbert, P. A. & Michels, M. A. J. Charge-carrier concentration dependence of the hopping mobility in organic materials with Gaussian disorder. *Phys. Rev. B* 72, 155206-155201-155220 (2005).

22 Baranovskii, S. D., Faber, T., Hensel, F. & Thomas, P. The applicability of the transport-energy concept to various disordered materials. *J. Phys.: Condens. Matter* 9, 2699-2706 (1997).

23 Wang, S. *et al.* Solvent effects and multiple aggregate states in high-mobility organic field-effect transistors based on poly(bithiophene-alt-thienothiophene). *Appl. Phys. Lett.* 93, 162103-162101-162103 (2008).

24 Zhao, N. *et al.* Polaron localisation at interfaces in high-mobility microcrystalline conjugated polymers. *Adv. Mater.* 21, 3759-3763 (2009).

Chapter 6. Outlook

Alkyl-substituted PBTTT films show a macroscopic monolayer-terraced morphology that is fundamentally different from the folded-chain and fringed-micelle crystalline morphologies often found in other π-conjugated polymers such as rrP3HT. This unusual well-ordered lamellar morphology was previously known as the origin of the high field-effect mobility for this material. However, we demonstrated that the formation of lamellar morphology is general and also achieved in rrP3HT. Therefore, this provides opportunities to a new processing "design" rule to make highly-ordered π-conjugated polymer films to further improve device performance. We also found that disorder in π-conjugated backbone, which was thought to localise polaron charge carriers, in fact enhance the interchain delocalised polaron. Therefore, this suggests that controlled small angle ring-twist within π-conjugated backbone is possible to achieve ultimately real 2-D delocalised charge transport in organic materials. In the CMS measurements of PBTTT, more than one species of polarons were observed and the polaron behaviour is also sensitive to the preparation of the device. This observation is different from well-known rrP3HT CMS spectrum. Therefore, systematic measurements to reveal the dependence of the polaron on temperature and charge carrier density are of direct relevance to the nature of charge transport in this material. The deeper understanding of the charge transport properties will provide more insights on the molecular and device designs.

Appendix

A. Publications arising from this work

1. L.-H. Zhao, R. Q. Png, J.-M. Zhuo, J.-C. Tang, L. Y. Wong, R. H. Friend, L.-L. Chua, P.K.-H. Ho, "The ring-twist transition in semicrystalline π-conjugated organic semiconductors: Inducing polaron delocalization through suppression of intrachain relaxation " , manuscript submitted to Nature Materials.
2. L.-H. Zhao, R. Q. Png, J.-M. Zhuo, L. Y. Wong, J.-C. Tang, Y.-S. Su, L.-L. Chua, "A General Method to Induce Macroscopically Well-Oriented Lamellar Order π-Stackable Polymer Films Using Borderline−Poor Solvents", manuscript submitted to JACS.
3. L.-H. Zhao, R. Q. Png, J.-C. Tang, J.-M. Zhuo, L.-L. Chua, "Moelcular-weight dependence of the liquid-crystalline transitions of poly(bithiophene–*alt*–thienothiophene): evidence for the role of π-stacking interactions and a new nematic phase", manuscript submitted to Macromolecules.

B. Publications (up till 2010) from work not described in this thesis

1. Y. Vaynzof, D. Kabra, L.-H. Zhao, L.-L. Chua, U. Steiner, R. H. Friend, "Surface-Directed Spinodal Decomposition in Poly[3-hexylthiophene] and C-61-Butyric Acid Methyl Ester Blends", ACS Nano, 5 (2010) 329
2. Y. Vaynzof, D. Kabra, L.-H. Zhao, L.-L. Chua, P.K.-H. Ho, R. H. Friend, "Improved photoinduced charge carriers separation in organic-inorganic hybrid photovoltaic devices", 97 (2010) 033309
3. J.-M. Zhuo, L.-H. Zhao, R. Q. Png, L.-Y. Wong, P. J. Chia, J.-C. Tang, S. Sivaramakrishnan, M. Zhou, E.C.-W. Ou, S.-J. Chua, W. S. Sim, L.-L. Chua, P. K.-H. Ho, "Direct spectroscopic evidence for a photodoping mechanism in polythiophene and poly(bithiophene-alt-thienothiophene) organic semiconductor thin films involving oxygen and sorbed moisture", Advanced Materials., 21 (2009) 4747
4. J.-M. Zhuo, L.-H. Zhao, P.-J. Chia, W. S. Sim, R. H. Friend, P. K.-H. Ho, "Direct evidence for delocalization of charge carriers at the fermi level in a doped conducting polymer", Physical Review Letters, 100 (2008) 186601
5. S. Wang, J.-C. Tang, L.-H. Zhao, R.Q. Png, L. Y. Wong, P.J. Chia, H. S.-O. Chan, P. K.-H. Ho, L.-L. Chua, Solvent effects and multiple aggregate states in high-mobility organic field-effect transistors based on poly(bithiophene-alt-thienothiophene), Applied Physical Letters, 93 (2008) 162130
6. S. Wang, P. J. Chia, L.-L. Chua, L.-H. Zhao, R. Q. Png, S. Sivaramakrishnan, M. Zhou, R. G.-S. Goh, R. H. Friend, A. T.-S. Wee, P. K.-H. Ho, "Band-like transport in surface-functionalized highly solution-processable graphene nanosheets", Advanced Materials, 20 (2008) 3440

7. L.-L. Chua, S. Wang, P.J. Chia, L. Chen, L.-H. Zhao, W. Chen, A. T.-S. Wee, P. K.-H. Ho, “Deoxidation of graphene oxide nanosheets to extended graphenites by "unzipping" elimination”, Journal of Chemical Physics, 129 (2008) 114702
8. P. J. Chia, L.-L. Chua, S. Sivaramakrishnan, J.-M. Zhuo, L.-H. Zhao, W. S. Sim, Y.-C Yeo, P. K.-H. Ho, “Injection-induced de-doping in a conducting polymer during device operation: aymmetry in the hole injection and extraction rates”, Advanced Materials, 19 (2007) 4202

C. Conference presentations (presenting author underlined)

L.-H. Zhao, J.-M. Zhuo, L.Y. Wong, S. Wang, W.-S. Sim, P.K.-H. Ho, "Charge modulation spectroscopy of charge carriers in organic thin-film transistors" International Conference on Materials for Advanced Technology (ICMAT), July 1-6, 2007, Singapore. (Posterl presentation)

L.-H. Zhao, J.-M. Zhuo, P. J. Chia, W.-S. Sim, R. H. Friend, P.K.-H. Ho, “Direct evidence for delocalised charge carriers at the Fermi level in a doped conducting polymer” European Materials Research Society (E-MRS) Spring Conference, May 26-30, 2008, Strasbourg, France. (Posterl presentation)

L.-H. Zhao, J.-C. Tang, R. Q. Png, L. Y. Wong, J.-M. Zhuo, P. J. Chia, L.-L.. Chua, P.K.-H. Ho, "A new order-to-disorder transition observed in a high-mobility semiconducting polymer poly(bithiophene-alt-thienothiophene) (PBTTT)" International Conference on Materials for Advanced Technology (ICMAT), June 28-July 3, 2009, Singapore. (Poster presentation)

L.-H. Zhao, R. Q. Png, J.-C. Tang, L. Y. Wong, J.-M. Zhuo, R. H. Friend, L.-L. Chua, P.K.-H. Ho, “Direct evidence for a ring-twist transition in π-conjugated semicrystalline organic semiconductors” Materials Research Society (MRS) Spring Conference, April 5-9, 2010, San Francisco, USA (Poster Presentation)